STUDY OF THE PROPERTIES OF NETWORKS OF LOW-DIMENSIONAL NANOMATERIALS FOR TRANSPARENT FLEXIBLE DEVICE APPLICATIONS

SOPHIE SOREL

A thesis submitted for the degree of
Doctor of Philosophy

Supervised by Prof. Jonathan Coleman
Chemical Physics of Low Dimensional Nanostructures Group
School of Physics
Trinity College Dublin

2013

To my family, Mum, Diane, Marguie and Nick.

DECLARATION

I declare that this thesis has not been submitted as an exercise for a degree at this or any other university and it is entirely my own work.

I agree to deposit this thesis in the University's open access institutional repository or allow the library to do so on my behalf, subject to Irish Copyright Legislation and Trinity College Library conditions of use and acknowledgement.

Elements of this work that have been carried out jointly with others or by collaborators have been duly acknowledged in the text wherever included.

Sophie Sorel

Better late than never is poor consolation for the man who has lost the opportunity of a lifetime

(Henri Becquerel)

The most incomprehensible thing about the world is that it is comprehensible.

(Albert Einstein)

ACKNOWLEDGMENTS

First and foremost I would like to thank Prof. Coleman for his patience and guidance throughout my PhD; I could not have hoped for a better supervisor. I must thank HP and SFI for the funding through which I completed my work. I would also like to thank Phil Lyons for helping me through my first year and Lia and Rita from administration. Finally I must thank all my friends from the group. Mustafa Lotya for always being there to bounce ideas off over a nice cup of tea. Peter, always there, always smiling. Everyone in the group for making it a fantastic, fun, messy 4 years. Thank you also to people from other groups for helping me branch out, the Boland group, the Cross group, the Blau group... Last but not least, I must thank my family whom I love more than anything. Mum, words can't describe how proud I am that you are proud of me, you're my angel. Diane, you are the only one who understands what I'm talking about, you would have made a great physicist. Marguie, routinely breaking my concentration with random phonecalls which often lead to my brightest ideas. Nick, you kept me sane and you made me tea and I love you.

PUBLICATIONS

1. *The relationship between material properties and transparent heater performance for both bulk-like and percolative nanostructured networks* - Sophie Sorel, Daniel Bellet and Jonathan N Coleman, under revision (2014)

2. *The dependence of the optoelectrical properties of silver nanowire networks on nanowire length and diameter* - Sophie Sorel, Philip E Lyons, Sukanta De, Janet C Dickerson and Jonathan N Coleman, Nanotechnology, (23) 185201 (2012)

3. *Flexible, transparent dielectric capacitors with nanostructured electrodes* - Sophie Sorel, Umar Khan, and Jonathan N. Coleman, Appl. Phys. Lett. 101, 103106 (2012)

4. *Manipulating Connectivity and Electrical Conductivity in Metallic Nanowire Networks* - Peter N. Nirmalraj, Allen T. Bellew, Alan P. Bell, Jessamyn A. Fairfield, Eoin K. McCarthy, Curtis O'Kelly, Luiz F. C. Pereira, Sophie Sorel, Diana Morosan, Jonathan N. Coleman, Mauro S. Ferreira, and John J. Boland, Nano Letters, 12 (11), 5966-5971 (2012)

5. *Transparent, Flexible, and Highly Conductive Thin Films Based on Polymer–Nanotube Composites* - Sukanta De, Philip E. Lyons, Sophie Sorel, Evelyn M. Doherty, Paul J. King, Werner J. Blau, Peter N. Nirmalraj, John J. Boland, Vittorio Scardaci, Jerome Joimel, and Jonathan N. Coleman, ACS Nano, 3 (3), 714-720 (2009)

6. *Transparent conducting films from $NbSe_3$ nanowires* - Sukanta De, Conor S Boland, Paul J King, Sophie Sorel, Mustafa Lotya, U Patel, Z L Xiao and Jonathan N Coleman, Nanotechnology, (22) 285202 (2011)

ABSTRACT

Transparent conductors (TC) - materials that are both transparent and conductive - are of great interest for modern technologies. However, a replacement is needed for the most commonly used TC, Indium tin oxide (ITO), because it requires high temperature processing and lacks flexibility, which is a critical requirement for future applications. Networks of silver nanowires are an excellent candidate for transparent flexible applications. In this work, I made a range of networks - with different thicknesses - of silver nanowires - with different lengths and diameters - in order to understand the effects of the aspect ratio of silver nanowires on the networks' opto-electrical properties. The best networks had a transmittance $T = 90\%$ for $R_S = 45\Omega/\square$ and annealing the networks for $30\ min$ at 200^oC improved the ratio of dc to optical conductivity, a figure of merit (FoM) which describes the opto-electrical properties of networks of 1D materials, by a factor of two. However in order to be able to compare network and nanowire properties in the percolation region, new FoM's had to be introduced: the percolation exponent n and the percolative FoM Π. n and Π spanned 0.67 to 2.44 and 20 to 56 respectively. I showed that a lower n and higher Π would lead to the best properties and I estimated that nanowires with a diameter of $25nm$ would yield a transmittance $T = 90\%$ and a sheet resistance $R_S = 25\Omega/\square$. Nanowires were cut using sonic energy and I found that the length of the nanowire depends on sonication time as $L \propto t^{-0.3}$. Being able to cut the nanowires allowed me to show that in the bulk regime the conductivity ratio depends on nanowire length and diameter as $\frac{\sigma_{DC,B}}{\sigma_{Op}} \propto \frac{L}{D}$.

Following the group's success with depositing one dimensional nanomaterials into state of the art transparent thin films, I decided to make transparent flexible dielectric capacitors with nanostructured porous electrodes. I successfully designed and constructed these devices by depositing carbon nanotubes either side of a thin film of polyvinyl acetate. By varying the geometry of the dielectric and electrode layers, their influence on the capacitors' properties could be defined. Impedance spectroscopy

was used to characterise capacitors with transmittance between 60% and 75%, electrode sheet resistance between $400\Omega/\square$ and $9k\Omega/\square$, and capacitance between $0.35F.\mu m^{-1}$ and $0.9F.\mu m^{-1}$. I showed that increasing the thickness of the dielectric would lower the areal capacitance following the definition $\frac{C}{A} = \frac{\varepsilon_0 \varepsilon_r}{d}$, however the electrode thickness had no effect on the capacitance. Identically, varying the electrode thickness varied the transmittance and sheet resistance while the polymer thickness had no effect on these properties. To prove their use for flexible applications, the capacitors were tested for mechanical stability. The capacitance and resistance were measured after cycles of bending the sample back and forth to a radius of curvature of $8\ mm$ and both proved stable under these conditions. I then varied the electrode material as a substitute for carbon nanotubes and fabricated a range of capacitors using graphene and silver nanowires electrodes. The graphene electrodes showed very poor sheet resistance but displayed identical geometric and active capacitive areas which is an advantage for reproducibility. On the other hand, silver nanowire networks displayed very good opto-electrical properties but the capacitance measurements displayed very large scatter due to the wires' surface roughness (which made their active area actually much larger than the geometric area of the device) and the network inhomogeneity from spraying.

Finally, I studied silver nanowires as Joule heaters for transparent flexible heater applications. These devices have been made by other groups before, using various one and two dimensional materials, however the heat transfer and heat loss mechanisms have yet to be fully understood. A range of flexible heaters were made from silver nanowire networks and the temperature rise investigated as a function of time, current applied and electrode transmittance. The maximum temperature obtained was 47.7^oC for a network with $T_r = 90\%$ under an applied current $I = 100mA$. Expressions for the temperature as a function of time and current were derived and tested against the data and a new dissipation constant, β, was defined. The derived equation for the transient curves fit the data rather well, although the setup's design could be improved in order to reduce the scatter in the obtained values for β. The behaviour of both bulk and percolative networks could also be very well explained by a derived expression linking surface temperature to network transmittance. A 3D surface plot was generated to

describe the temperature change as a function of transmittance and applied current and it was shown that temperatures as high as $100^{o}C$ could be achieved for a network with transmittance $T_r = 94\%$ under an applied current $I = 20mA$.

LIST OF ABBREVIATIONS:

1D:	*One dimensional*
AAO:	*Anodised aluminium oxide*
AgNW:	*Silver nanowire*
CNT:	*Carbon nanotubes*
CVD:	*Chemical vapor deposition*
D:	*Diameter of nanowires*
DMF:	*Dimethylformamide*
FoM:	*Figure of merit*
FPD:	*Flat panel displays*
HSP:	*Hansen solubility parameters*
IPA:	*Isopropanol*
ITO:	*Indium tin oxide*
L:	*Length of nanowires*
LCD:	*Liquid crystal display*
MTP:	*Multiply twinned particles*
OLED:	*Organic light-emitting diodes*
PDMS:	*Polydimethylsiloxane*
PET:	*Polyethylene terephthalate*
PVA:	*Polyvinyl alcohol*
PVAc:	*Polyvinyl acetate*

PVP: *Polyvinylpyrrolidone*

R_s: *Sheet resistance*

SDS: *Sodium dodecyl sulphate*

SEM: *Scanning electron microscope*

SWNT,MWNT: *Single-walled or multi-walled carbon nanotubes*

T: *Transmittance (Tr in chapter 7)*

T: *Temperature (in chapter 7)*

TC: *Transparent conductors*

TCO: *Transparent conducting oxides*

TFC: *Transparent, flexible dielectric capacitors*

TFH: *Transparent flexible heaters*

THF: *Tetrahydrofuran*

t_{min}: *Percolation transition thickness*

CONTENTS

LIST OF FIGURES

LIST OF TABLES

1

INTRODUCTION AND THESIS OUTLINE

IPads, Kindles, solar cells, LCDs... Exciting technologies which have yet to become transparent and flexible. Transparent conductors (TC), materials that are transparent to light yet electrically conductive: these are the materials of choice to undertake such a challenge but they have yet to make it happen.

For years, the field of transparent conductors has been flooded with work on transparent conducting oxides (TCO), led by studies on the most widely used TCO: Indium Tin Oxide (ITO). ITO is an n-type semiconductor with properties such as $T = 90\%$ for $R_S = 10\ \Omega/\square$ so it is not surprising that it is such a popular option for TC applications. However there are drawbacks to ITO. Indium has become sparse which has led to a steady rise in its cost over the last 20 years (*100 $/kg* to *900 $/kg* between *1990* and *2007*). Since *75%* of its mass is Indium, ITO is becoming economically unviable. ITO also requires high temperatures for its processing, which again increases production costs while at the same time reducing the number of substrates that can be used for its deposition. The most inconvenient aspect of ITO is its brittleness due to its ceramic nature (Figure 1.1). Indeed, the next generation of optoelectronic devices requires transparent conductive electrodes to be lightweight, flexible, cheap

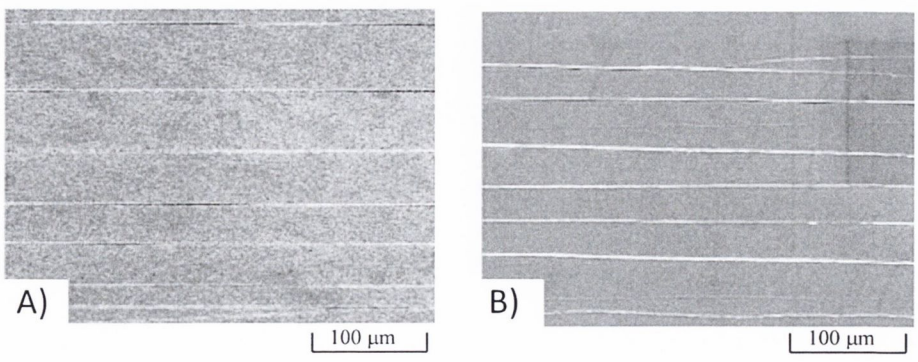

Figure 1.1: Failure of ITO thin films under mechanical strain: A) tension B) compression.[1]

and compatible with large-scale manufacturing methods, conditions which ITO cannot fulfill. Therefore industry is searching for a new material which would have the same great opto-electrical properties as ITO but which would also be stable under mechanical strain and would ideally be processed on a large scale at near room temperature.

Luckily the scientific community has already been studying a range of new materials as a replacement for ITO: conducting polymers such as PEDOT:PSS, graphene, carbon nanotube and metallic grids and nanowires. Although those are all promising materials with exciting properties, only silver nanowires have the ability to achieve low enough sheet resistances for a transmittance above 90% and have the added benefit of having a very flat transmittance spectrum over the visible range. Of course, the other major advantage of nanowire or nanotube networks is that individual wires/tubes can slide along each other when the network is under strain without altering junction resistance, hence keeping overall network resistance stable [2]. Although a lot of work has been put into achieving state of the art nanowire networks, the dependence of the transmittance and sheet resistance on the geometry of the nanowires themselves has not been studied. However, the demands on novel TC materials are such that it is indispensable to understand the networks' connectivity in order to produce the highest quality electrodes which could be tuned to specific electrical and optical requirements for transparent flexible applications.

The natural continuation for reaching towards state of the art networks of nanomaterials is to create straightforward applications exploiting the unique properties of porous electrodes of one dimensional (1D) materials. So far, 1D nanomaterials have been used to prepare all sorts of devices such as supercapacitors, solar cells, LEDs and touch-screen displays. However, it is to be noted that very little attention has been paid to one of the most basic circuit components: the dielectric capacitor. Such transparent capacitors with nanostructured porous electrodes could be very easily turned into sensors: capacitive gas and strain sensors or resistive humidity and biosensors. Although some groups[3] have reported making transparent flexible capacitors, their properties have yet to be characterised. Of course, linking device geometry to properties such as capacitance and time constant is necessary in order to tune the capacitor to requirements for any types of applications.

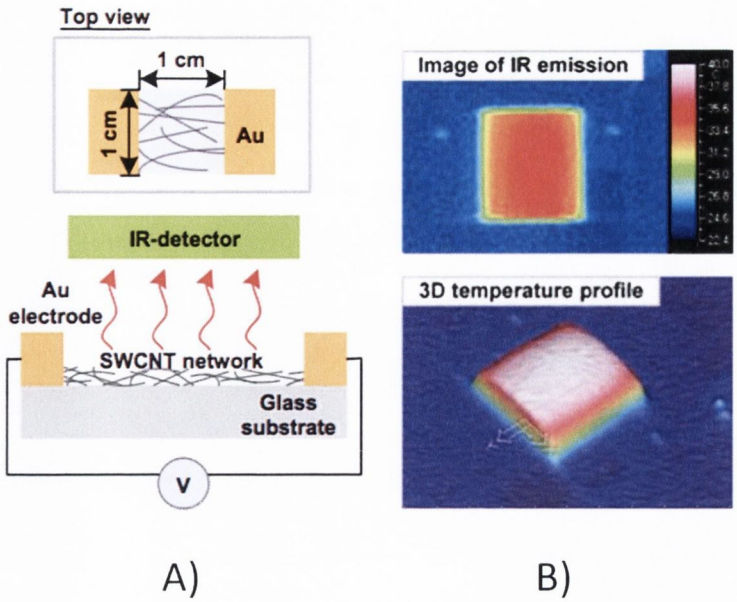

Figure 1.2: Transparent flexible heaters. Experimental setup and IR images of a Carbon nanotube network heater A) Schematic drawing of a carbon nanotube film and the setup for measurement B) IR emission images and temperature profile of a carbon nanotube network heater. [4]

Another way of taking advantage of the properties of networks of 1D nanomaterials is to note that such networks lose power through heat dissipation; this can in turn be used to make transparent flexible heaters (TFH). This simple application of transparent flexible electrodes is quite straightforward but nonetheless very beneficial for use as coatings for motorcycle helmets, car windscreens or food packaging. In fact, TFHs have become a hot topic in recent years (Figure 1.2) and some have been produced with a range of materials[5–8], however the link between the network properties and the heating time and maximum temperatures reached have never been formally established. Naturally, understanding the origins and the mechanism behind these properties is crucial for applications and must be investigated.

In light of all this, it is clear that attention must be given to the study of the influence of network and device geometry on their properties. The aim of this thesis will be to investigate complex systems by stripping them down to their core properties and characterising these as a function of dimensional changes. This will allow us in

the future to tune the properties of transparent electrodes and devices to industry requirements.

As an introduction, Chapter 2 will give an overview of the work already undertaken on silver nanowire synthesis and the properties of nanowire networks while Chapter 5 will cover the characterisation of networks of silver nanowires with different length and diameters. In Chapter 6, transparent flexible dielectric capacitors with porous electrodes will be characterised and the link between the devices' properties and their geometry will be studied. Carbon nanotubes were used in this study for proof of concept due to their low surface roughness; details of the materials and methods used are covered in Chapter 2 and 3. Chapter 7 will look into using the Joule heating of networks of silver nanowires to create transparent flexible heaters. Work on the characterisation of temperature change as a function of thin film transmittance and current applied will be covered with preliminary information being given in Chapters 2 through 4.

2

MATERIALS AND BACKGROUND

2.1 INTRODUCTION TO TRANSPARENT CONDUCTORS

Transparent conductors are materials which can form thin films of high transparency yet low sheet resistance, two properties which are highly sought after in modern electronics [9]. The first report of a thin film of transparent conductor (TC) - cadmium oxide (CdO) prepared by thermal oxidation of sputtered films of cadmium - was published in 1907 by Badeker et al. [10]. Since then, the commercial value of these types of thin films has been recognized and extensively researched [11, 12] so that today TCs are encountered as transparent electrodes in many devices. They can be found for example in glass touch-control panels etched from TC layers and flat panel displays used as smart windows in cars or aircraft [13], in organic light-emitting diodes (OLEDs) used in low power consumption and lightweight flat panel displays (FPD) [14]and also in solar cells for energy harvesting [15, 16]. For such applications, industry requires films with very high transparency in the visible range paired with a very low sheet resistance [15]. An example from the industry is Hewlett-Packard who set a target of $T = 90\%$ for $R_S = 10\Omega/\square$ for TC electrodes during their research partnership with Trinity College Dublin between *2007* and *2013* . Other factors influencing the choice of a material for TC applications are durability (physical, chemical and thermal), etchability, thickness, deposition temperature, uniformity, toxicity, and cost.

Today, the most frequently used TC materials (and the closest to fulfilling the stringent requirements above) are doped metal oxides, in particular indium tin oxide (ITO) [9, 11, 17]. ITO is an n-type semiconductor consisting of indium(III) oxide (In_2O_3) and tin(IV) oxide (SnO_2), with optimal opto-electrical properties occurring at a *90/10* atomic ratio. ITO thin films can be produced by various methods, mostly at high temperatures, including vacuum reactive evaporation [18, 19], chemical vapor deposition [20] and

sputtering [21, 22]. One major drawback of ITO is its very brittle nature. Indeed some work has shown that thin ITO films may fracture when subjected to tension or will delaminate (with or without fracturing) when subjected to compression with strains as low as 2-3% [23]. The properties controlling the fracture and delamination are the fracture toughness of the ITO and the interfacial toughness between the ITO and the substrate [1, 24]. Some companies are working on methods to solve the problem of the appearance of micro cracks within an ITO layer after repeated flexing/strain [23]. For example, an ITO on PET film can be laminated to another PET film via an optically clear adhesive; this film stack would vastly improved mechanical properties but at additional cost [25]. Another option would be to modify the ratio of indium to tin which may have some marginally advantageous effects on the film mechanical properties but the electro-optical properties would suffer. This shows that the problem of brittleness may only be avoided by switching our attention to different materials altogether. This added to the increased cost of scaling deposition to large areas due to the rising cost of indium and coupled with the relatively high sheet resistances reported for low temperature growth [26]make ITO unsuitable for future large area plastic electronics. Future displays will have to be flexible but will be required to achieve the same performances as ITO.

Several paths were followed in order to find a replacement for ITO, one of these was to fabricate transparent conductive polymers. Attention was turned towards polymers in the *1980s* when a broad range of commonly available polymers were found to exhibit high electrical conductivities via simple chemical doping mechanisms [27]. PEDOT:PSS has received the largest technical and application success. Its conductivity arises from the positive doping in its backbone which can yield conductivities of *500-1000* $S.cm^{-1}$ [28], becoming competitive with transparent conducting oxides on plastic substrates. However, this material is unstable with a decrease in conductivity when exposed to heat, humidity or UV light; furthermore, its blue/green hue makes it unattractive for transparent display applications. Because of the brittle nature of ITO, some researchers were interested in applying a polymer film to maintain electrical continuity if cracks formed within ITO films but also to use as a filler to smooth porous thin films of emerging nanomaterials [29].

More recently, the ability to controllably synthesize, purify and analyze nanoparticles has lead the way to a whole new area of material science. A lot of work has been undertaken to study the optical, electrical and thermal properties of individual nanoparticles as well as porous thin films and networks of nanomaterials. The ability of nanoscale conductors to be cast into films from solution is shifting the attention in thin film electronics away from high temperature, high vacuum, expensive processes, and towards high volume, high throughput, and solution coating methods. A few nanomaterials show great promise including carbon based materials such as graphene and carbon nanotubes, but also networks of nanowires and metal grids. The interest paid to those metals in particular is due to the high conductivity of the bulk materials allowing very thin films to display conductivities matching that of ITO. Therefore, of all the materials studied, only metallic nanowire networks have come close to surpassing minimum industry standards [30–34], displaying sheet resistance for $T = 90\%$ as low as $R_S = 49\ \Omega/\square$ for spray cast networks [33].

The metals most commonly used for these applications are silver (Ag), gold (Au) and copper (Cu). Through electrospinning, some have fabricated thin networks of copper nanowires with sheet resistances as low as $50\ \Omega/\square$ for $T = 90\%$ [34]. In order to do this, precursor nanofibres are dissolved in polyvinyl alcohol (PVA) and electrospun onto a glass substrate. They are then heated in ambient conditions in order for the copper to oxidize into CuO before being annealed in H_2 for the Cu fibers to form. PVA viscosity and spinning voltage control the diameter of the resulting nanowire and this method is easily scalable. Moreover, with this method, the lengths of the nanowires are of the order of the centimeter which brings the critical network density - the minimum density for a conductive film to form - to be up to 10^8times lower than for carbon nanotubes or silver nanowires. Furthermore, the wires fuse together during the heating process decreasing the junction resistance and lowering the overall surface roughness. However electrospun copper nanowires align during the process which unidirectionally reduces the percolation threshold. This is an advantage for some applications such as directional strain sensors but perhaps not ideal for TC applications.

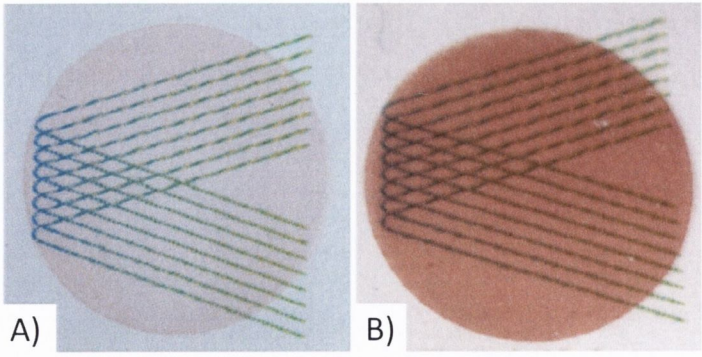

Figure 2.1: Networks of gold nanowires with transmittance A) *87%* and B) *70%*. The characteristic red tinge is noticeable even for very low thicknesses.[35]

Gold nanowires have also been shown to reach sheet resistances of only *49* $\Omega/\square$ for $T = 83\%$ [35] however as for copper nanowires, thin films display a reddish tinge which is again problematic for some TC applications such as flat panel displays or touch-screen panels (see Figure 2.1).

Of all metallic nanowires, silver nanowires have reached very low sheet resistances for high transmittance [32] and fortuitously have a light greyish colour which make thin films practically invisible to the naked eye. For these reasons, our work has focused on silver nanowire thin films and their opto-electrical properties. Although some state of the art silver nanowire networks have achieved very promising transmittance and sheet resistance, it is important to study the reason behind these incredible properties in order to enhance them. This work will therefore focus on studying the influence of the geometry of silver nanowires on the properties of the networks. Later, those networks will be used for making devices such as transparent flexible capacitors and heaters.

2.2 SILVER NANOWIRES AS TRANSPARENT FLEXIBLE ELECTRODES

2.2.1 *Synthesis and morphology*

Silver is an environmentally stable metal with atomic number *47* which possesses the highest electrical conductivity (6.3×10^7 $S.m^{-1}$) of any element and the highest

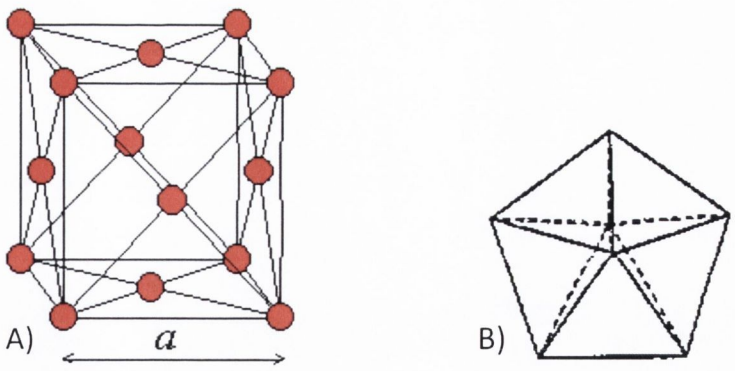

Figure 2.2: A) Unit cell for the FCC crystalline structure for silver B) A multiply twinned particle of silver with a 5-fold symmetry bound by ten {111} facets

thermal conductivity ($429\ W{\cdot}m^{-1}{\cdot}K^{-1}$) of any metal. It is stable in oxygen and water, but tarnishes when exposed to sulfur compounds in air or water to form a black silver sulfide layer. Atoms of silver form a close-packed fcc lattice as shown in Figure 2.2. Many properties of solids depend on the size range over which they are measured and the properties associated with these materials are the average of microscopic properties. Therefore, understanding the growth of metallic nanowires is vital to controlling their morphology (i.e. aspect ratio) and hence their electrical properties [36], quantum confinement properties [37, 38], surface plasmon resonance properties [39] etc. Silver nanowires can be synthesized using various methods which can be classified into two categories : the hard template or the soft solution methods.

The hard template method uses a porous template such as polymer films containing etched channels, biomolecules or porous aluminium oxide films as a mould in which to grow the nanowires [40, 41] as shown in Figure 2.3. However, the preparation and removal of the templates are costly and even though hard templates give better control over the geometry of the final product, they are harder to discard and hence the yield and quality of 1-D product is very low.

Over time it has become clear that soft solution methods are more useful for large-scale production of nanowires. The growth of metal nanowires from isotropic solutions is a challenging task because almost all metals are crystallized in the highly symmetric cubic lattice which means anisotropic confinement must be applied to induce and maintain 1D growth. The most common "polyol" method allows anisotropic confine-

Figure 2.3: Alumina membrane with etched pores as a hard-template macroporous membrane [40]

ment and was first reported by Sun et al. [42] in 2001. The synthesis follows two steps; first Pt or Ag nanoparticles (multiply twinned particles, MTP) are prepared, then a solution of $AgNO_3$and polyvinylpyrrolidone (PVP) is added to the solution containing the Pt/Ag seeds. The mixture is then heated at 160°C for 60 minutes then diluted in acetone and centrifuged to obtain purified silver nanowires. Two components are critical to the growth mechanism: the multiply twinned particles (MTP) [44] with the decahedral shape and the PVP. The MTP has 5-fold symmetry, with its surface bound by ten {111} facets (see Figure 2.2B)). A set of five twin boundaries are required to generate the decahedral particle because it is impossible to fill the space of an object of 5-fold symmetry with only a single-crystalline lattice. The twin boundary is believed to originate simply from an angular gap of $\approx 7.5^{\circ}$. The nanowires are formed in the mixture by forcing the anisotropic growth of the silver crystal around the original MTPs along their {111} facets using the PVP to block the growth along the {100} facets (PVP doesn't bond to the {111} facets due to the silver atoms' different electronic configuration)[42, 43, 45, 46]. Because a twin boundary represents the highest-energy site on the surface of an MTP, it helps attract silver atoms to diffuse toward its vicinity from the solution during the Ostwald ripening process (note: this is allowed with Pt seeds because Ag and Pt have close crystalline structure and lattice constants). Mann et

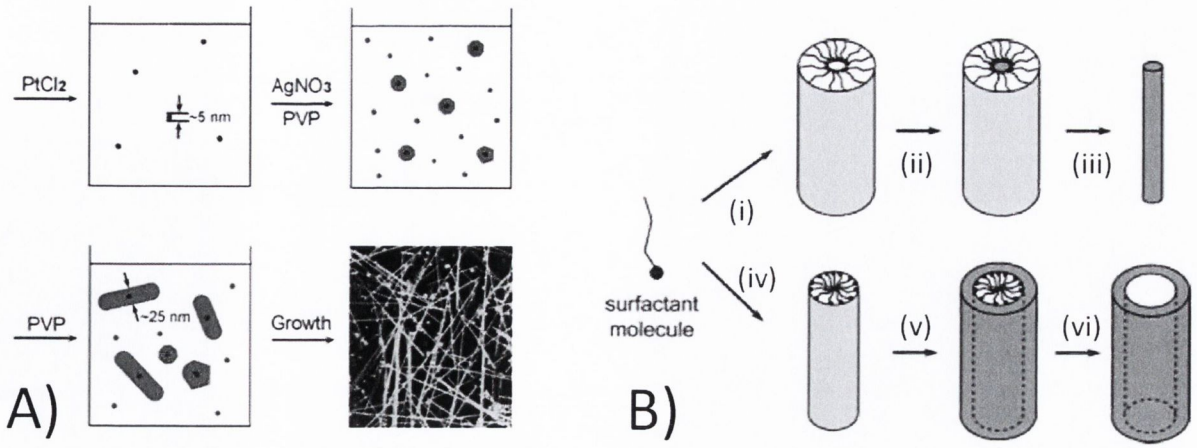

Figure 2.4: Soft solution processing of silver nanowires: A) Schematic illustration of the polyol process[43] B) Schematic illustrations showing the formation of nanowires by templating against mesostructures self-assembled from surfactant molecules: (i-iii) formation of a nanowire from aqueous phase inside a cylindrical micelle. In the case of (iv-vii) the *exterior surface* of an inverted micelle serves as the physical template[41].

al. [47] and subsequently Sun et al. [48] have proposed the mechanism for the evolution of gold and silver into 1D nanostructures as seen in the schematic illustration shown in Figure 2.5.

Furthermore, the presence of the highly polar PVP will create an effective potential surrounding the nanowires helping to stabilise a uniform solution [45]. Since then, other groups have obtained AgNWs without seeding simply from reduction of the $AgNO_3$solution in dimethylformamide (DMF) [49]. In either case, the quality and geometry of the nanowires will depend on three factors; first the size of the initial seed will control the diameter of the nanowires. Second, the reaction temperature and time will control the length of the nanowires and third the ratio of PVP to $AgNO_3$will determine whether or not nanowires will form. Indeed, a ratio of between 5 and 6 is crucial to the formation of one-dimensional nanostructures [43].

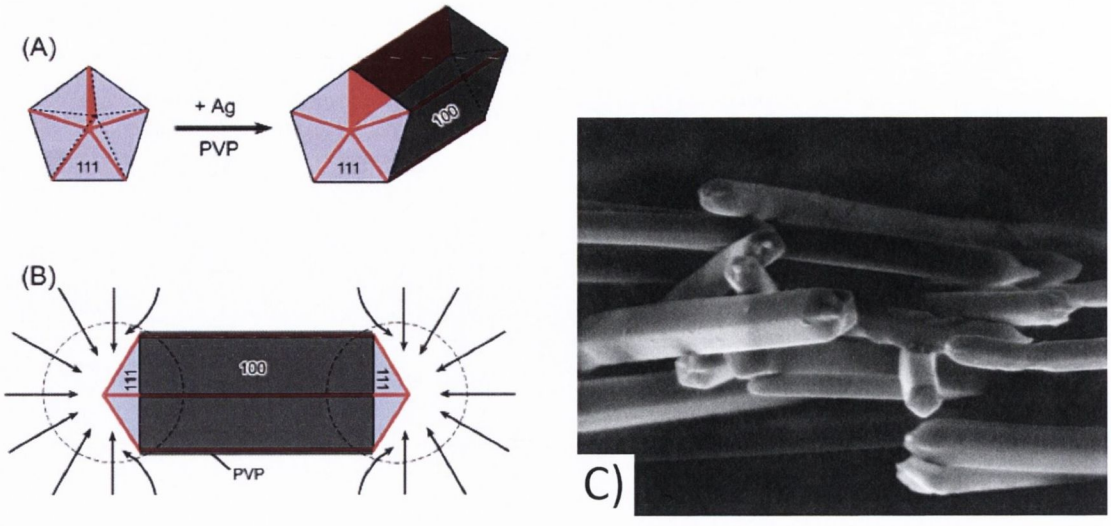

Figure 2.5: A-B) Schematics of the proposed explanation for the formation of silver nanowires via the polyol process: A) A multiply twinned particle of silver grows into a silver nanowire by forcing the growth along the {111} facets [48] C) SEM of silver nanowire films (*130 nm* in diameter), the 5-fold symmetry of the nanowires is obvious in this image (Courtesy of Dr. Philip Lyons, CRANN)

2.2.2 *Sonication induced scission*

In order to study the influence of the geometry of nanowires on the properties of the network, the influence of the length and the diameter must be isolated. This means that a method must be found to cut one-dimensional nanoparticles of a given diameter to different lengths. This is usually done by using sonication induced scission.

Acoustic waves in a liquid can form bubbles through rectified diffusion [50, 51] (see Figure 2.6) ; these bubbles will collapse very quickly when they reach a critical size which in turn creates a strong flow field in the liquid surrounding the bubble. This phenomenon is known as cavitation and has been thoroughly investigated [52–56]. In the case of a liquid containing nanowires or nanotubes, cavitation will force the fluid to accelerate along the length of the nanoparticles hence creating a drag force on the nanoparticle proportional to the velocity of the fluid. The force creates a stress which will break the nanoparticle when the stress exceeds the nanoparticle's tensile strength. This usually happens at the centre of the nanoparticle where the drag forces are at

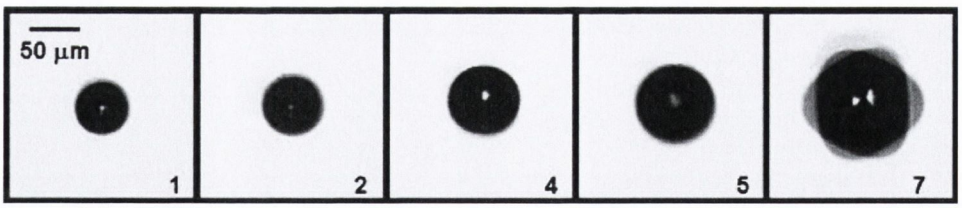

Figure 2.6: Rectified diffusion growth of a single bubble in the presence of a surfactant (sodium dodecyl sulphate, SDS) and at a pressure of 0.22 ± 0.03 bar. Each picture is taken 30 seconds apart[52].

their maximum. Martijn et al. [55] in 2004 followed by Hennrich et al. [53] in 2006 have proposed a theoretical explanation for the mechanism of sonication induced scission in the case of polymers and carbon nanotubes respectively. Hennrich also shows that in the case of single-wall carbon nanotubes, the length dependence of sonication time exhibits a power law as $L_{SWNT} \propto t^{-0.5}$.

2.2.3 *Deposition*

Many deposition methods for silver nanowires have been investigated, some more successful than others, however this is a crucial part of the process of making state of the art, new generation TCs. Here some of the main techniques will be covered and the advantages and drawbacks of each will be discussed.

2.2.3.1 *Dip coating and drop casting*

Cloutier et al. [57] have reported a method for coating glass substrate with a thin film of silver nanowires by dip-coating. The method consists of slowly dipping a *25 x 25 mm* glass sample into a solution of nanowires in isopropanol (IPA) using a mechanical dip coater. It is reported that the density of the network is controlled by the concentration of the solution and the number of dip-coated layers however there is no study formally explaining the link between these. The glass on which the film was formed was first thoroughly washed with detergent, acetone and IPA. The advantages of this technique is that the networks of silver nanowires are extremely homogeneous as shown in Figure 2.7, in addition it is easy to control the specificities of the network by controlling the

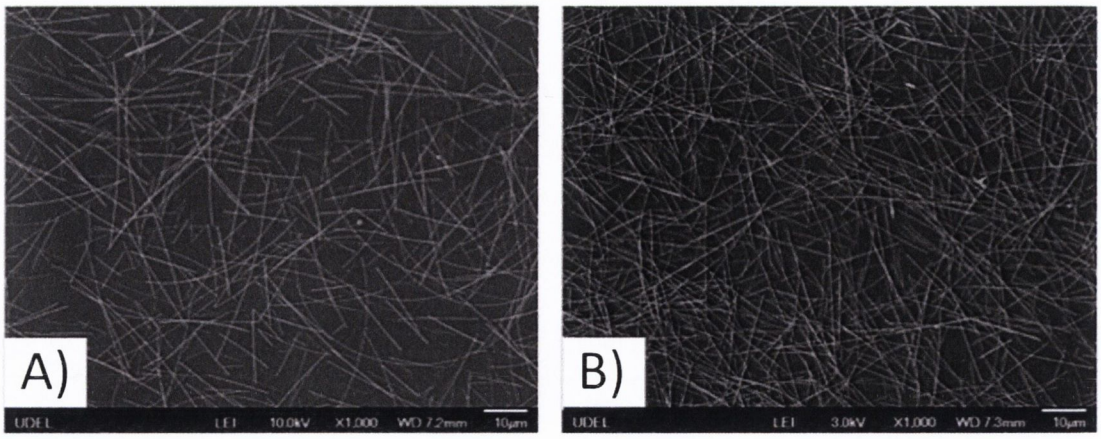

Figure 2.7: Deposition by dip coating of silver nanowire networks of various thicknesses A) T = 94.8% and B) T = 89.9%.[57]

solution concentration, speed of dipping and number of coats. However, the authors do not discuss different substrates such as Polyethylene terephthalate (PET) for flexibility and neither do they mention making thick films with $T < 60\%$. Another inconvenience is the waste of materials as the nanowires coating the reverse of the glass slide must be discarded. Along the same idea, Peumans et al. have reported a method for drop casting silver nanowires from liquid phase and simply letting it dry [31] or pulling a Meyer rod over the surface of the substrate to achieve the desired thickness [30]. Once again, network density can be controlled by the concentration of the initial solution and the number of coats. The homogeneity of the network is dependent upon drying, hence the use of a heating lamp to avoid uneven local heating.

2.2.3.2 *Dry transfer*

Another promising technique using the principle of Polydimethylsiloxane (PDMS) stamping has been studied by Madaria et al. [58]. The technique consists in filtering a solution of silver nanowires in IPA through an anodised aluminium oxide (AAO) membrane so as to form a film which is subsequently transferred onto a PDMS stamp (microcontact printing) by making "conformal" contact between the membrane and the stamp. The stamp could have been previously patterned via lithography in order to transfer a patterned film of silver nanowires. The receiving substrate is then heated at 120°C while the PDMS stamp is placed against it for 1 minute then slowly removed.

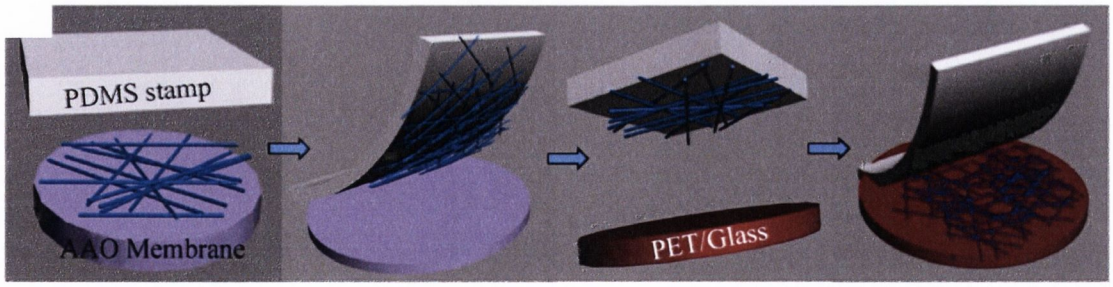

Figure 2.8: Schematic illustration of dry transfer technique by Madaria et al[58]. The network transferred via PDMS stamping cannot exceed a certain thickness past which only part of the film will be transferred.

This method exhibits serious advantages. First, the nanowires can be annealed whilst still on the AAO membrane before being transferred to a substrate, the advantage being the improvement of the electrical properties of the nanowire network (as discussed here later) . Second, the transfer process is very uniform and results in uniform density across the whole network. Finally, the film seems to adhere strongly to the underlying PET after transfer which follows the claim that noble metals, such as Au and Ag, have highly polarizable electrons, promoting strong adhesion to materials with dispersive surfaces such as PET [59]. This method is therefore very promising since it can be performed free of chemicals and at low temperatures with the possibility to pattern the networks. However, it was shown that thick films with $T < 60\%$ cannot be transferred due to decreased interaction with the substrate. Furthermore, the advantages of strong adhesion are nulled by the fact that in any case the networks must be encased to avoid oxidation. Finally, the area of printable network is limited by the size of the AAO membrane which might reveal itself difficult to translate to large area processing.

2.2.3.3 *Vacuum filtration*

The vacuum filtration method was first developed by Wu et al. [60] and was later taken up by many other research groups [32, 61–63]. This was the method used to make thin films in the initial stages of this thesis. The first step comprises vacuum filtering a dilute surfactant or solvent based suspension of nanomaterials to form a thin film of nanomaterial on a nitrocellulose porous membrane. The size of the pores will scale with the dimensions of the nanomaterial. In order to eliminate all traces

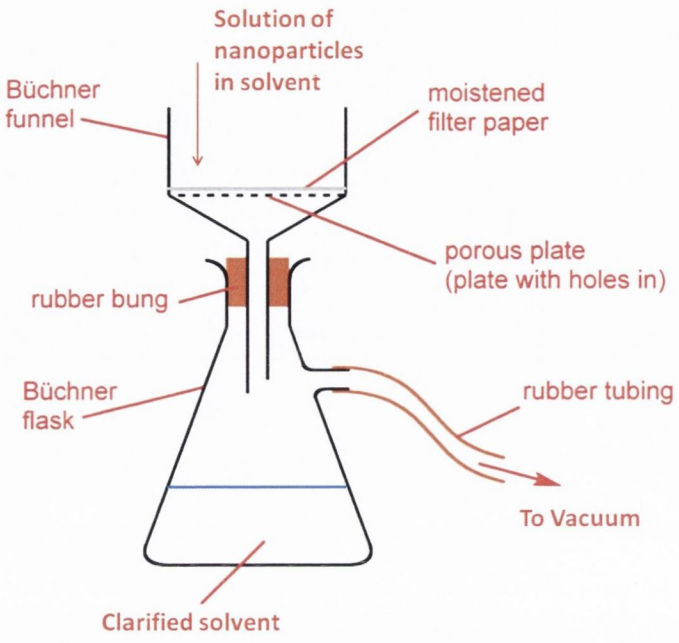

Figure 2.9: Filtration setup.

of surfactant, the film is washed with purified water. The network of nanomaterial is then transferred onto a substrate using contact, heat and a 2 *kg* weight for 2 hours to encourage the nanowires to stick to the PET. The membrane is then washed away with consecutive baths of acetone, leaving a pristine network on the substrate. The homogeneity of the film is guaranteed by the fact that as the film builds up, the thicker regions will act as a block to the solution to allow the thinner regions to catch up. Since the nanomaterials are very long, they tend to lie straight and hence gain maximum overlap. The thickness of the film is very easily controlled by the concentration and volume of solution being filtered. The main disadvantage of this method is its inability to be scaled up for industry since the size of the membrane limits the extensiveness of the networks.

2.2.3.4 *Spraying*

The method described by Scardaci et al. [33] was the method used in experimental Chapters 6 and 7 for its many advantages, namely large area processing at low temperatures, excellent control over the network density and thickness and excellent reproducibility across samples. The silver nanowires in this study were sprayed from

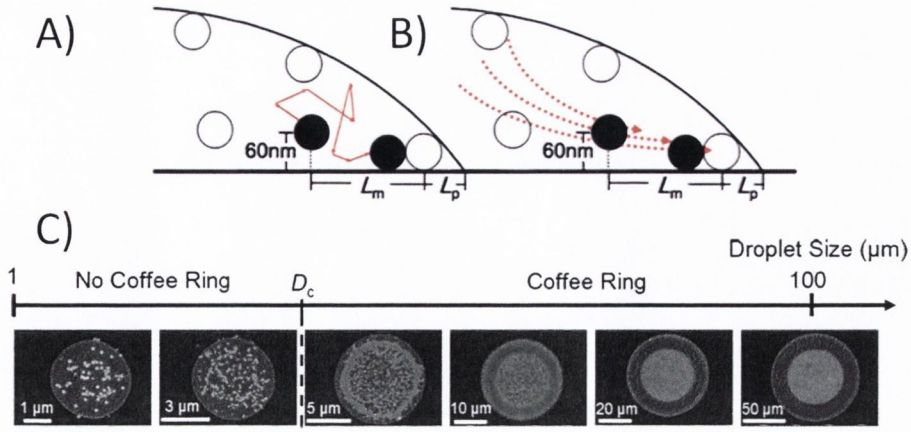

Figure 2.10: Coffee ring structure for a colloidal solution of polystyrene latex beads (surfactant-stabilized) with a particle diameter of $113\ nm \pm 11\ nm$: A) and B) Mechanisms for particle migration; A) diffusive motion and B) induced capillary flow. C) The coffee ring effect is larger as the diameter of the droplet increases i.e. for longer drying times. This means accelerating drying and decreasing the droplet diameter are necessary for homogeneous network formation while spraying (note that the image contrast of the SEM images is dependent on the local thickness of the coffee ring structure. Therefore the region of the coffee ring structures appear to be darker as the number of the nanoparticle layers increases).[65]

liquid phase onto PET at 110^0C with a cost they estimated to be about $30\ \$.m^{-2}$ which is as competitive as ITO although it is believed the price will decrease with upscaling and development. A previous paper was published by the same group in *2010 [64]* covering the influence of substrate temperature on the quality of the networks. It was found that higher temperatures were best for homogeneous networks. This can be explained by the fact that for higher temperatures, droplets deposited onto the substrate and containing nanomaterials - such as nanobeads, nanowires, nanotubes or layered 2D materials - can dry faster. This has two advantages, first as the droplet spends less time on the surface of the substrate it is less likely to coalesce with other droplets before drying which would decrease network homogeneity and reduce control over network morphology. Second, theory predicts [65–67] that in the case of a droplet lying on a substrate, nanoparticles are driven to the edges of the droplet by both particle diffusive

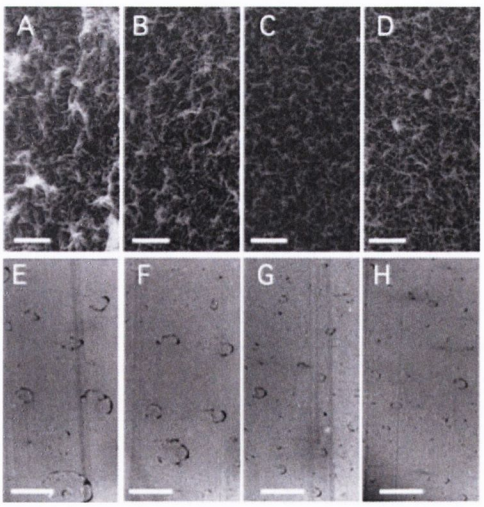

Figure 2.11: The coffee ring effect: SEM images of AgNW networks built up through multiple spray passes. In each case the network thickness is similar, with each of these networks displaying transmittance of 92–93%. Here the back pressure increases from A to D: A) *15*, B) *30*, C) *45*, D) *55* psi. In each case the scale bar is 50 μm. E–H) Optical micrographs of AgNWs deposited from individual drops following a single spraying pass.[33]

motion and induced capillary flow (Figure 2.10A),B)), creating a ring-like pattern on the surface upon drying. This is called the coffee-stain effect . The capillary flow is due to accelerated drying of the droplet at its edges, forcing a flow of liquid and thus a migration of the nanoparticles from the centre of the droplet towards the edge (see Figure 2.10). Because of this, Scardaci et al. chose to apply the highest temperature compatible with the substrate and only varied the back-pressure on the system. An increase in the back-pressure is responsible for smaller droplets and logically they observed more homogeneous networks for higher back-pressures as shown in Figure 2.11. The homogeneity of the network was closely linked to n, a percolative figure of merit for very thin network (see following section). It was observed that larger back-pressure lead to smaller n and more homogeneous networks.

2.2.4 *Network properties*

2.2.4.1 *Achieving High T and low R_S*

Following from the various deposition methods used, research groups have achieved state of the art networks of metallic nanowires [33, 57, 58, 60, 63]. Indeed, deposition is important for applications since the more homogeneous networks will display much lower sheet resistances [33]. Industry also requires high transmittance (T) and low sheet resistance (R_S) values paired with large deposition areas and low temperature processing. Each of the methods previously covered display some advantages and drawbacks but perhaps, the future of improving silver nanowire networks is in fact to choose the most industry-friendly process and to improve the network post-deposition or to design the network to the required specifications. In order to find out what the best way of improving the networks is, it must first be understood what limits the conductivity of the networks i.e. understanding the advantages and limitations of both the material itself and the network morphology. The properties of nanomaterials are determined significantly by their structure, i.e. by their dimensions, crystallinity and geometry. These parameters will in turn influence the conductivity of individual nanowires and the conductivity of the interwire junctions.

Silver nanowires have very large conductivity which in turn generate large overall network conductance. Nanowire conductivity may be altered by their geometry, indeed confinement along the nanowire diameter and scattering along the length of the nanowire if it is larger than the mean free path of the electrons [36] can make the nanowire more or less conductive. The geometry of the nanowires will also be responsible for the connectivity of the network [68] (as longer nanowires are more interconnected) and also will be partly responsible for the junction resistivity. Indeed, factors like nanowire-to-nanowire connections (which may limit the conductivity) will play a role in the network conductance and must be optimized. Moreover, a network of nanowires with high aspect ratio has extremely high transparency [69] in contrast with networks formed from other nanoparticles such as dots, where substantial coverage of the surface is needed for electrical conduction, leading to low optical transparency.

Finally, the morphology of the web-like network allows for very high mechanical flexibility. It was recently shown by Wu et al. [2] that nanowires can reversibly slide along one another while maintaining electrical contact, allowing the network to be stretched to strains greater than the fracture strain for individual wires. This is in agreement with previous work done on the mechanical stability of networks of silver nanowires [32]. This morphology also inherently allows the rearranging of conducting pathways and hence has high tolerance for the breaking of conducting paths, and therefore will be largely responsible for the networks' conductance.

It is now clear that most network properties are closely related to nanowire geometry and that this relation must be investigated in order to maximise the potential of silver nanowire networks. And indeed, in order to improve the performance of the networks, some research groups have investigated selecting the physical dimensions of the wires which maximise network conductivity and transparency. For example, it has been predicted that by reducing the wire diameter and increasing the wire length of one-dimensional nanomaterials, the network conductivity can be significantly improved [68, 70–74]. This should translate into reductions in sheet resistance for networks thin enough to have high transmittance. Some work [30, 57] has hinted towards the fact that increasing the length of the nanowires does in fact improve the electrical properties of the network. However, such improvements have not been clearly demonstrated experimentally. In addition, it is not clear whether increasing the nanowire conductivity by reducing nanowire diameter would translate into better opto-electrical performances. This is largely because it is not known to what extent varying the nanowire dimensions will affect the optical properties of the network. For example, if the network absorbance increases with decreasing wire diameter, the advantages of any conductivity increase would be largely negated. Thus, there is a large gap in research on the critical matter of understanding how both the optical and electrical properties of nanowire networks depend on the dimensions of the nanowires used.

Furthermore, for all types of nanowires, a few steps can be undertaken to improve junction conductivity post-deposition. First, the PVP leftover from the nanowire's synthesis which acts as an insulating layer between the nanowires can be removed;

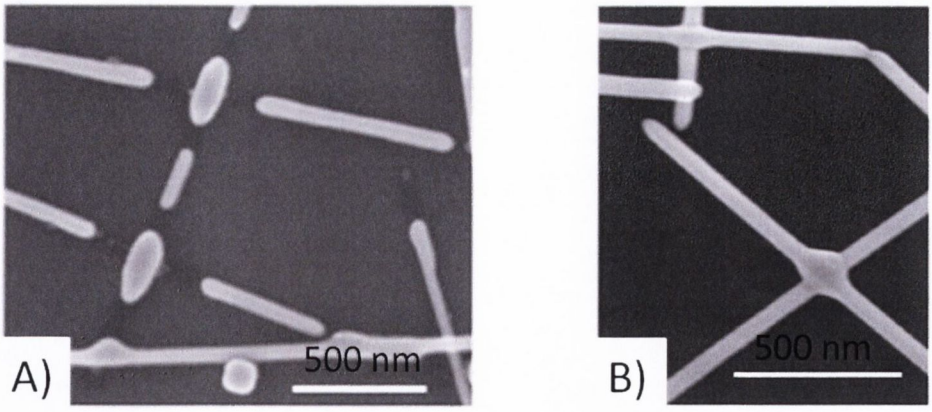

Figure 2.12: Effects of annealing silver nanowires on A) a hotplate and with B) plasmonic welding[75].

then the nanowires can be fused together. Both enhancements can be obtained by simply annealing the networks. It was reported by various groups that annealing the networks to between *120°C* and *250°C* for between *20* and *35 min* can increase the network conductivity by a factor of *10* [30, 33, 57, 58]. However several of those reports contradict each other as extreme annealing also has the effect of melting the nanowires and hence increasing network resistivity [30, 58]. No formal experimental work has been done on varying annealing temperature and time, along with nanowire diameter, as some reports suggest that large nanowires can sustain longer annealing at higher temperatures [57]. The deterioration of the nanowires due to excessive annealing can be avoided by following some light annealing to melt away excess PVP with a localised plasmonic [75], cold [76] or chemical [77] welding of the nanowires (see Figure 2.12).

2.2.4.2 *Networks of nanowires at the percolation limit*

In order to compare different deposition methods, different materials and different nanowire geometries, it is important to adopt a figure of merit common to all the systems studied. Indeed it is not enough to mention a specific pair of T and R_S as this does not describe the material, method or nanowire type over its whole network thickness range. Historically for transparent conductors, the figure of merit of choice has been the dc to optical conductivity ratio or an equivalent term [9, 78] which is easy to obtain from T - R_S data as will be shown in Chapter 3 of this thesis. This method has

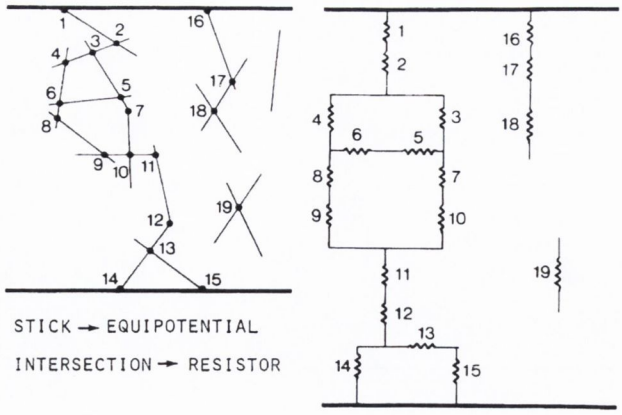

Figure 2.13: A network at its percolation threshold where each junction can be modeled as a simple resistance. This is turn allows modelling of complex networks of 1D nanostructures.[74]

been successfully used to obtain the conductivity ratio for graphene, carbon nanotube and silver nanowire networks [79]. However this approach is not complete, indeed, for one and two dimensional materials at transparencies necessary for device applications the sheet resistance increases much faster as transmittance increases. Much work has been done on trying to model the behaviour of the networks for high transparency, most of them based on percolation theory.

Electrical percolation describes the onset of electrical conductivity across a previously insulating region once conducting links have been added at a density exceeding some critical value, the percolation threshold (see Figure 2.13). For conducting rods, randomly deposited in-plane and above the percolation threshold, the conductivity follows the percolation scaling law [80–82],

$$\sigma_{DC} \propto (N - N_C)^n \tag{2.1}$$

where N is the number of rods per unit area, N_C is the percolation threshold (or critical density) and n is the percolation exponent. For the random distribution of the conducting sticks model in a square matrix, the critical density is given by

$$l\sqrt{\pi N_C} = 4.236 \tag{2.2}$$

where l is the average length of the conducting sticks. The critical exponent, n, should depend only on the dimensionality of the space; for a film in two dimensions, theory

predicts $n = 1.33$, while in three dimensions $n = 1.94$ [83], however it is well known that the percolation exponent can deviate from these universal values in the presence of a distribution of inter-wire junction resistances. The magnitude of the deviation will scale with the details of the distribution, network connectivity and homogeneity, junction resistance and nanowire geometry [80, 81, 84, 85]. Other reasons for deviations from these values are that equation 2.1 was only shown to hold for $N \to N_C$ and hence might break down for thicker networks, but also the fact that silver nanowire networks are porous and have an intrinsic fractal nature i.e. are neither truly two nor three dimensional. Some groups have found it useful to substitute σ_{DC} and N_C for more easily measurable quantities by substituting in $R_S \propto \sigma_{DC}^{-1}$ into $R_S \propto (V - V_C)^{-n}$ where R_S is the sheet resistance of the network and V is the volume of solution used in the process of making the network [58]. In this case, V_C was found experimentally as the smallest volume of solution needed to make a conducting film. Others have chosen to include the average thickness of the network as a proxy for density (assuming density does not vary with increasing network thickness) and to write $\sigma_{DC} \propto (t - t_c)^n$ where t_c is the threshold thickness. Since thickness can easily be related to sheet resistance and transmittance for thin metallic films, this final expression is the one that will be used in this work. A more complete overview in Chapter 3 will cover the use of percolation theory to describe thin films of silver nanowires.

2.3 CARBON NANOTUBES ELECTRODES FOR DEVICE APPLICATIONS

2.3.1 *Morphology and properties*

Since their discovery by Iijima in 1991[86], carbon nanotubes (CNT) have been studied extensively [60, 61, 87, 88]. With very high mobility ($10^5 cm^2 V^{-1} s^{-1}$) [89] and very promising electrical [90] and mechanical properties [91, 92], the state of the art carbon nanotubes are a contender as a replacement material for Indium Tin Oxide (ITO). Carbon nanotubes are extremely stiff, displaying Young's modulus close to *1 TPa*, and are among the world's strongest materials, with strength between *50* and *100 GPa* [93].

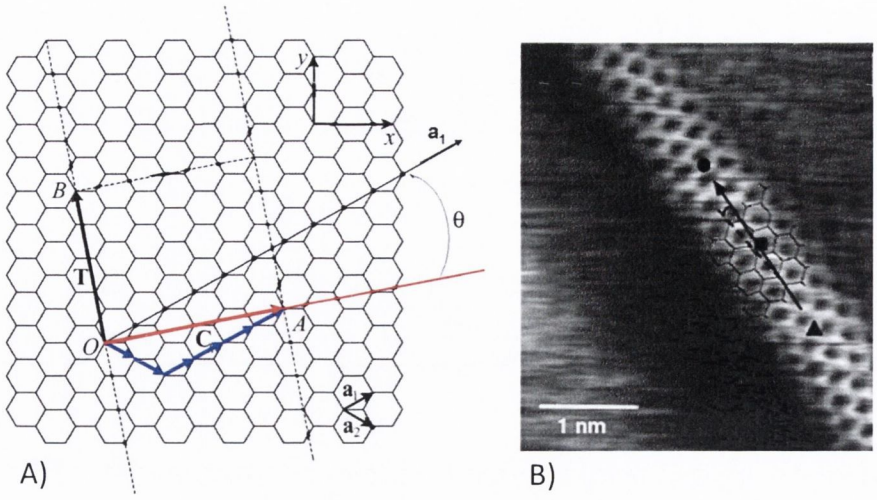

Figure 2.14: Structure of a carbon nanotube: A) The seamless rolling of a sheet of graphene along a vector C (the circumferential vector) creates a carbon nanotube. The electrical properties of the nanotube will depend on the length and direction of C with respect to the beehive lattice. B) STM image of a carbon nanotube. The tube axis is indicated with a solid, black arrow and the zigzag direction is highlighted by a dashed line. A portion of a two-dimensional graphene layer is overlaid to highlight the atomic structure[98]

They have been studied for potential device applications and nanoscale electronics, as networks for transparent electrodes but also as a component for solar cells [94], supercapacitors [95] and biological sensing [96].

Carbon nanotubes are built from a single sheet of sp^2- hybridised carbon atoms, or graphene, rolled onto itself to form a seamlessly connected tube [97] (Figure 2.14). Depending on the orientation of the rolling, the properties of the tube will change, mainly the electrical properties of the nanotube will be greatly affected by its chirality. The diameter of the nanotubes can be defined as:

$$d = \frac{\sqrt{3}}{\pi} a_{cc} \sqrt{n^2 + nm + m^2} \tag{2.3}$$

where $a_{cc} = 0.14nm$ is the carbon-bond length and n and m are the coordinates of the circumference vector in the $(\vec{a}_1, \vec{a}_2)$ plane (Figure 2.14). In the case of $n = m$ the diameter will be $d = \frac{3}{\pi} a_{cc} n$ and the carbon nanotube will be metallic [99], in any other case the carbon nanotube will be semiconducting and the bandgap is predicted to be proportional to $\frac{A_0}{R}$ where R is the nanotube radius and $A_0 = \frac{3\gamma_0 a_{cc}^2}{16}$. Here

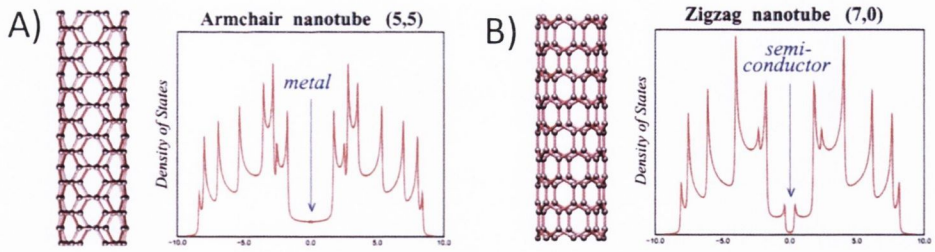

Figure 2.15: Density of states around the fermi energy E_F for A) metallic and B) semiconducting carbon nanotubes. The size of bandgap in the case of semiconducting nanotubes is proportional to the inverse of the square of the tube radius.[99]

$\gamma_0 \approx 2.7eV$ is the magnitude of the tight- binding transfer matrix element (i.e. the atomic energy shift due to the potential from neighboring atoms) [100–102] (see figure 2.15). Hence, a network of carbon nanotubes will be made of $1/3$ metallic nanotubes and $2/3$ semiconducting nanotubes. Carbon nanotubes can be single-walled (SWNT) or multi-walled (MWNT) where multi-walled carbon nanotubes are multiple concentric cylinders of graphene nested within one another precisely $0.35nm$ apart and where each shell has different sets of (n, m) coordinates (Figure 2.14). A single-walled nanotube (SWNT) can have a diameter of $2nm$ and a length of $10\ \mu m$, making it effectively a one-dimensional structure comparable to a nanowire.

2.3.2 *Synthesis*

2.3.2.1 *Chemical vapor deposition (CVD)*

CVD is the decomposition/reaction of one or more gas phase compounds which gives a non-volatile solid that builds up on a substrate. In the case of carbon nanotube the gases are a process gas (such as ammonia, nitrogen or hydrogen) and a carbon-containing gas (such as acetylene, ethylene, ethanol or methane). The substrate is prepared with a layer of metal catalyst particles where the size of the metallic particles will influence the diameter of the carbon nanotubes and is then heated at around 700^0C at ambient pressure [103]. Nanotubes grow at the sites of the metal catalyst where the carbon-containing gas is broken apart and the carbon is transported to the edges of the particle to form the nanotubes. This mechanism is not yet well understood and

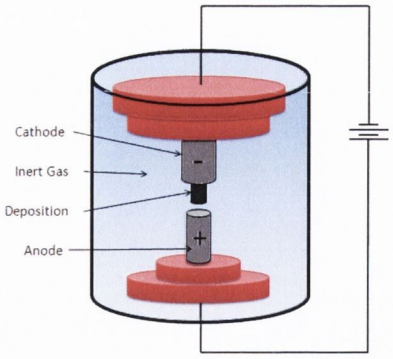

Figure 2.16: Schematics of the arc discharge process for carbon nanotubes. As a potential is applied between the anode and the cathode, a plasma is created between the graphite rods. An inert gas such as He or Ar flows through the chamber at low pressure

is still being studied [103, 104]. CVD is the most promising method of production for industry because of its low price to yield ratio and the direct deposition onto a substrate. Moreover, it is possible to choose the exact site of growth by patterning of the catalyst.

2.3.2.2 *Arc-discharge method*

As shown in Figure 2.16, this method [105] consists in placing two small diameter rods (*6 mm* and *9 mm*) made of highly purified graphite very close to each other (less than *2 mm*). An inert gas (He, Ar...) flows in the chamber at a controlled pressure while a large potential is applied between the rods. As the rods are brought closer together, a discharge occurs resulting in the formation of a plasma between the rods. The plasma causes the graphite in the smaller rod to sublimate and deposit itself in the form of carbon nanotubes and other nanoparticles onto the larger rod. The type, yield and quality of the nanotube product is dependent on the relative size of the rods, the nature and pressure of the gas, the presence of ac or dc voltage and the temperature. In order to obtain single wall nanotubes (SWNT), a metallic catalyst is added to one of the rods and the type and amount of metal will again vary the quality and quantity of SWNT. The Arc-discharge method will usually cause the growth of CNTs with fewer structural defects in comparison with other techniques.

2.3.2.3 *Laser Ablation*

Laser ablation, is one of the superior methods to grow SWNTs [106] with high-quality and high-purity. In this method, which was first demonstrated by Smalley in 1995 [107], the principles and mechanisms are similar to the arc discharge with the difference that the energy is provided by a laser hitting a graphite pellet containing catalyst materials (usually nickel or cobalt). The properties of CNTs prepared by this process are strongly dependent on many parameters such as the laser properties (energy fluence, peak power, continuous wave versus pulse, repetition rate and oscillation wavelength), the structural and chemical composition of the target material, the chamber pressure and the chemical composition, flow and pressure of the buffer gas, the substrate and ambient temperature and the distance between the target and the substrates.

Unfortunately, all these methods produce CNTs with a number of impurities whose type and amount depend on the technique used. The techniques mentioned above produce powders which contain only a small fraction of CNTs; the rest of the product collected will be a blend of other particles such as nano-crystalline graphite, amorphous carbon, fullerenes and different metals (typically Fe, Co, Mo or Ni) that were introduced as synthesis catalysts. Impurities will impair the CNTs' electrical properties and structural defects can create weaknesses for mechanical studies, therefore developing an efficient and simple purification method is important for CNT science as covered below [108]. Furthermore, in most cases the carbon nanotubes must be collected adding a level of difficulty to the process. These challenges remain and impede the rise of carbon nanotubes as a "go-to" solution to transparent flexible applications. However, CNTs' low resistivity, low surface roughness and relative low cost makes them an ideal material for the creation of inexpensive transparent flexible applications such as dielectric capacitors and other simple circuit components with less stringent requirements.

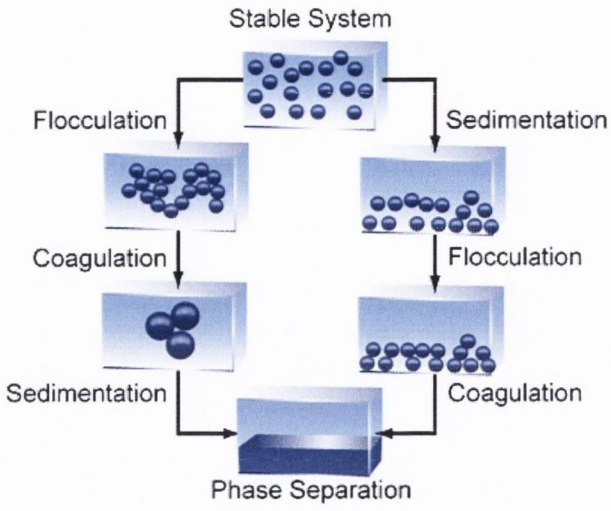

Figure 2.17: Particles in a dispersion may adhere together and form aggregates of increasing size which may sediment out irreversibly due to gravity (or vice versa).

2.3.3 *Exfoliation and deposition*

As discussed previously, the most common methods for synthesising carbon nanotubes require collecting them in powder form which favours bundling from Van der Waals interactions. Furthermore, this powder must be cleaned in order to get rid of any non-tubular nanoparticles. In order to make thin films of networks of carbon nanotubes it is therefore necessary to find a simple way to deposit a controlled amount of CNTs onto the desired substrate whilst also separating the bundles of nanotubes and ridding them of impurities. Much work has been completed in this area and one of the most successful methods, which was the one used for this work, is the liquid phase exfoliation of carbon nanotubes using a surfactant [109, 110]. Particles in a dispersion may adhere together via Van der Waals attraction and form aggregates of increasing size which may sediment out irreversibly due to gravity (or vice versa). An initially formed aggregate is called a floc and its formation flocculation; this process is reversible (deflocculation). If the aggregate changes to a much denser form it is said to undergo coagulation; this process is irreversible (see Figure 2.17).

In order to obtain a homogeneous colloidal solution of carbon nanotubes in water, the carbon nanotubes are separated using sonic energy and are prevented from reaggregating with the presence of surfactant. Indeed, the ionic part of the surfactant

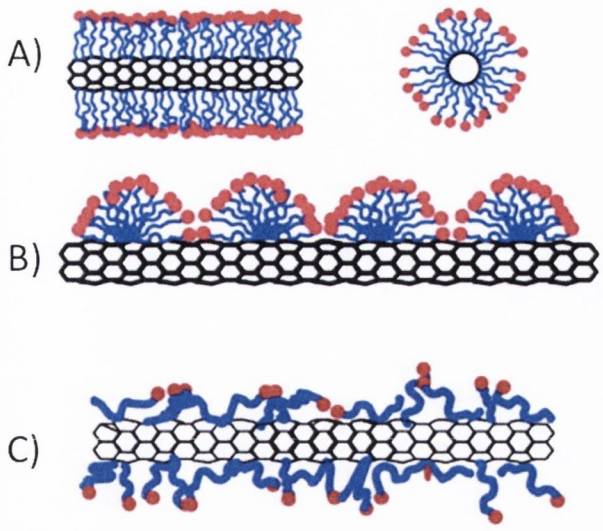

Figure 2.18: Schematic representations of the mechanism by which surfactants help to disperse SWNTs. A) SWNTs encapsulated in a cylindrical surfactant micelle (both cross section and side-view); B) hemimicellar adsorption of surfactant molecules on a SWNT; C) random adsorption of surfactant molecules on a SWNT[112].

binds with the carbon nanotubes while the counter-ions create a diffuse potential around the nanotube, discouraging other nanotubes from aggregating [111, 112]. This diffuse potential is called the zeta potential ζ and the presence of $|\zeta| < 30\ mV$ will create a stable dispersion (see Figure 2.18). The physics of the double layer was named DLVO theory, after its inventors Derjaguin and Landau, Verwey and Overbeek.

Once the carbon nanotubes have been dispersed in a surfactant solution, it is possible to separate SWNTs, large bundles of nanotubes and other impurities by centrifuging the solution (see Figure 2.19). A general approach for sorting carbon nanotubes by diameter, band-gap and electronic type (metallic versus semiconducting), using the technique of density-gradient ultracentrifugation was developed by Arnold et al. in 2006 [113]. This scalable approach exploits differences in the buoyant densities (mass per volume) among SWNTs. In this technique, purification is induced by ultracentrifugation in a density gradient. In response to the resulting centripetal force, particles sediment toward their respective buoyant densities and spatially separate in the gradient. However, for general use, it is enough to simply separate SWNTs and small bundles from large aggregates by centrifuging the carbon nanotube dispersion for 90

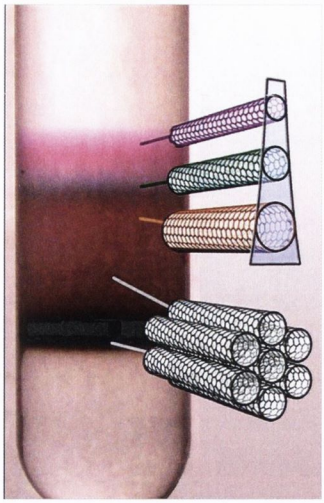

Figure 2.19: Centrifugation separation using density gradient ultracentrifugation[113].

min at *5500 RPM*. The supernatant liquid is then either quickly decanted from the tube without disturbing the precipitate, or withdrawn with a Pasteur pipette. Finally, the carbon nanotube networks can be formed using the vacuum filtration and spraying techniques outlined previously in the case of silver nanowire networks.

2.3.4 *Transparent flexible carbon nanotube electrodes*

Carbon nanotubes were one of the most promising 1D materials to be investigated for transparent and flexible networks in the aim of replacing materials that have been improving to near perfection over decades, materials such as silicon, copper, or the transparent conductor ITO. The attractiveness in all cases lies not necessarily in increased performance, but in cheap, room temperature fabrication, and attributes such as mechanical flexibility.

Much work was undertaken to study the properties of networks of carbon nanotubes and many more properties for carbon nanotube networks have been studied and explained than for silver nanowires. Unlike silver nanowires, the morphology of both the nanotubes and the networks and their influence on the opto-electrical properties of the networks have been extensively looked into [87, 114, 115]. It was reported by Stadermann using conductive tip AFM on very short length scales that discrete drops in conductance could be measured which spatially corresponded to

junctions between carbon nanotubes in a network [116–119]. The conductivity drop depended on the type of junction, metallic/metallic, semiconducting/semiconducting or metallic/semiconducting but in all cases the junction resistance is several orders of magnitude higher than the nanotube bundle resistance and hence dominate the overall network resistance.

Hecht [114] then showed that the dc conductivity scaled with the average CNT bundle length as $\sigma_{DC} \propto L^{1.46}$ in agreement with some theoretical work done by Balberg in 1983 [74] where CNT networks were modeled as a two-dimensional system of randomly distributed conducting sticks which, near percolation, displayed a dependence $\sigma_{DC} \propto L^{2.48}$. However, 2.48 acts as an upper bound in the case where network resistance is only dependent on junction resistance. Others have shown that the conductivity of CNT networks will decrease with increasing film porosity and bundle diameter [70], a model which is in perfect agreement with a study of junction resistance in the case of pristine, acid-treated and annealed SWNT bundles [87].

Networks of carbon nanotubes in the percolation regime were also extensively studied, in fact much of the research based on CNTs was used to build the foundations for studying networks of nano-scaled wires. Since the basis for the study of silver nanowire networks was extracted from literature on CNT networks, the properties of percolative carbon nanotube networks will not be a reviewed to avoid repetition. Furthermore, because of the very-well known properties and low surface roughness of carbon nanotube networks these were the ideal candidate for the second part of this work: using porous, transparent and flexible electrodes for device applications.

2.3.5 *Transparent flexible capacitors and capacitive sensing*

With the scientific community's attention monopolized by supercapacitors, very little work has been carried out on transparent, flexible dielectric capacitors (TFC). In fact, only one paper mentions the production of a transparent flexible dielectric capacitor with flexible carbon nanotube electrodes to be used as a skin-like pressure and strain sensor [3]. Some capacitive sensors made from copper electrodes and PDMS dielectric

were also made, acting as a flexible, though non-transparent, dielectric capacitor [120] and some transparent and flexible pressure sensors were recently produced for touch screen applications using Indium Zinc Oxide (IZO) and polycarbonate dielectric [121]. However, the characterization of the properties of TFC as a function of device morphology has never been tackled. Although the motivation behind this work was to use porous electrodes to build transparent and flexible capacitors to be used in the field of transparent flexible electronics, a byproduct of these capacitors with porous electrodes is their ability to be used in the area of capacitive humidity sensing. Indeed, the porous nature of CNT electrodes allows for small molecules to travel through them in order to interact with the dielectric layer of the capacitor. These devices could be very useful in the case of biosensors, where the sensor needs to blend in with and follow the movements of a patient's skin. Furthermore, detection of the concentration of a specific gas molecule in mixtures of various gas molecules is increasingly required for control and monitoring of various industrial or medical processes.

Capacitive-type sensors have good prospects given that the capacitor structure is so simple, enabling miniaturization and achieving high reliability and low cost. The principle of capacitive sensing is usually to choose the dielectric in the device to be sensitive to a range of gas or liquid analytes. Little so far is known about the fundamentals of capacitive type chemical sensors, in particular, gas sensors based on capacitance change, though it can be assumed that the analyte will interact with the dielectric in various ways [122–126]. It can, for example, cause swelling of the dielectric, affect the dielectric constant of the new system or affect the resistance of the porous electrode as it comes in contact with it, all of which will affect the measured capacitance of the system. It is therefore very important to characterize the properties of transparent flexible capacitors with nanostructured electrodes in order to control those properties for applications.

2.4 TRANSPARENT FLEXIBLE HEATERS (TFH)

When an electric current flows through a solid or liquid with finite conductivity, electric energy is converted to heat through resistive losses in the material. The heat is generated on the micro scale when the conduction electrons transfer energy to the conductor's atoms through collisions; this phenomenon is called joule, resistive or ohmic heating. Transparent flexible heaters are an interesting application to transparent flexible nanostructured electrodes simply based on joule heating at the junctions in the network.

Transparent heaters have already been developed and are in production [127, 128] using either ITO sputtered on a polyester film or using a micro wire heating element laid in a pattern between two clear substrate materials. Transparent heaters are designed to work with LCD panels, windows, mirrors, solar panels, camera lenses, touch screens or any application that requires light or visual transmittance in cold and moist environments. However, both ITO and micro-wires display weaknesses; ITO is brittle and will not be useable in the case of flexible applications and wires do not heat the substrate homogeneously. This is why attention has been turned once again towards materials such as metallic nanowires, carbon nanotubes and graphene which give a homogeneous coverage of the substrate while remaining transparent and flexible.

The matter of joule heating in networks of nanowires has already been tackled, mainly because in very resistive, industrially relevant networks, current density is very high and represents a problem when it comes to electromechanical stability of devices [129]. Figure 2.20 illustrates how very thin networks of silver nanowires will fail over time if current densities are high enough. Although silver nanowires have small diameters and display some small intrinsic defects, including interfaces and dislocations, it is believed junctions are mainly responsible for joule heating. The power dissipation which happens mainly at the nanowire/nanowire junctions is proportional to the current and resistance of the network as $P = I^2R$ and is partly responsible for network failure in percolative films [7, 130]. Khaligh et al. showed through SEM imaging of nanowires that after annealing or after network failure, the nanowires

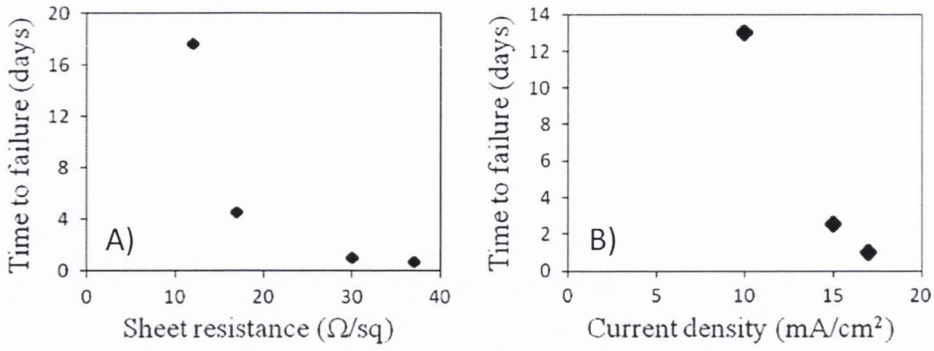

Figure 2.20: Dependency of time to failure on resistance and current density in the case of a thin network of metallic nanowires. A) The number of days to failure versus sheet resistance, when conducting *17 mA.cm^{-2}* across samples with different resistances B) The relationship between the number of days to failure and current density, as measured with three different *30* Ω/□ electrodes. [129]

displayed the same morphological alterations, furthering the claims that heating is responsible for network failure [129]. This shows that it is important to understand and characterise the temperature increase of nanowire network as a function of current applied and network density in order to avoid network failure and to be able to use these networks for transparent flexible heater applications.

2.4.1 *Heating devices in the literature*

Transparent flexible heaters made from one or two dimensional nanomaterials have started emerging as recently as *2007*, led by carbon nanotubes thin [6] and thick films [131]. Carbon nanotubes were chosen for their extraordinary thermal conductivity of nearly *3500 W/mK*, extreme thermal stability for temperatures as high as *3200 K* in vacuum [130, 132] and emissivity close to *1* [6, 133]. The research was focused on proving the concept of carbon nanotube networks as heaters and less so on understanding the link between network properties and temperatures attained. However, as the interest grew for those simple devices so did the amount of research. In 2010, Jang et al. [134] published work on the dependence of power input on maximum achieved temperature. They reached the conclusion that temperature increased as power applied increased;

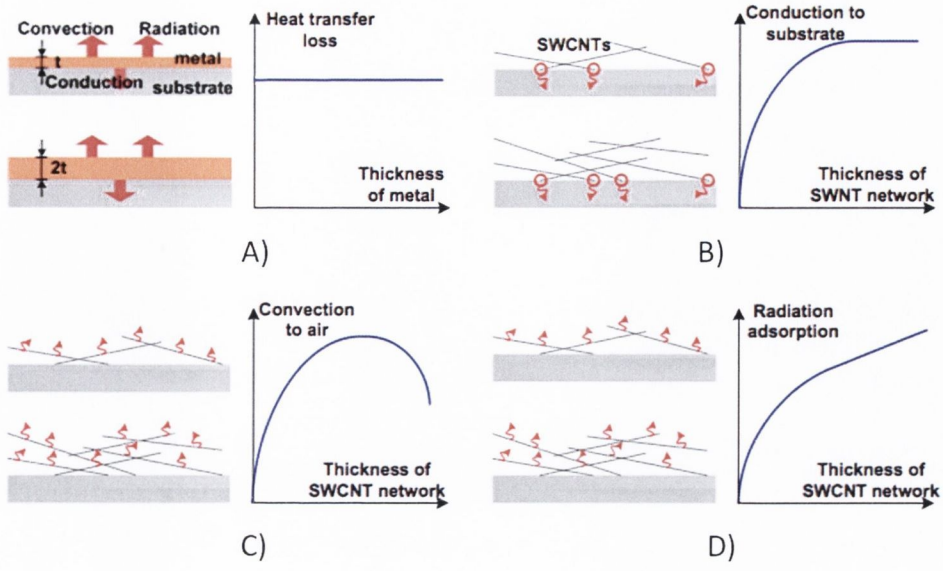

Figure 2.21: Understanding the mechanism for heat loss dependency with the change in film thickness. A) Heat losses of a conventional film heater (Pt thin film). B) Conduction. C) Convection. D) Radiation losses of the SWCNT network heater.[5]

this make sense since increasing the power input is done by increasing the current which in turn allows for more electrical energy to be converted into heat. In 2010, Kang et al. [5] characterised the temperature response of carbon nanotube heaters as a function of network resistance (at room temperature) and applied voltage. It is pointed out that the power input depends on V and R as $P = V^2/R$ and that the thin films can be characterised by the heat generation as a function of input power dT/dP. Though what is interesting about this paper is that for the first time the mechanism of heating is tackled and explained as a function of radiation, convection and conduction i.e. a stable temperature occurs when the heating power compensates for the heat loss at the interfaces (air and substrate). (see Figure 2.21).

Heat transfer through conduction is believed to happen at discrete points of contact of the SWNTs with the substrate which means that as the film grows thicker, the heat loss through conduction increases rapidly (Figure 2.21 B)). The second heat loss mechanism is convection through air which, they suppose, will have a larger effect in very thin films (Figure 2.21 C)). Finally, some heat loss is attributed to radiation

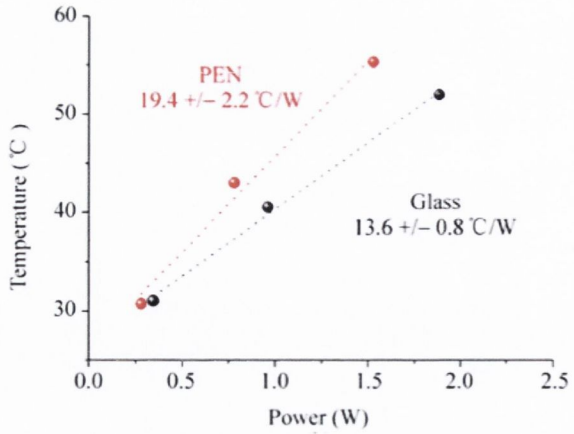

Figure 2.22: Input power as a function of the steady state temperature of a network of silver nanowires deposited onto poly(ethylene naphthalate) (PEN) and glass substrates[7]

which will decrease as the film thickness increases as SWNTs have very high optical absorption properties [133] (Figure 2.21 D)).

Although SWNTs are an excellent candidate for TFH applications, a lot of attention has been given to graphene in the last few years. Indeed, the outstanding thermal conductivity of graphene films [135–138] provides another advantage for using graphene in transparent heaters. As it delivers heat quickly to the environment, the result is a faster heating rate and a more homogeneous temperature distribution additionally to the low surface roughness and homogeneous coverage intrinsically provided by the morphology of graphene thin films. Furthermore, since the temperature depends on the morphology of the film, the desired temperature can be set by modifying the sheet resistance using chemical doping and varying the thickness of the graphene film [8, 139].

Finally, and as for most transparent flexible applications, a couple of articles [7, 140] have very recently been published on TFHs made from silver nanowire electrodes as a logical continuation from carbon based nanomaterials for their very high conductivity ratio $\frac{\sigma_{DC,B}}{\sigma_{Op}}$, comparable to that of ITO. In *2012*, the first AgNW TFHs were reported from Celle et al. [7]. Silver nanowires seemed to behave quite similarly to carbon-based materials although the maximum temperatures were achieved after much longer times (*200 sec* for AgNWs against *60 sec* for SWNTs and graphene) which can be a result of silver's much lower thermal conductivity compared to SWNTs and graphene. The

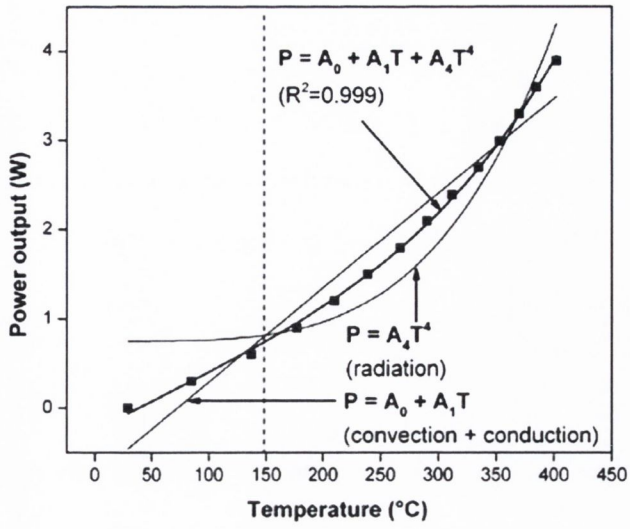

Figure 2.23: Fitting of heat exchange mechanisms governing heat exchange from the surface of a perpendicularly-aligned CNT film[141]

same paper also shows how the substrate has an effect on the temperature achieved, which means heat conduction through the substrate is an important part of the process (Figure 2.22) in agreement with previous theories for SWNT films. Indeed, heat disperses more rapidly when a material has a high thermal diffusivity value. At 50 °C, the thermal diffusivity of the substrates used are about 1.5×10^{-7} m^2/s, for poly(ethylene naphthalate) (PEN) and 5.9×10^{-7} m^2/s for glass. These values indicate that heat transfer is lower with the PEN substrate and thus heating rate and steady state temperature are both slightly higher when compared with the glass substrate. This paper also reported that applying too high a voltage will destroy the networks due to melting of the nanowires which is an inconvenience for applications where highly transparent percolative networks must be used.

Although much work has been undertaken to create state of the art flexible and transparent heaters for a whole range of applications, too little effort has been put into understanding exactly the mechanism behind these nanostructured porous heaters. Within the last few months, some work has arisen on the theory of heat transfer in TFHs. Janas et al. [141] have in March of this year published work on CNT thin films as heaters. The film was suspended while surface temperature was monitored with a thermal camera. They report that, assuming complete conversion of electric power

into heat, fitting of the data (Figure 2.23) revealed two regimes of heat evolution. The lower regime is convection to air and conduction to the supporting quartz slides. Then radiative emission starts to dominate at about *150* °C and at temperatures higher than *400* °C one could see a very faint red glow of the hot surface. Another paper [139] published last July states some of the basic equations of thermodynamics and heat convection and radiation in order to obtain an expression for time dependent temperature.

In this work, networks of silver nanowires will be studied in order to fill the gaps in the understanding of the time-dependent behaviour of the networks during the heating process and the dependence of the saturation temperature on the current applied and thickness of the nanowire network.

3

THEORY

3.1 NETWORKS OF ONE-DIMENSIONAL NANOMATERIALS

3.1.1 *Electrical and optical properties of thin metallic films*

3.1.1.1 *Electrical properties*

In the scientific quest to find a new transparent flexible conducting material, metallic nanoparticles were always an attractive option. Metals are characterised by high electrical conductivity brought on by the fact that a large number of electrons in a metal are free to move about. Those free electrons are called conduction electrons, i.e. the valence electrons of the atom become the conduction electrons of the metal. The characteristic feature of metallic binding is the lowering of the energy of the valence electrons in the metal as compared with the free atom. This comes from the fact that metals crystallise in relatively close packed structures: hcp, fcc, bcc...[142] The Drude model of electrical conduction was proposed in 1900 by Paul Drude to explain the transport properties of electrons in conductive materials. The model assumes that the microscopic behavior of electrons in a solid may be treated classically, meaning that electrons are assumed to travel a distance λ (the mean free path) in a straight line in the solid before being scattered by (and loosing most of their momentum to) a much larger immobile positive ion on the crystal lattice (see Figure 3.1) . Therefore, it is possible to model the behaviour of electrons in a metal by assuming they behave like an ideal gas of particles of mass m and velocity v_d associated to temperature of the gas. Electrical current density under an applied electric field, E , can then be written as

$$J = -eNv_d = \frac{e^2 N\tau}{m} E = \sigma E \tag{3.1}$$

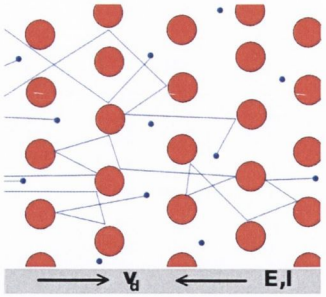

Figure 3.1: Drude Model electrons (shown here in blue) driven by an electric field E constantly bounce between heavier, stationary crystal ions (shown in red)

where σ is the conductivity of the material, N is the number of electrons with charge $-e$ per unit volume and τ is the time between collisions of the electrons with impurities, lattice imperfections and phonons within the crystal. Furthermore, the current density is by definition the current per cross sectional area

$$J = \frac{I}{A} \tag{3.2}$$

and the potential drop along a line of length l in an electric field E is

$$V = El \tag{3.3}$$

$$V = \frac{I}{A}\rho l \tag{3.4}$$

$$V = RI \tag{3.5}$$

also known as *Ohm's law*, where the resistance is $R = \rho\frac{L}{A}$. In a thin film, $A = wt$ where t is the thickness of the film and w is the width of the film, therefore

$$R = R_S\frac{l}{w} \tag{3.6}$$

where by definition

$$R_S = \frac{1}{\sigma t} \tag{3.7}$$

is called the *sheet resistance*. The concept of sheet resistance is applicable to films thin enough to be considered as two-dimensional entities. Although sheet resistance should have the same units as resistance, its unit is in fact taken as $\Omega/\square$ to indicate that the value is that of a unit area of material. Here, σ is the dc conductivity of bulk silver and will be symbolised from now on by $\sigma_{DC,B}$.

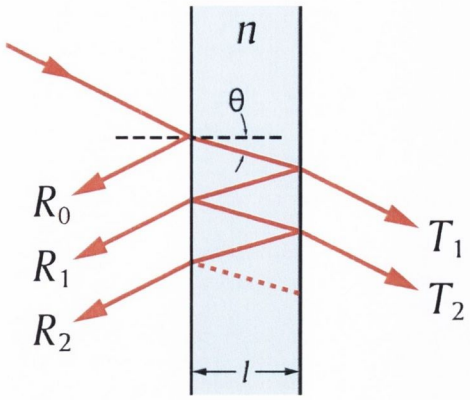

Figure 3.2: For a a thin semitransparent material with thickness $l \ll \lambda$, multiple reflections and transmission arise causing interference.

3.1.1.2 *Optical properties*

In a thin metallic film, the evaluation of the amplitude and phase of the electromagnetic wave is lengthy but straightforward, although only the end result will be given here. Indeed, if the film is very thin then incident light will be subjected to multiple reflection and transmission before exiting the film as shown on figure 3.2 By calculating the multiple reflections and transmissions at the two symmetrical boundaries (given by $z = o$ and $z = l$), assuming the thickness of the metallic film is lower than the wavelength of visible light and that the film is optically conductive, the transmittance of light can be approximated as[143]

$$T = \left(1 + \frac{Z_0}{2}\sigma_{op}t\right)^{-2} \tag{3.8}$$

Where σ_{Op} is the conductivity of the material as light interacts with it - or the optical conductivity. The definition of sheet resistance (equation 3.7) can be subbed in

$$T = \left(1 + \frac{Z_0}{2R_S}\frac{\sigma_{op}}{\sigma_{DC,B}}\right)^{-2} \tag{3.9}$$

The ratio of dc to optical conductivity, $\frac{\sigma_{DC,B}}{\sigma_{Op}}$, is a figure of merit used widely in the area of transparent networks of nanotubes/nanowires where a larger ratio will lead to better opto-electrical properties. Note that equation 3.8 is analogous to the Beer-Lambert law, $T = e^{-\alpha t} = e^{-\alpha(\sigma_{DC,B}R_S)^{-1}}$, expanded to first order with $\sigma_{Op} \approx \alpha/Z_0$. In fact, a more popular figure of merit in the field of transparent conductors is $\frac{\sigma_{DC,B}}{\alpha}$ [9, 79], however the form of equation 3.8 will be more usefull in this work.

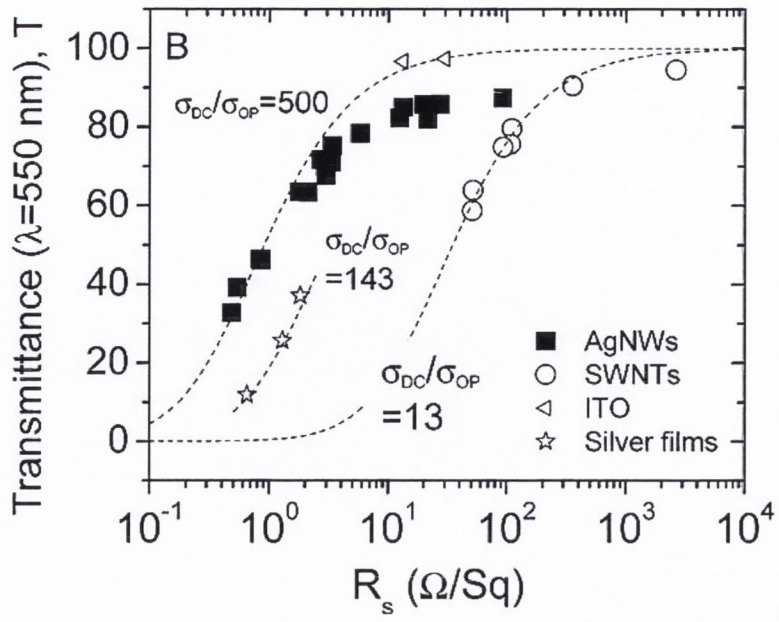

Figure 3.3: Transmittance ($\lambda = 550nm$) plotted as a function of film sheet resistance for networks of silver nanowires and carbon nanotubes as well as evaporated silver and commercial ITO. This work by De et al. shows that equation 3.9 fails to describe the data accurately at high transmittance in the case of networks of one-dimensional nanostructures. [32]

3.1.2 *Characterisation of a percolative network*

The above definition of transmittance as a function of sheet resistance describes the properties of thin metallic films very well when those thin films have thicknesses above a certain critical thickness t_{min}. However this theoretical model deviates for films with thickness below this threshold as shown in Figure 3.3. This is easily understood for networks of one-dimensional materials with very few connective paths. Indeed, as the number of paths decreases the conductivity will decrease extremely fast. Likewise, as more links are added, new conducting paths are formed and the conductivity increases rapidly. The transmittance on the other hand will remain more or less unaffected by the change in available conductive paths. This phenomenon is called *percolation* and has been studied extensively in the areas of mathematics (computer connectivity, social networking) [144–146], chemistry [147] and biology (epidemics) [148–150].

Percolation can be discussed in terms of probability, the probability that a conductive path will be present between the two sides of a network as more nanowires are added to the network. The probability at which a conductive path occurs is called the *percolation threshold*. The behaviour at thicknesses greater than a few nanometers is distinct from true percolation however, percolation-like conductivity scaling has been observed for a number of systems far from the percolation threshold[32, 35, 79, 95, 151, 152]. This can be considered as an intermediate system between true percolation and bulk behaviour. Theoretical work has been done on the percolative behaviour of networks of rods and it was found that at thicknesses near percolation (from above) the conductivity of the network follows

$$\sigma_{DC} \propto (N - N_c)^n \tag{3.10}$$

where N is the number of rods per unit area, N_C is the percolation threshold (or critical density), n is the percolation exponent which would only depend on the dimensionality of the space in the case of true percolation (see Chapter 2, section 2.2.3) and σ_{DC} is the conductivity of the percolative network, different to $\sigma_{DC,B}$. For this study, it is more convenient to talk about the thickness of the network rather than the number density of wires making up the network. The number of rods per unit area can be written as

$$N = \frac{m_N}{m_{nw}} \frac{1}{A} \tag{3.11}$$

$$= \frac{m_N}{A} \frac{1}{\rho_{nw} \langle V_{nw} \rangle} \tag{3.12}$$

$$= \frac{At\rho_N}{A} \frac{1}{\rho_{nw} \langle V_{nw} \rangle} \tag{3.13}$$

$$= t \frac{\rho_N}{\rho_{nw} \langle V_{nw} \rangle} \tag{3.14}$$

where m_N is the mass of the network, $m_{nw}$the mass of a nanowire, ρ_{nw} is the density of a nanowire, V_{nw} is the average volume of a nanowire, A is the surface area of the film and ρ_N is the thin film density[70, 79] (note that due to high porosity, $\rho_N \neq \rho_{nw}$). Therefore, the effective thickness of the film can be written as

$$t = \frac{N \langle V_{nw} \rangle \rho_{nw}}{\rho_N} \tag{3.15}$$

$$= sN \tag{3.16}$$

This can be subbed into equation 3.10 by writing

$$\sigma_{DC} \propto s^{1/n} (N - N_c)^n \tag{3.17}$$

$$\propto (sN - sN_c)^n \tag{3.18}$$

This means that we can write the conductivity of percolative films proportionally to film thickness as

$$\sigma_{DC} \propto (t - t_c)^n \tag{3.19}$$

For industrially relevant films, $t \gg t_c$ meaning $(t - t_c) \sim t$, therefore

$$\sigma_{DC} = kt^n \tag{3.20}$$

where k is a proportionality constant. σ_{DC} increases with increasing thickness until it reaches its bulk value, $\sigma_{DC,B}$, at $t = t_{min}$, meaning

$$\sigma_{DC,B} = kt_{min}^n \tag{3.21}$$

or

$$k = \frac{\sigma_{DC,B}}{t_{min}^n} \tag{3.22}$$

allowing us to write

$$\sigma_{DC} = \sigma_{DC,B} \left(\frac{t}{t_{min}} \right)^n \tag{3.23}$$

Let's recall that the sheet resistance, R_S , is a function of network conductivity, which is now dependent on network thickness, and can be written as

$$R_S = \left(\sigma_{DC,B} \left(\frac{t}{t_{min}} \right)^n t \right)^{-1} \tag{3.24}$$

$$R_S = \left(\sigma_{DC,B} t_{min} \frac{t^{n+1}}{t_{min}^{n+1}} \right) \tag{3.25}$$

This new expression for the sheet resistance as a function of network thickness can be subbed into equation 3.8 in order to get a percolative equivalent

$$T = \left[1 + \frac{Z_0}{2} \sigma_{Op} t_{min} \left(R_S \sigma_{DC,B} t_{min} \right)^{-1/n+1} \right]^{-2} \tag{3.26}$$

$$= \left\{ 1 + \frac{1}{2} \left[\frac{\left(Z_0 t_{min} \sigma_{Op} \right)^{n+1}}{R_S \sigma_{DC,B} t_{min}} \right]^{1/n+1} \right\}^{-2} \tag{3.27}$$

$$= \left\{ 1 + \frac{1}{2} \left(\frac{Z_0}{R_S} \right)^{1/n+1} \left[\frac{\left(Z_0 t_{min} \sigma_{Op} \right)^n}{\sigma_{DC,B} / \sigma_{Op}} \right]^{1/n+1} \right\}^{-2} \tag{3.28}$$

This can be rewritten as

$$T = \left[1 + \frac{1}{\Pi}\left(\frac{Z_0}{R_S}\right)^{1/n+1}\right]^{-2} \tag{3.29}$$

where Π is the *percolative figure of merit*

$$\Pi = 2\left[\frac{\sigma_{DC,B}/\sigma_{Op}}{\left(Z_0 t_{min}\sigma_{Op}\right)^n}\right]^{1/n+1} \tag{3.30}$$

Equations 3.9 and 3.29 are used to describe the behaviour of thin silver nanowire films in Chapters 5 and 7. The change in bulk and percolative figures of merit will be studied as the geometry of the nanowires are varied.

3.2 TRANSPARENT FLEXIBLE CAPACITORS WITH NANOSTRUCTURED ELECTRODES

3.2.1 *Transparent polymer for dielectric applications*

A polymer is a macromolecule composed of many repeated subunits[153], known as monomers, which are usually composed of a string of - CH_2- groups paired with various side groups. These side groups are what affect the polymers' properties most. In this study, poly(vinyl) acetate (PVAc) was used as the polymer for the dielectric layer of the capacitors, the structure of PVAc is shown in Figure 3.4. In order to create the capacitor's dielectric layer, PVAc must be dissolved into a solvent in order to use it in the liquid phase. PVAc is soluble in many solvents, including acetone, tetrahydrofuran, methanol, ethanol or toluene. In order for a polymer to mix in a solvent the Helmholtz (F) free energy of the system must be minimised i.e. the entropy, S, must be maximised as the internal energy, U, is minimised. This is well described by Hansen solubility parameters (HSP)[154] where materials with similar HSP have high affinity for each other. HSPs cover three types of interactions, the atomic (or dispersive) interactions, the permanent dipole–permanent dipole interactions and hydrogen bonding. The basic equation governing the assignment of Hansen parameters is that the total cohesion energy, E, must be the sum of the individual energies that make it up

$$E = E_D + E_P + E_H \tag{3.31}$$

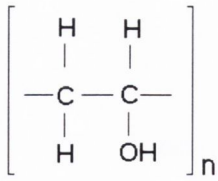

Figure 3.4: Polyvinyl alcohol structure

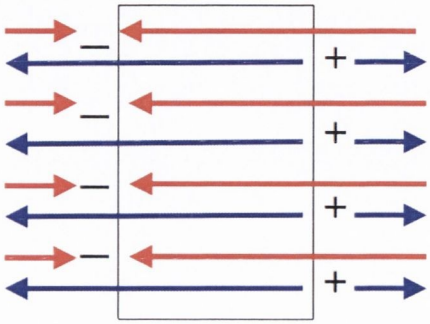

Figure 3.5: Effective electric field inside the polymer due to charges on the plates of a capacitor

where E_D is the dispersive energy, E_P is the polar cohesive energy and E_H is the cohesive energy source in hydrogen bonding. The solubility parameters are individually defined as

$$\delta = \sqrt{\frac{E}{V}} \tag{3.32}$$

where V is the molar volume. This means the square of the total solubility parameter can be written as the sum of the squares of the D, P, and H components.

$$\delta^2 = d_D^2 + \delta_P^2 + \delta_H^2 \tag{3.33}$$

For a polymer to dissolve in a solvent, their individual Hansen parameters (δ_D, δ_P, δ_H) must match as closely as possible.

In capacitors an electric field interacts with the bound electrons in the dielectric as shown in figure 3.5. The electron cloud is forced off-centre from the polymer's molecular core hence creating dipoles throughout the material. The total electric field in the polymer is then the applied field minus the induced polar field and the polarisation can be written

$$\mathbf{P} = \varepsilon_0 \left(\varepsilon_r - 1\right) \mathbf{E} \tag{3.34}$$

Using the electric susceptibility, we can also write

$$\varepsilon_r = 1 + \chi_e \tag{3.35}$$

The dielectric constant ε_r is a property of the polymer and varying ε_r will vary C.

3.2.2 *Basics of Impedance spectroscopy*

For this study, networks of various nanomaterials such as carbon nanotubes and silver nanowires were sprayed on either side of a thin film of insulating polymer in order to produce dielectric capacitors. To study these devices, *impedance spectroscopy* was used. It is well known that the current flowing through a resistive element in a circuit will follows Ohm's law:

$$I = \frac{V}{R} \tag{3.36}$$

However, in more complex circuit elements and under an applied ac potential, the behaviour of the electrical response will vary with varying frequency. Similarly to resistance, impedance is a measure of the ability of an element to resist current in such a case where the electrical response is frequency-dependent . Electrical impedance is normally measured using a small excitation signal. This is done so that the cells' response is pseudo-linear as shown in Figure 3.6. In a linear (or pseudo-linear) system, the current response to a sinusoidal potential will be a sinusoid at the same frequency but shifted in phase. However, the signal must be large enough so that the current response is larger than the margin of error of the setup. The excitation signal expressed as a function of time has the form

$$V_t = V_0 sin(\omega t) \tag{3.37}$$

where V_t is the excitation voltage at time t, V_0 is the amplitude of the signal and ω is the radial frequency. The relationship between the radial frequency (*rad/s*) and the frequency (*Hz*) is

$$\omega = 2\pi f \tag{3.38}$$

In a linear system, the response I_t is shifted by an angle φ and has amplitude I_0

$$I_t = I_0 sin(\omega t + \varphi) \tag{3.39}$$

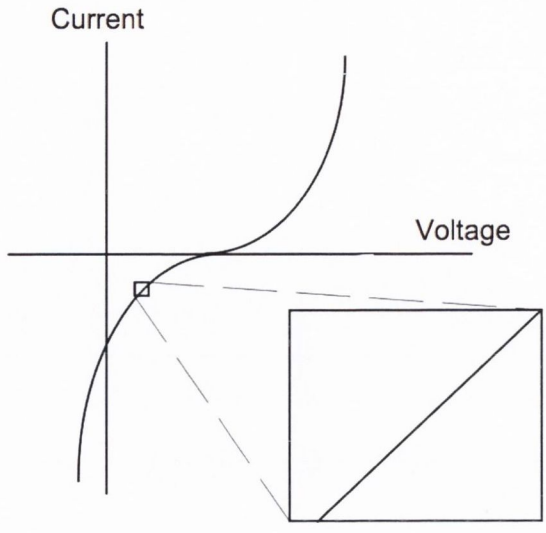

Figure 3.6: In the case of a non-ohmic system, the current response to an applied ac voltage is non-linear as shown here. However, if the voltage applied is very small the current response appears to be linear as shown in the inset. This pseudo-linear behaviour means we can assume that the input consists of the weighted sum of several signals, then the output is simply the superposition (weighted sum) of the responses of the system to each of the signals.

hence the impedance can be expressed in terms of its magnitude Z_0 and a phase shift between its various components φ. If the applied sinusoidal signal V_t is plotted on the x-axis of a graph and the sinusoidal response signal I_t on the y-axis, the result is an ellipse (or oval) for a linear system (see Figure 3.7). This oval is known as a Lissajous figure and provides information on the type of circuit that is being dealt with in addition to information on I and V. If the system is not linear, i.e. the frequency of the current response is different to the frequency of the applied potential, the resulting curve will be a three dimensional knot and for an ohmic system, the Lissajous curve will be a line ($\varphi = o$). Figure 3.7 illustrates various possibilities for a linear system.

The impedance of the system is represented as a complex quantity

$$Z = Z_0 exp\,(i\varphi) \tag{3.40}$$

where the amplitude Z_0 represents the ratio of amplitudes of the voltage and current and φ is the phase shift between I and V. Alternatively, Euler's formula

$$exp(i\psi) = cos(\psi) + isin(\psi) \tag{3.41}$$

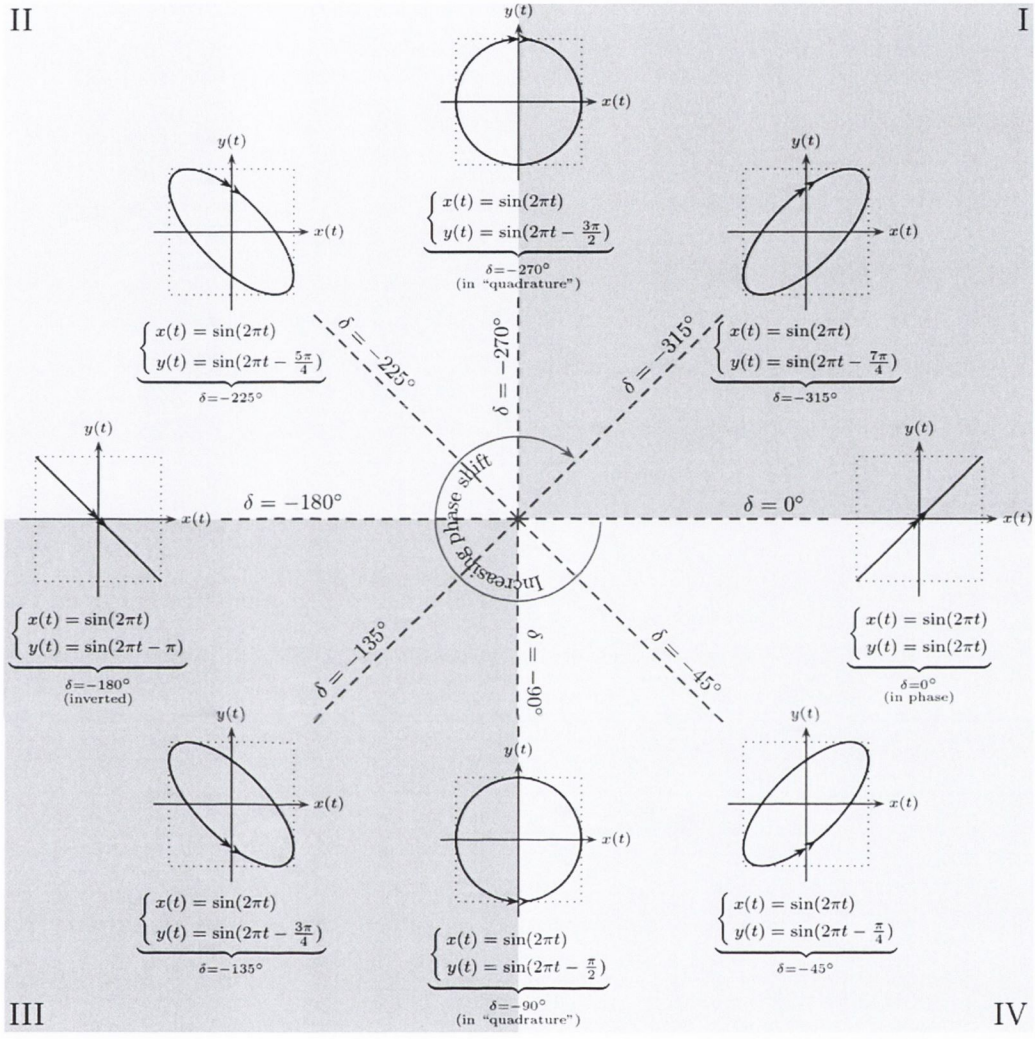

Figure 3.7: Lissajous curves deliver information about what type of circuit is being tested. Indeed the shape of the curve carries information on the presence and the weight of an imaginary component to the impedance. For example, a resistor which only has a real component will display a linear Lissajous curve. On the other hand, the current through a capacitor will lag the voltage by $\pi/2$ radians, the Lissajous curve will in this case be a circle.

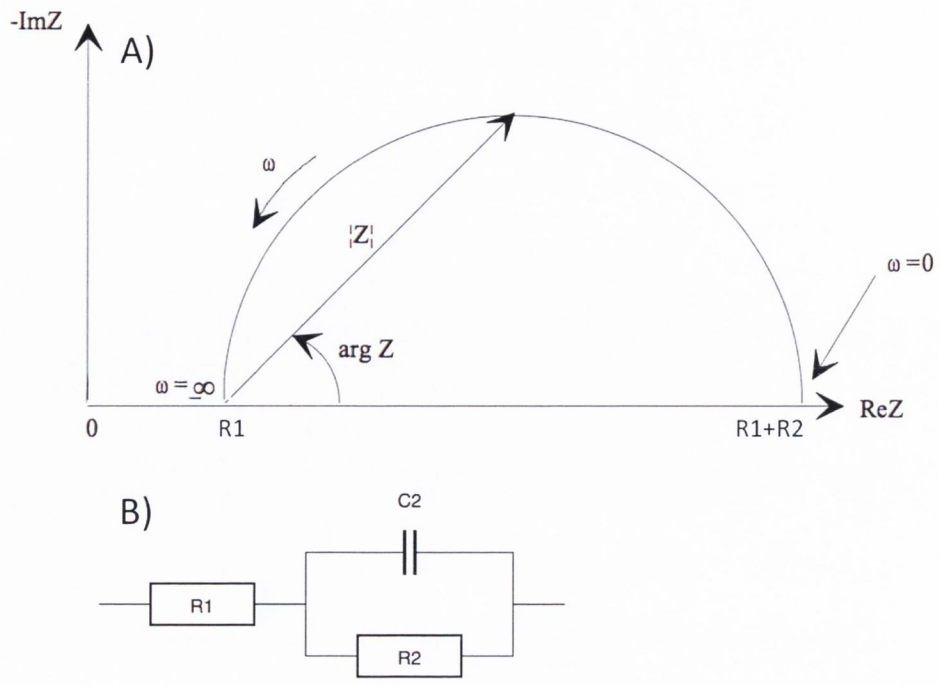

Figure 3.8: A) Nyquist plot for an RC parallel circuit: the semicircular shape is typical of these circuits. The semicircular shape arises as the frequency increases and has for diameter the amplitude of the series resistance in the circuit. B) The RC parallel circuit corresponding to the above Nyquist plot

allows us to write

$$Z = Z_0[cos\varphi + isin\varphi] \tag{3.42}$$

showing that the impedance is composed of a real part and an imaginary part. It is possible to extract the nature of the circuit studied from the nature of the real and imaginary parts of the impedance. Each equivalent circuit will display a typical Nyquist plot, i.e. a plot of imaginary impedance versus real impedance therefore Nyquist plots are important for matching devices to their equivalent circuit. On the Nyquist Plot the impedance can be represented as a vector (arrow) of length $|Z|$ as shown on Figure 3.8 . The angle between this vector and the x-axis is the phase angle, φ $(= argZ)$, discussed previously.

Although they provide a very useful set of information, Nyquist Plots have one major shortcoming. When looking at any data point on the plot, one cannot tell what frequency was used to record that point; therefore it is essential that the information be represented in a different format. Bode plots describe the information more thoroughly

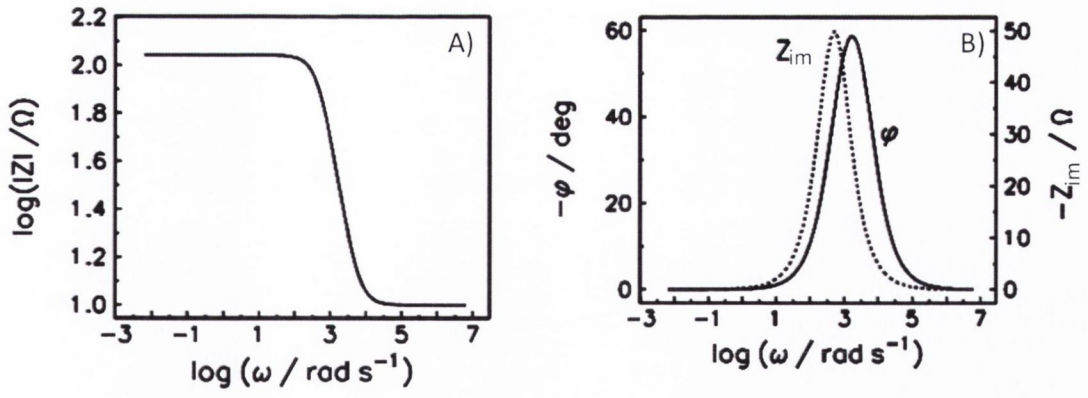

Figure 3.9: Typical Bode plots for parallel RC circuit (as seen in Figure 3.8). A) Magnitude of the impedance as a function of frequency, the shape of the curve can be related to the type of circuit using first principles of impedance as shown in Chapter 5. B) Phase versus frequency, the phase goes to o for low frequency as reactance term becomes negligible.

by separating the information about the phase and the information about the amplitude of the impedance and by showing frequency information (Figure 3.9).

3.2.3 *Series RC circuits*

The samples in this study would ideally exhibit behaviours typical of a series RC equivalent circuit. This means that the device would not present a leaking current created by a short between the electrodes across the dielectric layer. If a short was present, the Nyquist and Bode plots would be that of a parallel RC circuit as shown in Figures 3.8 and 3.9.

NYQUIST PLOT In the case of an RC series circuit, the impedance is equal to

$$Z = R_{Ser} + X_C \tag{3.43}$$

where X_C is the *capacitive reactance*. As a potential is applied to a capacitor, the current response is equal to a constant C, the capacitance, multiplied by the rate of change of voltage per unit time:

$$I_t = C\frac{dV_t}{dt} \tag{3.44}$$

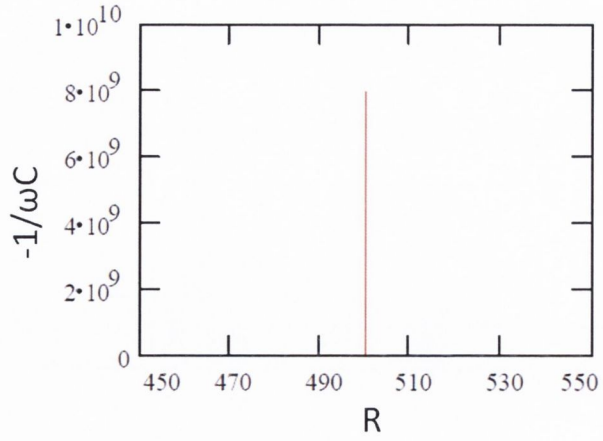

Figure 3.10: A series RC circuit will have a Nyquist plot displaying a typical Delta function because the series resistance, R, is frequency independent while the reactance, $X_C = 1/\omega C$, is frequency dependent.

As seen above, the voltage can written as $V_t = V_0 exp(i\omega t)$ and therefore, the current becomes $I_t = i\omega C V_0 exp\,(i\omega t)$. Substituting this into the equation for Ohm's law (equation 3.5) leads to

$$X_C = \frac{V_0 exp(i\omega t)}{i\omega C V_0 exp\,(i\omega t)} \tag{3.45}$$

Or

$$X_C = \frac{1}{i\omega C} \tag{3.46}$$

This allows us to write

$$Z = R_{Ser} - i\frac{1}{\omega C} \tag{3.47}$$

where R_{Ser} is the real part of the impedance and $1/\omega C$ is the imaginary part of the impedance. This means that the Nyquist plot will be composed of a series of points with identical x-component equal to R_{Ser} but different y-component depending on the frequency at which the impedance is measured. This means that if the nyquist plot for a device is a delta function then this device is known to behave like an RC series circuit (Figure 3.10).

BODE PLOT As before, if the device behaves like an RC series circuit it will have impedance

$$Z = R_{Ser} - i\frac{1}{\omega C}$$

where the modulus of the impedance will be equal to

$$|Z| = \sqrt{R_{Ser}^2 + (1/\omega C)^2} \tag{3.48}$$

Likewise, the phase in the case of an RC series circuit can be obtained by using Pythagoras' theorem in the imaginary plane (Figure 3.8) allowing us to write:

$$\varphi = tan^{-1}\left(\frac{1}{\omega RC}\right) \tag{3.49}$$

The Bode plots for such a circuit should therefore allow us to extract the values for the phase and the modulus of the impedance. The method for obtaining R_{Ser}, C and the time constant, $\tau = RC$, from the Bode plots will be outlined in experimental Chapter 6.

3.3 THERMAL CONDUCTIVITY OF THIN SILVER NANOWIRE NETWORKS

3.3.1 *Theoretical models for heat transfer*

Thin film heaters work on the simple principle that in a resistive circuit element electrical power gets dissipated as heat. This is called Joule heating and the pattern of heat flow through a material from such heating mechanism follows a few principles. First, in the case of a direct current, the power dissipated (electrical energy being converted to thermal energy) follows Joule's law:

$$P = IV \tag{3.50}$$

And in the case when Ohm's law is applicable, Joule's law can be rewritten as

$$P = I^2R = \frac{V^2}{R} \tag{3.51}$$

Heat will then travel through and away from the thin film following a few principles outlined in recent papers [139, 141]. First, let us note that in heat transfer analysis, a body is said to behave like a "lump" if its interior temperature remains essentially uniform at all times during a heat transfer process. The temperature of such bodies can be taken to be a function of time only, $T(t)$. Heat transfer analysis that utilizes this idealization is known as lumped system analysis. In the case of silver nanowires,

lumped system analysis is assumed to be applicable so that the temperature remains uniform within the body at all times and changes with time only, *i.e.* $T = T(t)$. Let's consider a thin metallic film of mass m and specific heat c_p initially at a uniform temperature T_o. At time $t = 0$, (T=T_o) a current is applied to the film and heat transfer takes place between the body and its environment. During a differential time interval dt, the temperature of the body rises by a differential amount dT. Then, the net transfer of heat into the body over a time dt will be

$$dQ = mc_p dT \tag{3.52}$$

In any system, the overall driving force for heat flow processes is the cooling (or leveling) of the thermal gradients within this system. As shown in Chapter 2, radiation and convection are the two main heat transfer mechanisms playing a role in the stabilisation of the surface temperature of TFHs. All bodies constantly emit energy by a process of electromagnetic radiation and the intensity of such energy flux depends upon the temperature of the body and the nature of its surface. Radiation is a consequence of thermal agitation of the molecules composing the heated material and this type of heat transfer can occur in vacuum. Heat transfer through radiation can be described by a reference to the so-called *black body*. A black body is a body which absorbs all energy that reaches it and reflects or transmits nothing. The energy radiated from it per unit time is described by the *Stefan-Boltzmann law* of black body radiation

$$P_{blackbody} = A\sigma T^4 \tag{3.53}$$

where A *is* the surface area of the system, T is the temperature of the body and $\sigma = 5.6703 \times 10^{-8} W.m^{-2}.K^{-4}$ is the Stefan-Boltzmann constant. However, a system that does not absorb all incident energy can still be described by the Stefan-Boltzmann law with the introduction of the *emissivity*, ε. For a black body, $\varepsilon = 1$ while for an infinitely reflective surface $\varepsilon \to 0$. Therefore, the Stefan-Boltzmann law can be applied to TFHs and can then be rewritten as

$$P_r = \varepsilon\sigma A \left(T^4 - T_0^4\right) \tag{3.54}$$

where $\varepsilon < 1$. The addition of the T_0 term accounts for the fact that as the system radiates heat into its environment, the environment radiates heat back into the system.

The second heat transfer mechanism in play, convection, is the transfer of heat by mass motion of a fluid from one region of space to another. In the case of TFHs, *natural convection* is at play with the flow being caused by differences in density due to thermal expansion upon heating of the air. Indeed, when cool gas flows past a warm body, as air in the case of TFHs, the fluid immediately adjacent to the body forms a thin slowed-down region called a *boundary layer*. Heat is conducted through this layer and into the gas stream, increasing its temperature and causing it to displace. The Stefan-Boltzmann-law implies that the heat dissipation through radiation will be maximised at high temperatures, therefore convection will be largely responsible for cooling the device at lower temperatures. For a lumped system, the heat lost through convection per unit time is described by *Fourier's law* as

$$P_c = hA\,(T - T_0) \tag{3.55}$$

where h is the convective heat transfer coefficient, A *is* the surface area of the system and T_0 is the temperature of the surrounding air. Following these basic principles, the formal study of the heat loss mechanism in the case of silver nanowire networks will be covered in experimental Chapter 7.

4

CHARACTERISATION AND METHODS

4.1 INTRODUCTION

In order to characterise the properties of networks of nanomaterials and devices, it was necessary to develop a method to produce samples in a reproducible manner and which would lead to good quality networks. With that in mind, filtration was the method used for the study of the properties of nanowire networks whereas spraying of the nanostructures onto the substrates for enhanced sample-to-sample continuity was used subsequently. Once the samples were made, a series of steps were taken to characterise their optical and electrical properties. This chapter will cover the techniques used.

4.2 SILVER NANOWIRE FILMS THROUGH FILTRATION

For the purpose of this study, silver nanowires were purchased from Seashell Technologies [155] as suspensions in isopropyl alcohol. A small volume of the dispersion was diluted down to *0.001 mg/mL* with Millipore water. This was subjected to a few minutes low power sonication in a sonic bath (Model Ney Ultrasonic). Silver nanowire films were prepared by vacuum filtration of the above dispersions using porous mixed cellulose ester filter membranes (MF-Millipore membrane, mixed cellulose esters, hydrophilic, 0.2 μm, 47 mm). As the solvent fell through the pores of the membrane, the nanowires were trapped on its surface, forming an interconnected network. The density of this network (nanowires/area) could be controlled with high precision by simply controlling the volume of dilute suspension filtered through the membrane. The deposited films were transferred to a polyethylene terephthalate (PET) substrate using heat and pressure [60]. The PET was then heated at *100* °C and the AgNW

film/membrane was placed on the PET face down. A 3 *kg* weight was then placed on top of it for 2 hours. The cellulose filter membrane was then removed by treatment with acetone vapor and subsequent acetone liquid baths followed by a methanol bath [60, 156]leaving a pristine film with a diameter of 36 *mm*. This method has the benefit that the speed of the vacuum filtering process does not permit wire flocculation, creating optically homogeneous films. Another factor helping with homogeneity is that the denser regions act as a blockade to fluid flow through the filter, allowing rarer regions to accumulate tubes. The method is inexpensive and scalable to larger areas. The drawbacks are the possibility of an uneven film if the filtration surface isn't perfectly horizontal and the relatively long sample preparation time. Furthermore, as the thickness builds up for very thick films, suction may vary which in turn will affect stacking which means the film density/porosity might diverge from that of thinner films. A diagram of the setup is shown in Chapter 2, Figure 2.9.

4.3 SPRAYING

In Chapters 6 and 7, samples were made using spray deposition for both carbon nanotube and silver nanowire electrodes. The advantages of spray deposition over other methods are the capacity for large area processing, low cost, homogeneity within a sample and very good reproducibility [33]. The mechanics of spraying are rather simple, a very sharp needle is inserted into a nozzle of diameter between 150μm and 600μm depending on the size of the material being sprayed. As the needle is withdrawn from the nozzle an annulus forms between the needle and the nozzle. A solution of nanomaterials in a solvent can then run down the needle and escape through the annulus. Nitrogen is directed at a high pressure through a gap around the annulus, forcing the liquid to atomise as shown in Figure 4.1.The size of the droplets will depend on the pressure of the nitrogen pressure (see Chapter 2, section 2.2.3). The quality of the final network depends on a number of parameters such as solution concentration, scan speed, airbrush height, flow rate, back pressure and substrate temperature. Substrate temperature and back-pressure are critical for the drying dynamics of droplets once

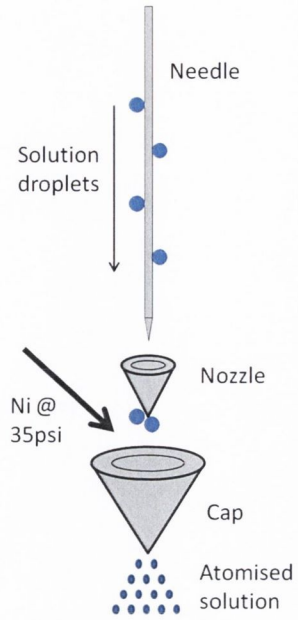

Figure 4.1: Diagram of the workings of the spray pen. The solution runs down along the needle which is inserted to a certain depth into the nozzle. The size of the annulus created dictates the flow rate. Nitrogen at high pressure flows between the nozzle and the cap, atomising the solution into a spray.

they reach the surface[33, 65–67] as covered in Chapter 2, section 2.2.3. The setup used in this study was a Harder & Steenbeck infinity airbrush secured to a JANOME JR2300N robot as shown in Figure 4.2. Spraying was performed with a solution of either CNT in surfactant or AgNW in IPA, both at $0.15\ mg.ml^{-1}$. The back-pressure used was between 30 and $55\ psi$ and the flow-rate was $2.5\ mm^3.s^{-1}$. The nozzle used had a diameter of $150\mu m$ in the case of carbon nanotubes and graphene, and $600\mu m$ in the case of silver nanowires. The temperature applied was limited by the substrate itself, from 110^0C for PET to several hundred degrees for glass. The silver nanowires were purchased from Seashell[155] while the carbon nanotubes were purchased from Iljin[157].

4.4 OPTICAL SPECTROSCOPY

Light interacts with matter in different ways depending on its composition, for example, some metals are shiny while glass is transparent and rubies are red. When light

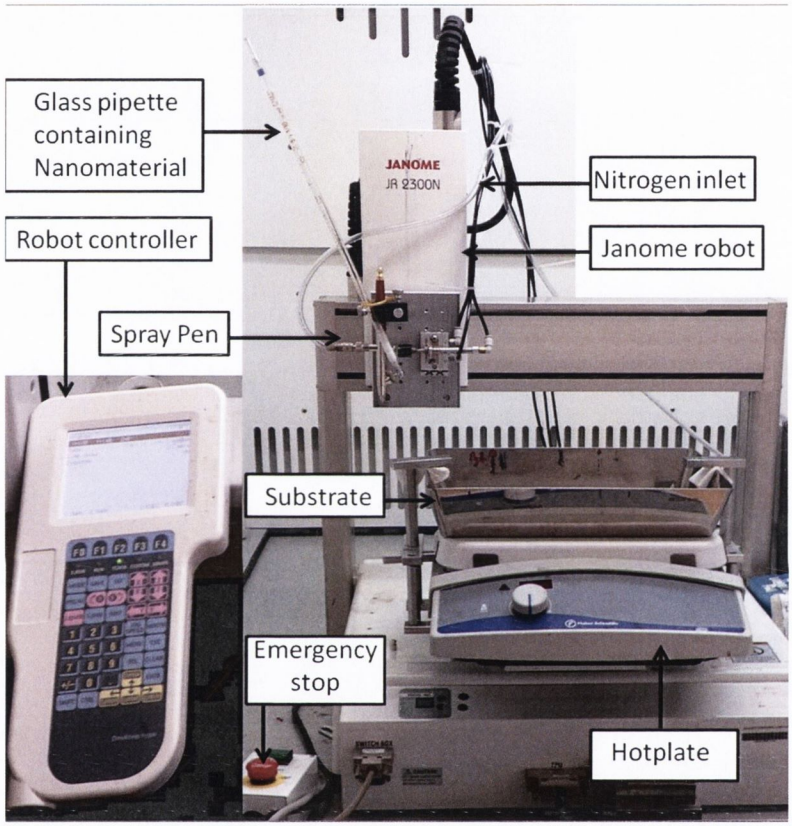

Figure 4.2: Sprayer setup: The spray pen is secured to a Janome robot and can spray patterns onto the substrate. The solution of nanomaterial is introduced to the pen via a glass pipette secured to the pen through the use of parafilm. The substrate (PET, Si, Glass etc...) can be heated to help the formation of homogeneous networks

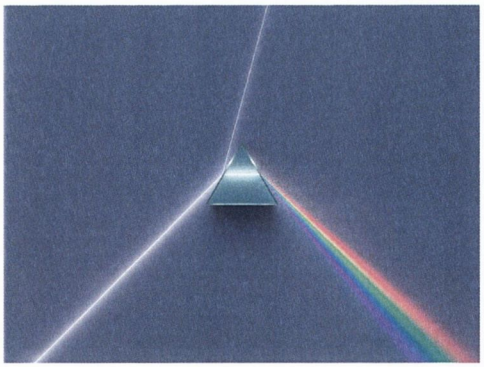

Figure 4.3: Propagation of light through a transparent medium. The incident light is reflected, transmitted and refracted.[158]

interacts with matter most optical phenomena will fall under one of three categories, namely reflection, propagation and transmission (see Figure 4.3). Furthermore, propagated light can be scattered, absorbed, or refracted by the atoms inside the material but all with the same final result, the decrease in how much light is transmitted through the sample. The absorption of light by an optical medium is quantified by its absorption coefficient α, defined as the fraction of the power absorbed in a unit length of the material. This can be re-written as:

$$\frac{dI}{dx} = -\alpha \times I(x) \tag{4.1}$$

where x is the direction of propagation of the beam, $I(x)$ is the intensity of light at position x and $\frac{dI}{dx}$ is the change in light intensity. This can be integrated to obtain the Beer-Lambert law:

$$\int_{I_0}^{I} \frac{dI}{I(x)} = -\alpha \int_0^x dx \tag{4.2}$$

$$ln\frac{I}{I_0} = -\alpha x \tag{4.3}$$

$$I = I_0 e^{-\alpha x} \tag{4.4}$$

where I_0 is the optical intensity at $x = 0$. The Beer-Lambert law can be used to obtain the transmittance of a thin film - a quantity used to describe optical properties of

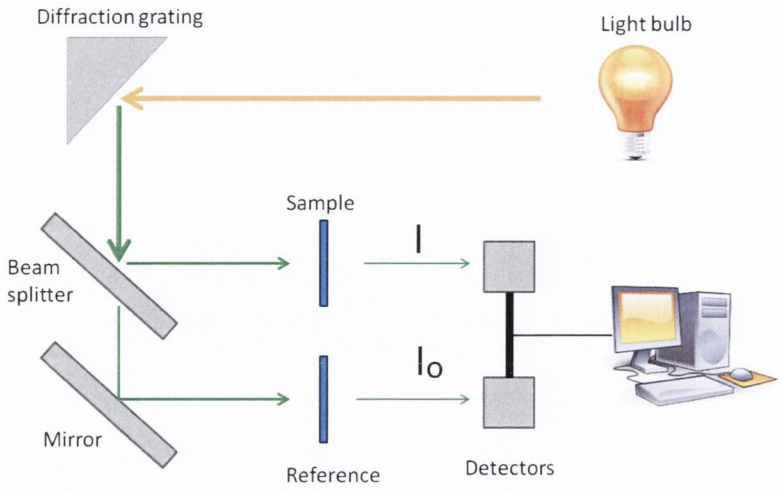

Figure 4.4: Schematics of a spectrophotometer: a beam of white light is split and passed through a sample and a reference cell. The transmitted light intensity is measured for different wavelengths. The wavelength of the incident light can be chosen using a diffraction grating.

transparent electrodes. Transmittance which is the fraction of incident light at a specified wavelength that passes through a sample can be defined as

$$T = \frac{I}{I_0} \tag{4.5}$$

$$= e^{-\alpha x} \tag{4.6}$$

meaning that the intensity of light in the sample decreases by $e^{-\alpha}$ for every unit length travelled by the light through the material. Also, the concentration of a solution containing nanoparticles can be found by using the absorbance of the sample. Absorbance is defined as

$$A = -log\left(\frac{I}{I_0}\right) \tag{4.7}$$

while the concentration is

$$C = \frac{A}{\alpha l} \tag{4.8}$$

where l is the thickness of the sample. Absorption and transmittance spectra were measured using a Varian Cary 6000i spectrophotometer. A schematic of the machine is shown in Figure 4.4. Baseline spectra were taken before all sample scans and each sample was scanned on average 5 times to confirm network uniformity.

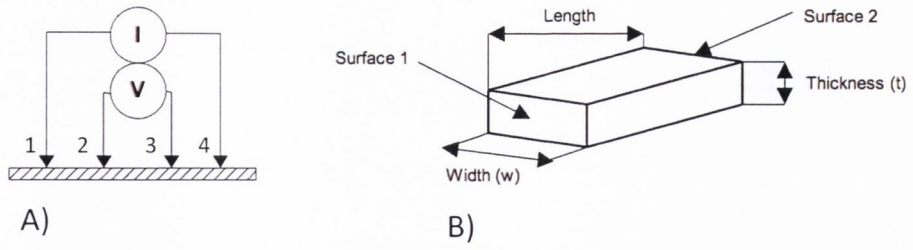

Figure 4.5: A) Setup for four point probe method; 4 strips are painted onto the sample with the outer strips connected to the current and the inner strips connected to the voltage. B) The direction for the length of the sample is parallel to the current.

4.5 FOUR POINT PROBE

Resistivity measurements are important for characterizing the properties of materials and determine their suitability for device application. As a matter of fact, figures of merit for TC applications are directly related to the conductivity of the material (Equations 3.9 and 3.29). However the approach for such measurements must minimize or remove the resistivity input from the contacts. The four point probe method was devised in order to rid the resistivity measurements from any such input. With the 2 point method current and voltage are measured in the same wire and the measured voltage is a result of the sum of the resistances from the sample and the connecting wires. For high resistance ($\geq 1M\Omega$) this method can be used because contact resistances are negligible. For low resistivity measurement this method will not be accurate as the contact resistance will be very close to the resistance of the sample. This is why, for low resistivity, four point probing is advised. The method consists in placing four equidistant, parallel strips of silver paint of identical length onto a flat area of the material to be measured. A current is applied through the outer strips (1 and 4 in Figure 4.5) while the floating potential is measured between the two inner strips (2 and 3 in Figure 4.5). Since no current flows through the inner strips the potential difference measured is only due to the resistance of the sample between the inner strips (2 and 3) [159]. The resistance can then be obtained from Ohm's law $V = RI$ The systems studied all through this thesis are thin films of thickness below a few hundred nanometres and therefore sheet resistance is used in place of resistance to

describe their properties. When the term sheet resistance is used, it is implied that the current flow is along the plane of the sheet, not perpendicular to it. In a regular three-dimensional conductor, the resistance can be written as

$$R = \rho \frac{L}{A} \tag{4.9}$$

where ρ is the resistivity of the material, L is the length of the sample (always parallel to the direction of the current) and $A = W \times t$ is the cross-sectional area of the sample. Then:

$$R = \rho \frac{L}{Wt} = R_S \frac{L}{W} \tag{4.10}$$

where R_S is the sheet resistance in $\Omega/\square$. In fact, R_S has the same dimensions as the resistance but these new dimensions indicate the resistance of a square of the same material. From the definition of resistance we can then write:

$$R_S = (\sigma_{DC,B} t)^{-1} \tag{4.11}$$

For this study a digital mutimeter (Keithley 2400) was connected to four silver electrodes, which were uniformly spaced on the surface of the sample (Figure 4.5), via thin silver wires (diameter = $10\mu m$). The applied current was recorded and the potential response measured using the Labview software.

4.6 SEM

SEM is one of the most widely used techniques in characterising nanomaterials and nanostructures. A coherent, monochromatic stream of electrons is accelerated towards a sample. The stream is then confined and focused into a beam of very fine spot size ($\sim 5nm$) using a series of magnetic lenses and has energy ranging from a few hundred electron volts to $50keV$. The beam then scans across the surface of the specimen with the help of deflection coils. When the electron beam interacts with the sample, the electrons lose energy by repeated scattering and/or absorption within a small volume of the specimen known as the interaction volume. This volume can extend 5μm into the surface depending on the electrons' initial energy, the atomic number of the material and the density of the material. Various detectors are placed within the chamber

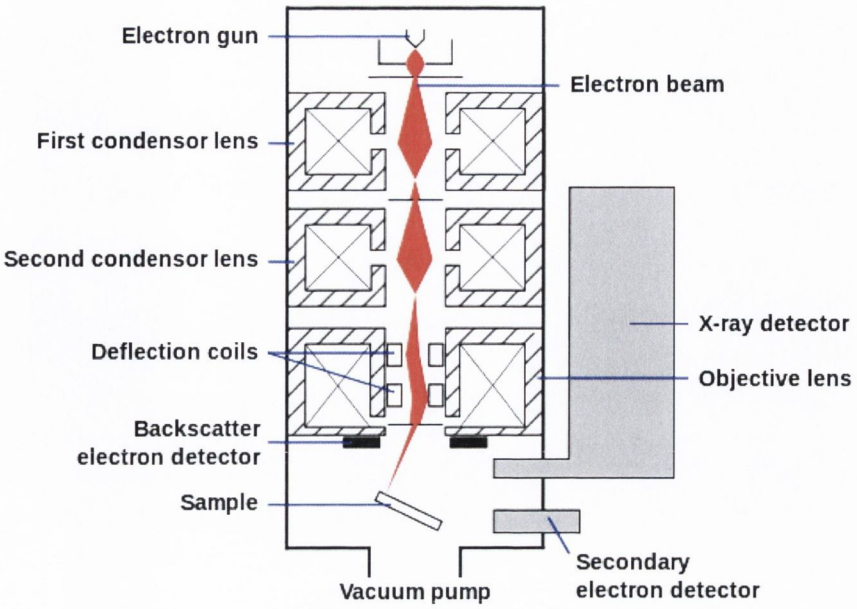

Figure 4.6: Schematics of an SEM: an electron beam is created and confined using magnetic lenses. The accelerated electrons interact with the sample and the energy lost by the back-scattered or secondary electrons can be measured. This information is used to create a picture of the surface of the sample.

to detect elastically back-scattered electrons, inelastically back-scattered electrons (or secondary electrons) and the emission of electromagnetic radiation from the absorption and re-emission of electrons. The resolution of the SEM approaches a few nanometers and the instrument can operate at magnifications that are easily adjusted from *10* to over *300000*. The theoretical limit to an instrument's resolving power is determined by the wavelength of the electron beam used and the specifications of the system [160]. The wavelength is linked to the energy so that best resolutions are obtained for very high energy electrons. The drawbacks of this are that the electron beam might destroy the sample being analyzed and that low conductivity samples will charge causing imaging difficulties. Once the beam has interacted with the sample the collected electrons will have different energies and hence carry information about the topography of the surface of the sample but also about the chemical composition information near the surface[160]. The SEM used in this study was a Zeiss Ultra Plus Field Emission. It allowed us to measure the diameter and length of nanowires, the thickness of bulk networks of nanomaterials and the cross section of some devices.

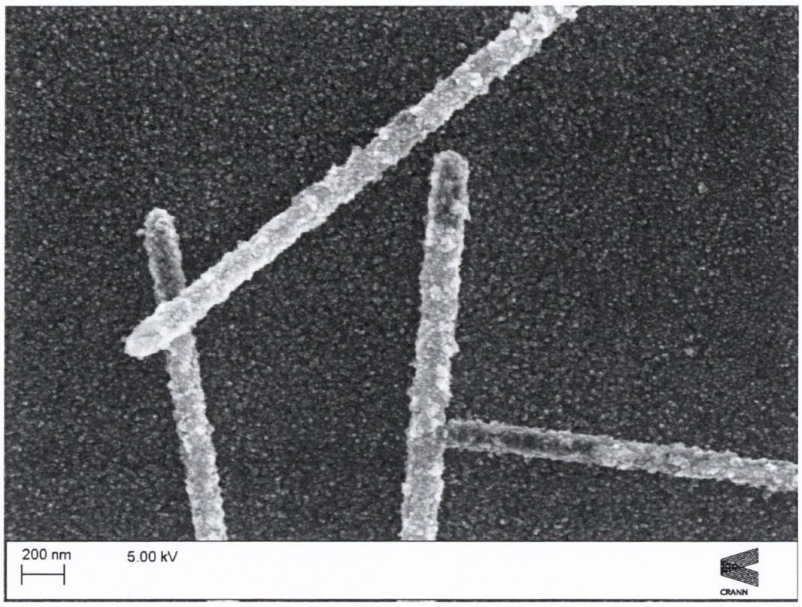

Figure 4.7: Example of an image obtained through SEM of a film of silver nanowires. The nanowires reacted with sulphur compounds in the air and hence are covered in silver sulphide (Ag_2S). [161]

4.7 IMPEDANCE SPECTROSCOPY

Throughout this work, capacitive devices were characterized using impedance spectroscopy. The principle of electrochemical impedance spectroscopy (EIS) is simple, an AC voltage is applied to the sample while the current response is measured as a function of voltage frequency. Background information on EIS is largely covered in Chapter 3 and hence will not be covered here. The spectroscope used in this study was a Gamry 3000, AC voltage applied varied between *25* and *50 mV* at frequencies ranging from *10Hz* to *1MHz*.

4.8 THERMAL MEASUREMENTS OF SILVER NANOWIRE NETWORKS

Measuring the surface temperature of a device can be done in several ways; for example, through infrared measurements of the energy radiating from the sample or through the use of a thermistor as was the case for this study. A thermistor is a type of resistor whose resistance varies significantly with temperature, more so

than in standard resistors. Therefore, as the sample heats up the thermistor heats up along with it and its resistance changes. The resistance of the thermistor can then be measured and linked to the temperature by using the Steinhart–Hart equation, a widely used third-order approximation:

$$\frac{1}{T} = a + bln\,(R) + cln^3\,(R) \tag{4.12}$$

where a, b and c are known parameters, R is the measured resistance and T is the temperature in *Kelvin*. In this work, Kechuang silver nanowires with diameter $D = 25nm$ and $L = 15\mu m$ were sprayed onto a 2 x 2 cm piece of PET with a back-pressure of $45psi$, a flow rate of $2.5mm^3.s^{-1}$ on a hotplate at 120^oC. The PET was then taped onto a glass slide and two silver electrodes were painted at either extremity of the sample. A current was passed through the samples using a Keithley 2400 sourcemeter causing the temperature of the network of silver nanowires to increase through Joule heating. The temperature of the networks could then be measured using a thermistor which had been screwed onto the side of the sample at the halfway point between the electrodes (see Figure 7.4). The resistance changes in the thermistor were measured using a Lakeshore 370AC resistance bridge and the corresponding temperature was calculated using MATLAB. In order to reduce the effects of temperature fluctuations within the laboratory, the sample was enclosed in an insulating box.

5

THE DEPENDENCE OF THE OPTO-ELECTRICAL PROPERTIES OF SILVER NANOWIRE NETWORKS ON NANOWIRE LENGTH AND DIAMETER

5.1 INTRODUCTION

One dimensional nanomaterials are already in use as transparent conductors for device applications. This chapter will deal with studying the properties of networks of silver nanowires as a function of the geometry of the nanowires making up the network. First, the controlled shortening of the nanowires by sonication induced scission will be studied in order to investigate the role played by the length of the nanowires on the opto-electrical properties of the network. Then the influence of the nanowire diameter will be investigated, leading to the use of figures of merit describing the behaviour of both thick nanowire networks and highly transparent networks in the percolation regime. The data will allow us to understand the role of the nanowire diameter on the overall network properties and make assumptions on which nanowire geometry will lead to the best networks for device applications. As an introduction, the advantages and drawbacks of annealing the networks and the effect on their opto-electrical properties will be investigated.

5.2 SAMPLE PREPARATION

For this study, silver nanowires (AgNWs) were synthesized by Seashell Technologies and supplied as suspensions in isopropyl alcohol (IPA) ($C_{AgNW} = 12.5\ mg.ml^{-1}$). A small volume of the dispersion was diluted to $0.001\ mg.ml^{-1}$ with Millipore water. In general, this was subjected to $2\text{-}5\ min$ low power sonication in a sonic bath (Model Ney

Ultrasonic) to eliminate bundles of nanowires. Silver nanowire films were prepared by vacuum filtration of the above dispersions using porous mixed cellulose ester filter membranes (MF-Millipore membrane, mixed cellulose esters, hydrophilic, *0.22 μm*, *47 mm*). The deposited films were dried on a hotplate (50°C) followed by a wet transfer to a polyethylene terephthalate (PET) substrate using heat and pressure as described in Chapter *4.2*. The cellulose filter membrane was then removed by treatment with acetone vapour and subsequent acetone liquid baths followed by a methanol bath; the end film was *36 mm* in diameter.

5.3 ANNEALING OF THE NETWORKS

As seen in Chapter *2*, many groups have reported an amelioration of the opto-electrical properties of nanowire networks after annealing, however this amelioration was not quantified. With this in mind, networks of silver nanowires with different lengths and diameters but the same film thickness were made and transferred onto a glass substrate. The thickness was chosen to be such that the networks would display bulk behaviour, i.e. $t \gg 100nm$. They were then annealed in an oven with a nitrogen atmosphere at *200°C* for *30 min*, the time and temperature were chosen to match that found in the literature. Sheet resistance and transmittance were measured before and after anneal as shown on Figure 5.1, A). This graph displays a clear shift of the data upwards and left which indicates that the sheet resistance of the network has decreased and that the network has become more transparent. These changes can be explained by the removal of polymer leftover from the synthesis of the nanowires. For each nanowire type, the conductivity ratio for the network was calculated before and after anneal using equation 3.9

$$T = \left(1 + \frac{Z_0}{2R_S}\frac{\sigma_{op}}{\sigma_{DC,B}}\right)^{-2}$$

It is clear from Figure 5.1, B) that annealing the networks has the effect of increasing the conductivity ratio. Knowing that there was both an increase in the transmittance and a decrease in the sheet resistance suggests that annealing has the double effect of increasing the dc conductivity and decreasing the optical conductivity. In the case

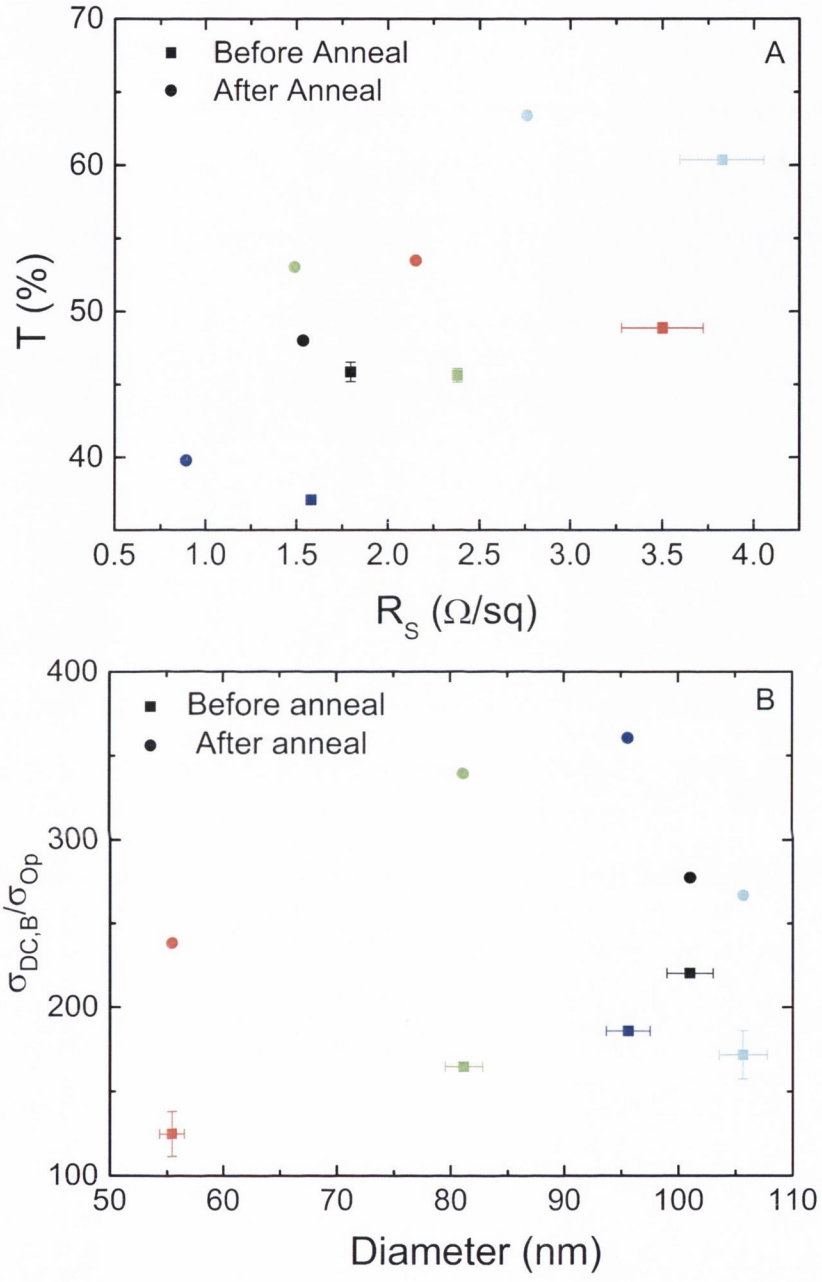

Figure 5.1: Annealing of thick nanowire networks at 200°C for 30 minutes where each colour describes a set of nanowires with a different aspect ratio: A) Transmittance and sheet resistance before and after anneal; the left-shift shows an increase in $\sigma_{DC,B}$ while the upwards-shift shows a decrease in optical conductivity B) Conductivity ratio before and after anneal, the increase can be explained by the removal of residual polymer from nanowire synthesis.

of $\sigma_{DC,B}$, annealing could be responsible for both removing the polymer from the junctions and welding the nanowires together. This would dramatically decrease the junction resistivity and also increase overall network conductance. To a lesser extent, removing the polymer from the network would mean light would not be scattered as much, lowering the optical conductivity of the network and hence increasing the overall transmittance of the thin film (see Chapter 3, equation 3.8).

5.4 DEPENDENCE OF NETWORK PROPERTIES ON NANOWIRE LENGTH

5.4.1 *Sonication induced scission*

In order to study the effects of nanowire geometry on the network, it is important to control the geometry of those nanowires. Furthermore, it is critical to separate the influence that the length and diameter of the nanowires have on the dc and optical conductivities of the network. As discussed in Chapter 2, the diameter of the nanowires is controlled for the most part by the diameter of the initial seed at the time of formation, therefore the only geometric parameter that can be controlled is the length of the nanowire. In this regard, a dispersion of nanowires with initial length $6\mu m$ was sonicated in a sonic bath for *90 min*. Every few minutes, a couple of drops of the dispersion was removed in order to be analyzed. This solution was dropped onto gold coated silicon for SEM measurements of the length of the nanowires. Images taken by SEM were analyzed using the program ImageJ as shown in Figure 5.2. The results of this analysis are shown in Figure 5.3 including the length distribution of the nanowires after scission. It is clear from the data that the length of the nanowires follows a power law: $L \propto t^{-0.33}$. This exponent is reasonably close to the value of *-0.5* expected from sonication induced scission[52–54]. This discrepancy could be due to the fact that previous work on sonication induced scission was done in the presence of a surfactant which would have an effect on the size of the bubbles, cavitation velocity and amplitude of the strain on the nanoparticles. Furthermore it was done in the presence of carbon nanotubes which have a different structure and tensile strength

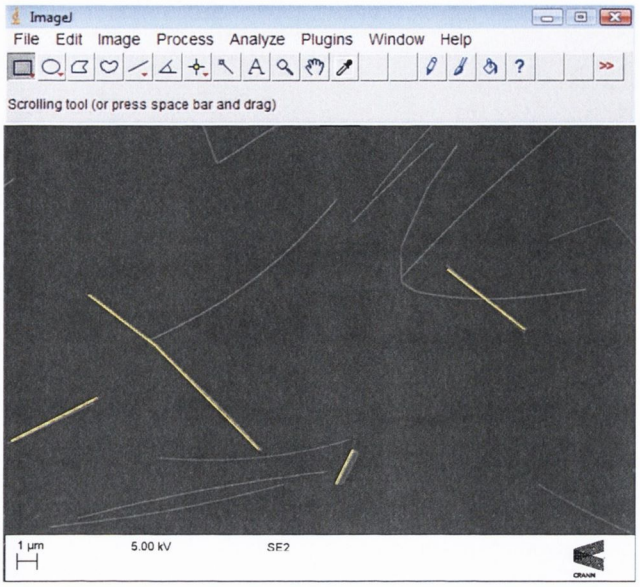

Figure 5.2: The program ImageJ was used to measure length and diameter of the nanowires. SEM images were taken of each samples and the length and diameters of a number of nanowires were measured, those measurements were then statistically analysed as shown in Figure 5.3.

compared to silver nanowires. However, this study demonstrates that the length of the nanowires can be controlled, making it possible to investigate the dependence of the properties of the network using nanowires which have been shortened to different lengths.

5.4.2 *Dependence of $\sigma_{DC,B}$ and σ_{Op} on length*

With studying the effects of nanowire length on the properties of the network in mind, both a thick film (2–3 μm) and a thin film (*200–300 nm*) were prepared for different sonication time by vacuum filtration. The thicknesses of these films were estimated by breaking the films and imaging the cross section via SEM (Figure 5.4). It must be noted that this method, like all methods of thickness measurements for nanostructured thin films, is somewhat unreliable and presents an error of up to *30%*. However, in this experiment the variation in conductivity over the range of nanowire lengths was large enough that the thickness-related error in conductivity was acceptable. For the

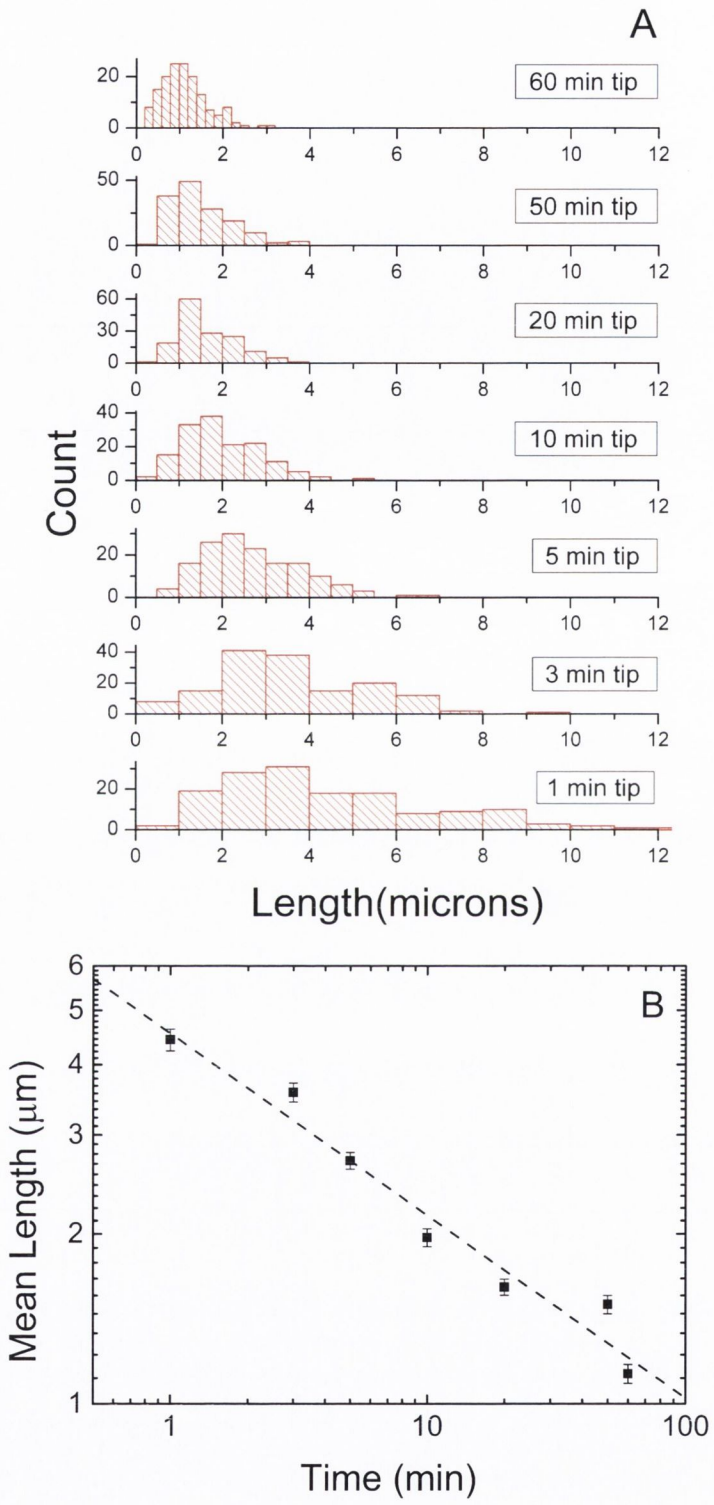

Figure 5.3: Sonication induced scission: A) Distribution of the length of the nanowires at different time intervals B) Plotting the average nanowire length against the sonication time shows a relationship of the type $L \propto t^{-0.33}$.

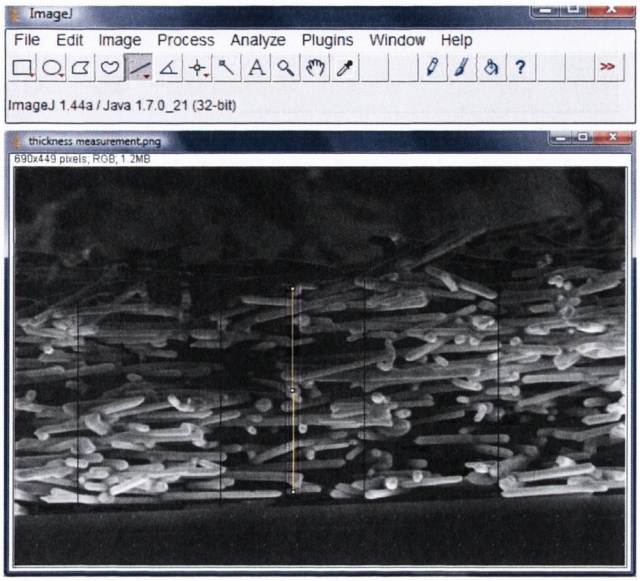

Figure 5.4: Measuring the network thickness using the ImageJ program. A thick film is produced and transferred onto a silicone substrate, the silicone is then snapped in half and the cross section of the film is imaged under SEM. High surface roughness and difficulty to align the sample perpendicularly to the line of sight leads to a measurement error of up to 30%.

thick films which were many times thicker than the nanowire diameter and hence displayed bulk-like properties, the sheet resistance and thickness were measured and $\sigma_{DC,B}$ calculated using

$$R_S = (\sigma_{DC,B} t)^{-1} \tag{5.1}$$

For the thin films, the optical transmittance was measured (at $550\ nm$) and the thickness estimated in order to calculate σ_{Op} using

$$T = \left(1 + \frac{Z_0}{2}\sigma_{Op} t\right)^{-2} \tag{5.2}$$

Figure 5.5 shows $\sigma_{DC,B}$ and σ_{Op}as a function of nanowire length with scatter attributed in both cases to the difficulties in measuring film thickness, t.

Clearly, $\sigma_{DC,B}$ exhibits a linear dependence on the length of the nanowires . This is not surprising as longer nanowires are more likely to connect with other nanowires, increasing the connectivity of the network and hence increasing the probability the network will be conductive [114]. In fact, simulations on networks of conducting sticks have shown that the conductivity should scale with nanowire length as a power

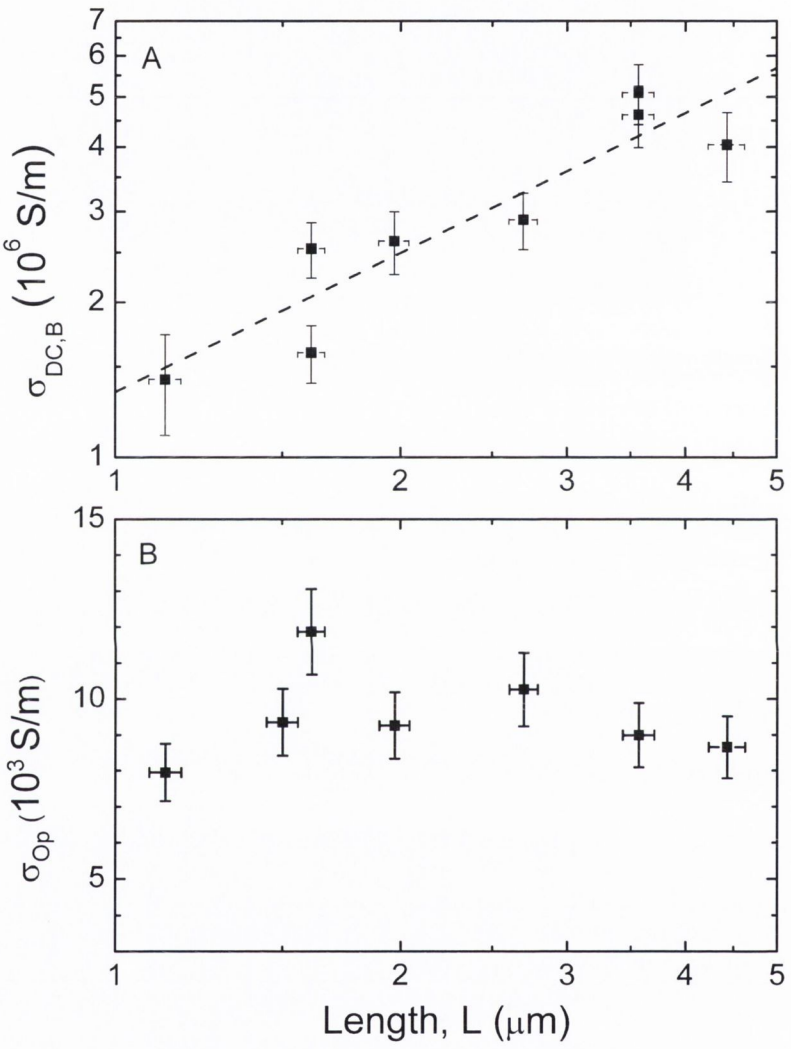

Figure 5.5: $\sigma_{DC,B}$ and σ_{Op} against the length of the nanowires making up the network. A) The dc conductivity displays a linear relationship as a function of length while B) the optical conductivity seems to be independent of nanowire length.

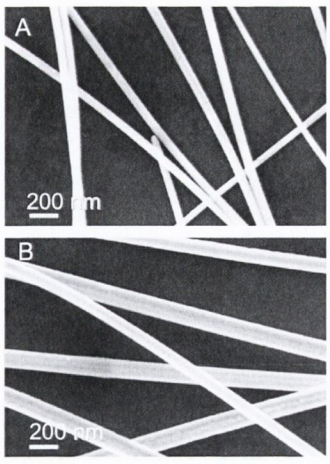

Figure 5.6: SEM of silver nanowire with A) small diameter as opposed to B) large diameter.

law $\sigma_{DC,B} \propto L^{\alpha}$ with exponent in the range $0 \leq \alpha \leq 2.48$ where *zero* means junction resistance is negligible and *2.48* means junction resistance dominates the network resistance[74, 114]. Indeed, by studying networks of carbon nanotubes, Hecht found $\alpha = 1.46$[114]. It is clear from figure 5.5 that a power law is appropriate for our data but with exponent $\alpha = 0.9 \pm 0.2$. The discrepancy with theory could come from the fact that the networks in this study exhibited bulk-like behavior while the theoretical studies were made using percolative networks. This should not cause problems since the conclusions drawn from this study will only affect bulk-like network properties. For the rest of this work a linear relationship: $\sigma_{DC,B} \propto L$ will be assumed and the length of the nanowires will be rescaled to remove the influence of the length on $\sigma_{DC,B}$. In the case of thin films, the data shown in Figure 5.5, B) strongly suggests that σ_{Op} is independent of the length of the nanowires.

5.5 DEPENDENCE OF NETWORK PROPERTIES ON NANOWIRE DIAMETER

Now the effects of the length on $\sigma_{DC,B}$ and σ_{Op} have been understood, it is necessary to investigate the effects of the diameter on the properties of the nanowire network. In order to do this, four types of nanowires with different lengths and diameters were purchased ($61\ nm \leq D \leq 127\ nm$ as measured, in table 5.1, Figure 5.6). For each type of nanowire, a set of films with thicknesses ranging from a few nanometers

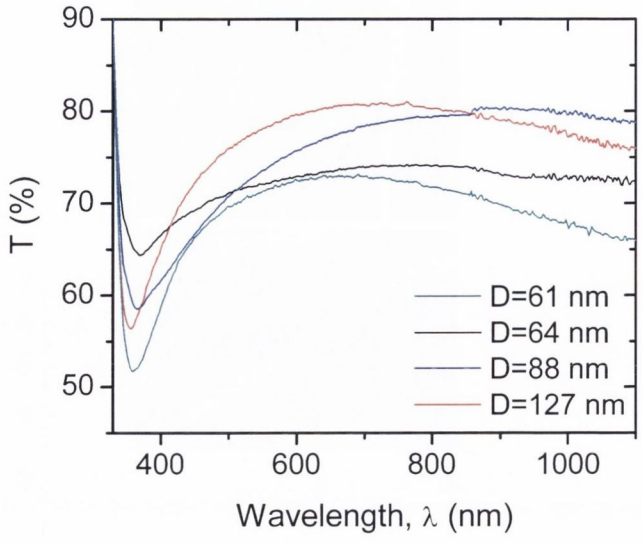

Figure 5.7: Transmittance spectra for thin films for four types of nanowires with different diameters. The spectra are relatively flat over the visible range $390nm \leq \lambda \leq 700nm$.

to a few microns were made and the sheet resistance and transmittance (at $550\ nm$) were measured for each film. Note that the thickness used in this study is the mean thickness for a continuous film with density equal to that of the network, therefore, some values for the thickness obtained are lower than the diameter of the nanowires for percolative networks. The actual thickness of the films could not be formally measured using the SEM method because in the percolation region the surface roughness of the films is as large as the film thickness itself. The transmittance spectra are shown in Figure 5.7 for thin films of same thickness with nanowires of different diameters. A typical example of the transmittance at 550 nm and sheet resistance data for a range of nanowire networks with a given D and L was plotted in figure 5.8 displaying an increase in sheet resistance as the transmittance increases.

The aim of novel transparent conductors is to obtain the highest possible transmittance paired with very low sheet resistance. It is therefore necessary to fit the data to a model in order to extract information that will allow us to investigate the suitability of nanowires for applications compared to other transparent conductors. It is believed that nanowire networks display thickness independent (i.e. bulk-like) dc conductivities above a certain thickness t_{min}. Below t_{min}, thin films are controlled by percolation and

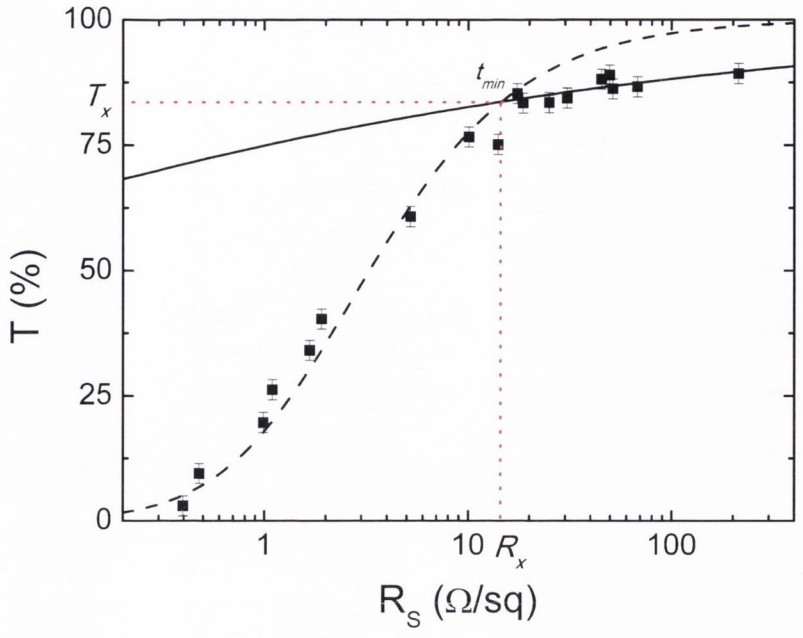

Figure 5.8: An example of the T versus R_S curves representative of transparent networks of low-dimension nanomaterials.The network enters the percolation regime at thickness t_{min}. At this thickness the network exhibits a transmittance T_x and sheet resistance R_x.

the percolation exponent n and have DC conductivity which is dependent on film thickness. As discussed in Chapter 3, the transmittance is defined as

$$T = \left[1 + \frac{Z_0}{2R_S}\left(\frac{\sigma_{Op}}{\sigma_{DC,B}}\right)\right]^{-2} \tag{5.3}$$

for bulk networks (i.e. thick films, dashed line in Figure 5.10) and as

$$T = \left[1 + \frac{1}{\Pi}\left(\frac{Z_0}{R_S}\right)^{1/n+1}\right]^{-2} \tag{5.4}$$

where

$$\Pi = 2\left[\frac{\sigma_{DC,B}/\sigma_{Op}}{\left(Z_0 t_{min}\sigma_{Op}\right)^n}\right]^{1/n+1} \tag{5.5}$$

for percolative networks (i.e. thin films, full lines in Figure 5.10). In order to extract the values for the figures of merit $\frac{\sigma_{DC,B}}{\sigma_{Op}}$, n and Π from the data, equations 5.3 and 5.4 must be rearranged. For the percolative part of the network, equation 5.3 can be rearranged as

$$T^{-0.5} - 1 = \frac{Z_0}{R_S}\frac{\sigma_{Op}}{2\sigma_{DC,B}} \tag{5.6}$$

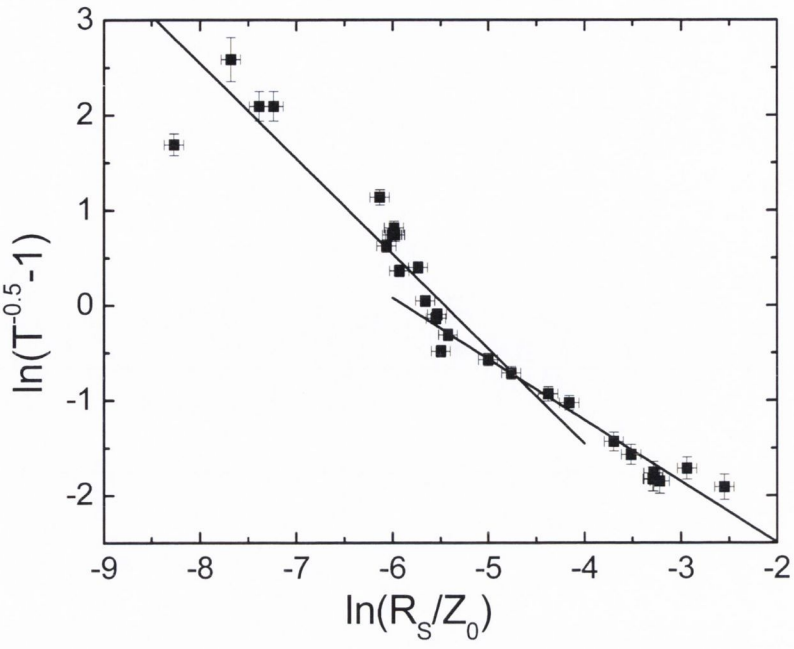

Figure 5.9: Fitting data in order to obtain bulk and percolative figures of merit from the slope and intercept in both regimes using equations 5.8, 5.11 and 5.12 .

$$ln(T^{-0.5}-1) = -ln\left(\frac{R_S}{Z_0}\right) - ln\left(\frac{\sigma_{Op}}{2\sigma_{DC,B}}\right) \tag{5.7}$$

This means that by plotting $ln\left(T^{-0.5}-1\right)$ against $ln\left(\frac{R_S}{Z_0}\right)$ and setting the slope to -1, then

$$\frac{\sigma_{DC,B}}{\sigma_{Op}} = 0.5exp\left(-intercept\right) \tag{5.8}$$

Identically, equation 5.4 can be rearranged

$$T^{-0.5}-1 = \frac{1}{\Pi}\left(\frac{Z_0}{R_S}\right)^{1/n+1} \tag{5.9}$$

$$ln\left(T^{-0.5}-1\right) = -ln\left(\Pi\right) - \frac{1}{n+1}ln\left(\frac{R_S}{Z_0}\right) \tag{5.10}$$

This means that by plotting $ln\left(T^{-0.5}-1\right)$ against $ln\left(\frac{R_S}{Z_0}\right)$ and fitting the data linearly, it follows that

$$n = -1 - \frac{1}{slope} \tag{5.11}$$

and

$$\Pi = exp\left(-intercept\right) \tag{5.12}$$

An example of the fitting is shown in Figure 5.9 The data is very well described by equations 5.3 and 5.4 which in both cases allow us to obtain the values for $\sigma_{DC,B}/\sigma_{Op}$ for

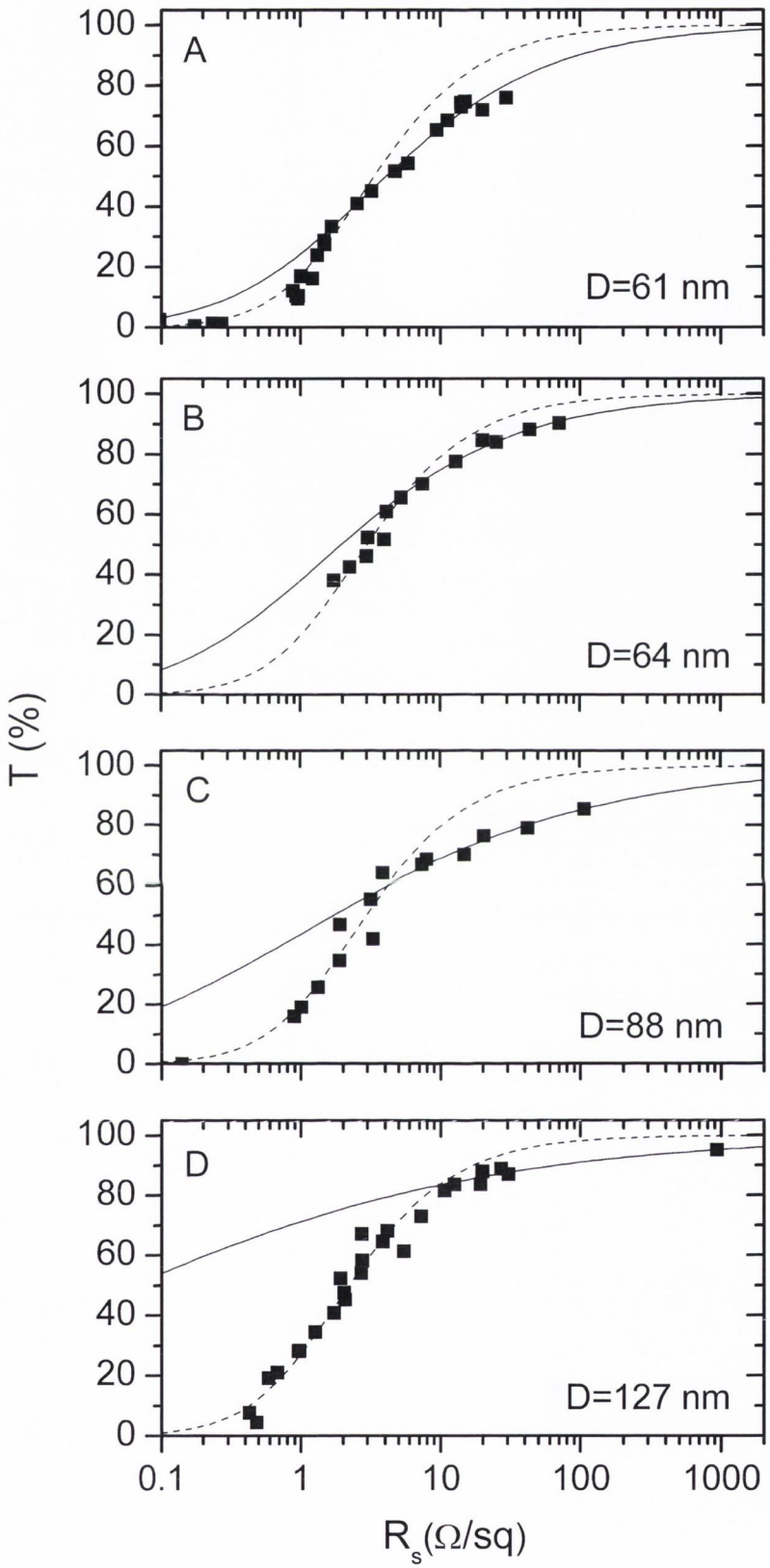

Figure 5.10: Data for the transmittance as a function of sheet resistance for the four nanowire types used in this study. In each case, the data can be divided into two regimes, the bulk-like regime and the percolative regime. These regimes have been fitted using equation 5.3 (dashed line) and equation 5.4 (solid line) respectively.

D (nm)	L (μm)	$\sigma_{DC,B}/\sigma_{Op}$	T_x(%)	Π	n
61	4.0	140	37	42	0.59
64	3.4	151	67	56	0.67
88	4.4	153	61	20	1.53
127	8.7	205	83	30	2.44

Table 5.1: Measured Parameters for each wire type. Note that the values of $\sigma_{DC,B}/\sigma_{Op}$ are as-measured and not rescaled to represent the case when $L = 5\mu m$

bulk networks and Π and n for percolative networks for different types of nanowires. Another parameter describing the networks, $\sigma_{Op}t_{min}$, can also be obtained from the data and will be discussed subsequently. These values are listed in the table in Figure 5.1 with $T_x$used as a proxy for $\sigma_{Op}t_{min}$.

Conductivity ratios for the different nanowires range from *140* to *205* in accordance with recent work undertaken on silver nanowires as transparent conductors [32]. However, it was previously shown that $\sigma_{DC,B}$ scales linearly with L. The properties of different nanowires cannot be compared without rescaling the length of each type of nanowires. The rescaled length was chosen to be $L = 5\mu m$ and the rescaled $\frac{\sigma_{DC,B}}{\sigma_{Op}}$ as a function of D data is shown in Figure 5.11 (the conductivity ratio was rescaled by multiplying it by $\frac{L}{5}$). These data can be fit to a power law $\sigma_{DC,B}/\sigma_{Op} \propto D^{-\beta}$ with $\beta = 0.79 \pm 0.2$ (exact fit in legend, Figure 5.11). This rather low value of β compared to the expected value $\beta \sim 2-3$ [79, 114, 115] implies that the opto-electrical properties of nanowire networks vary rather slowly with D. This suggests that either the predicted dependence of $\sigma_{DC,B}$ on D is wrong or that σ_{Op}also scales with D. In either case, combining this result with the opto-electronic dependence on L allows us to write

$$\frac{\sigma_{DC,B}}{\sigma_{Op}} \propto \frac{L}{D} \tag{5.13}$$

Understanding the reason behind this slow change is made difficult by the difficulty in accurately measuring film thickness which prevents an independent study of $\sigma_{DC,B}$ and σ_{Op}using equations 5.1 and 5.2. Indeed, the range of wire diameters is too small and so variations in $\sigma_{DC,B}$ and σ_{Op} with diameter are unlikely to overcome errors

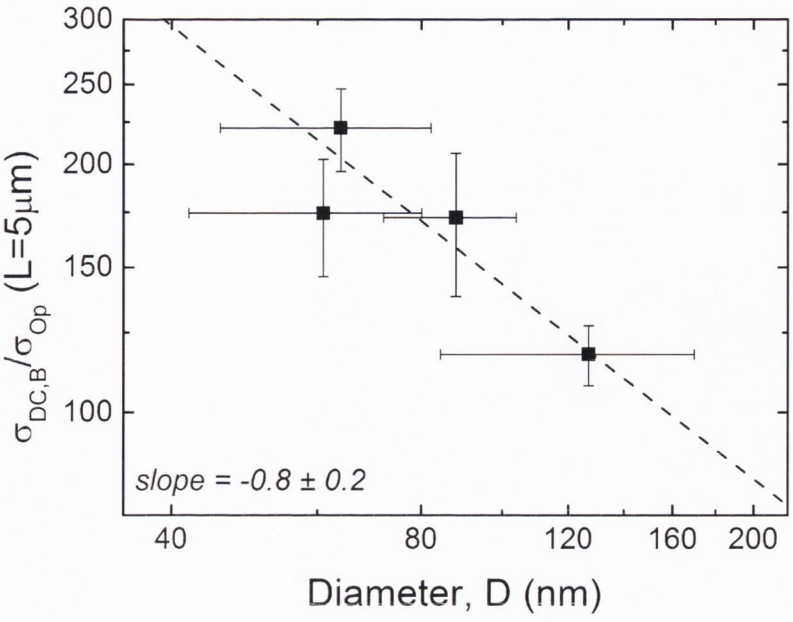

Figure 5.11: The ratio of dc to optical conductivity as a function of nanowire diameter. It was shown in figure 5.5 that the dc conductivity scaled linearly with L, therefore in this study, all nanowires were rescaled to $L = 5\mu m$. The dashed line is a power law fit to the data $\frac{\sigma_{DC,B}}{\sigma_{Op}} = 4.27 \times 10^{-4} D^{-0.79}$ (SI units).

associated with measuring the film thickness. In fact it was found during this work that the errors associated with film thickness measurements were so large as to make any comparative analysis of $\sigma_{DC,B}$ and σ_{Op} completely unreliable. However, as shown by equations 5.3, 5.4 and 5.5 it is not necessary to know individual values for $\sigma_{DC,B}$ and σ_{Op}since it is possible to describe the system fully, knowing $\sigma_{DC,B}/\sigma_{Op}$, n and $\sigma_{Op}t_{\min}$. $\sigma_{DC,B}/\sigma_{Op}$and n can be found by fitting equations 5.3 and 5.4 respectively to the data, however $\sigma_{Op}t_{\min}$is not as straightforward to obtain. $t_{\min}$ is the transition thickness from bulk to percolative network, therefore $\sigma_{Op}t_{\min}$can be found by assuming a film of thickness $t_{\min}$ has transmittance $T_x$at the point of intersection of the two curves generated by equations 5.3 and 5.4. Equation 5.2

$$T_x = \left(1 + \frac{Z_0}{2}\sigma_{Op} t_{min}\right)^{-2}$$

can be rearranged as

$$\sigma_{Op} t_{min} = \frac{2}{Z_0}\left(T_x^{-0.5} - 1\right) \tag{5.14}$$

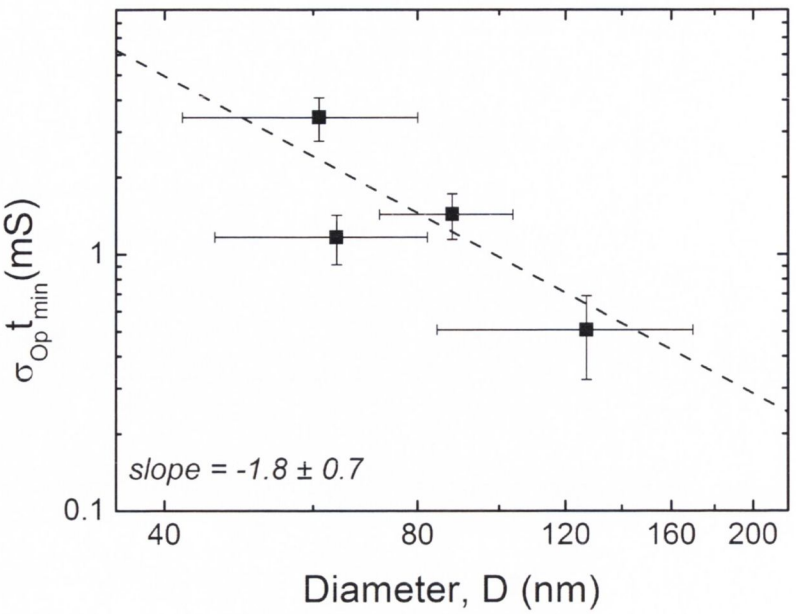

Figure 5.12: Proxy for optical conductivity as a function of mean nanowire diameter. The dashed line is a power law fit to the data; $\sigma_{Op} t_{min} = 3.98 \times 10^{-16} D^{-1.77}$ (SI units).

As T_x is easily obtained from the graphs it is straightforward to obtain $\sigma_{Op} t_{\min}$ and the data is shown in Figure 5.12 as a function of nanowire diameter. It is clear from the graph that $\sigma_{Op} t_{\min}$ scales with D (exact fit in Figure 5.12 legend) however, De et al.[79] have shown that $t_{\min}$is also a function of the nanomaterial diameter for different materials therefore it is not possible to conclude as to what is responsible for this dependence. $\sigma_{Op} t_{min}$ will be used below as a way to characterise thin, industry relevant films.

5.6 DEPENDENCE OF PERCOLATION PARAMETERS ON NANOWIRE DIAMETER

5.6.1 *Extracting* n *and* Π

The low thickness (high T and high R_s) portions of the curves in Figure 5.10 were fitted using percolation theory as described by equation 5.4 and from these fits the percolation exponent, n, and the percolative figure of merit, Π, were obtained for each wire type. These are plotted as a function of wire diameter in figure 5.13. Figure 5.13, A) shows that the percolation exponent increases with increasing diameter from ~ 0.6 to

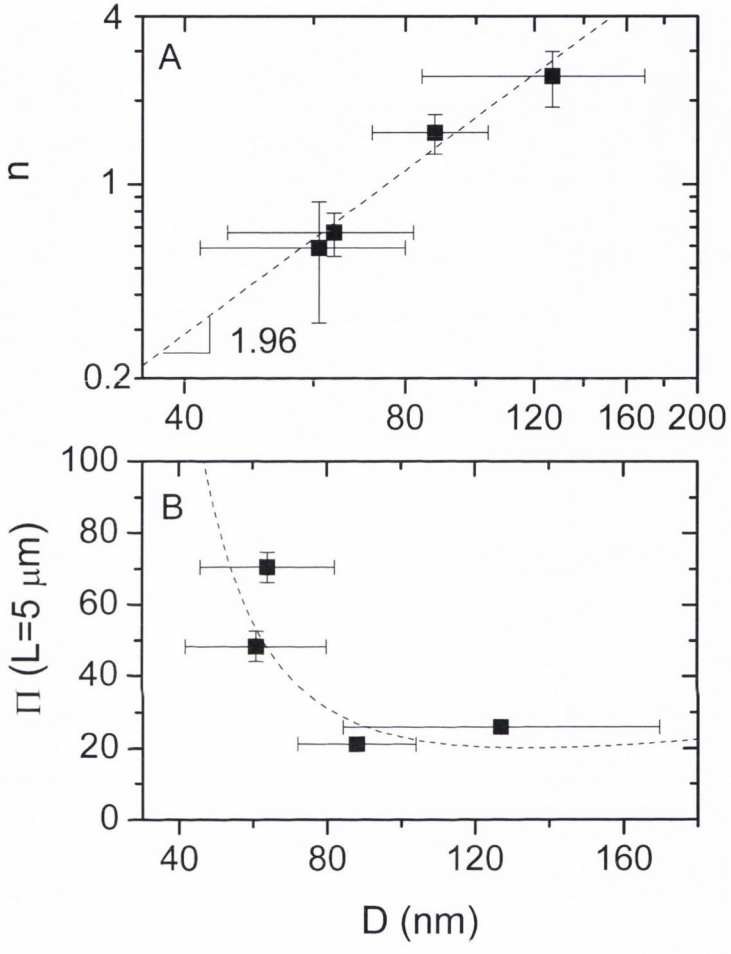

Figure 5.13: Percolation fit constants as a function of mean wire diameter, D. A) The percolation exponent, n, and (B) the percolative figure of merit, Π. In A), the data has been fitted to an empirical power law; $n = 9.12 \times 10^{13} D^{1.96}$ (SI units). In B), the data has been rescaled to represent the values expected for samples of wires with the same mean length of 5 μm. The dashed line in B) represents a continuous function calculated using equation 5.5 incorporating the empirical fit curves shown in figures 5.11, 5.12 and 5.13 A).

~ 3.5. Empirically the data appears to fit very closely to a quadratic dependence (exact fit in legend). For a two-dimensional network, the theoretical value for n is 1.33 [61, 83], however it is well known that the percolation exponent can deviate from its universal value in the presence of a distribution of inter-wire junction resistances, with the magnitude of the deviation scaling with the details of the distribution[80, 81, 84, 85]. It is likely that a disordered network will have a broad distribution of junction resistances and so larger n. Indeed, such a relationship has recently been observed for spray cast AgNW networks where n was observed to scale linearly with the network non-uniformity [33]. In light of this, this data suggests that the network non-uniformity tends to increase with increasing wire diameter. This clearly suggests that for networks in the percolative regime, low diameters are advantageous because low values of n lead to more uniform networks. It must be noted that following from equation 5.4, lower values of n lead to lower R_s , coupled with higher T i.e. better opto-electrical properties. Again this suggests that low D wires are desirable.

The percolation fits also give values for Π as shown in Table 5.1where the values must be corrected for the varying length as previously stated. This was done by multiplying the original values of Π by $\left(\frac{5\mu m}{L}\right)^{1/n+1}$. The rescaled data is shown in Figure 5.13, B) as a function of D. Here Π increases sharply as D decreases, reaching 70 for $D = 60\ nm$. That higher values of Π lead to lower R_s, coupled with higher T, again suggesting that low D wires give better opto-electrical properties. We note that values of Π approaching 70 are extremely high. Recently, De et al. analyzed the literature[79] for networks of metallic nanowires using equation 5.4(Figure). The highest value of Π found was 48 for networks of copper nanowires [34]. As described above, Π is a composite parameter defined by equation 5.5. The more fundamental parameters controlling Π are $\sigma_{DC,B}/\sigma_{Op}$, $\sigma_{Op}t_{\min}$ and n. However, for each of these parameters empirical expressions were generated by fitting the data in figures 5.11, 5.12 and 5.13, A).The generated expressions were

$$n = 9.12 \times 10^{13} D^{1.96} \tag{5.15}$$

$$\sigma_{Op} t_{min} = 3.98 \times 10^{-16} D^{-1.77} \tag{5.16}$$

$$\frac{\sigma_{DC,B}}{\sigma_{Op}} = 4.27 \times 10^{-4} D^{-0.79} \tag{5.17}$$

	$\sigma_{DC,B}/\sigma_{Op}$	Π	n	comment
carbon-based films				
Green *et al.*[11]	no data	3.3	0.75	unsorted SWNTs
Green *et al.*[11]	4.8	9.4	0.65	sorted SWNTs (M)
Green *et al.*[11]	3.5	8.7	0.91	sorted SWNTs (M)
Pei *et al.*[14]	no data	13.1	1.04	SWNTs
Chandra *et al.*[10]	8.5	12.3	0.50	pristine SWNTs
Chandra *et al.*[10]	19.5	23.8	0.36	doped SWNTs
Li *et al.*[12]	2.4	4.7	0.64	pristine SWNTs
Li *et al.*[12]	11.0	9.1	1.60	doped SWNTs
Manivannan *et al.*[13]	3.8	9.6	0.82	SWNTs
Unalan *et al.*[17]	no data	2.6	1.49	SWNTs
Parekh *et al.*[16]	1.2	no data	no data	SWNTs
Parekh et al.[16]	5.1	no data	no data	doped SWNTs
Dan *et al.*[4]	4.5	no data	no data	SWNTs
Dan *et al.*[4]	11.3	no data	no data	doped SWNTs
Wu *et al.*[22]	1.7	4.7	0.51	reduced graphene oxide
metallic films				
Rathmell et al.[20]	no data	6.2	6.50	CuNWs deposited
Wu *et al.*[21]	106	48	0.83	CuNWs fused
O'Connor *et al.*[39]	72	4.7	5.3	thin Ag film

Figure 5.14: Values of $\sigma_{DC,B}/\sigma_{Op}$, Π and n found by De et al. from fitting the data from the literature with equations 5.3 and 5.4.[79]

These expressions can be substituted into equation 5.5 to give a semi-empirical expression for Π as a function of D

$$\Pi = 2\left[\frac{4.27\times10^{-4}D^{-0.79}}{\left(1.5\times10^{-13}D^{-1.77}\right)^{9.12\times10^{13}D^{1.96}}}\right]^{1/\left(1+9.12\times10^{13}D^{1.96}\right)} \tag{5.18}$$

This is shown in figure 5.13, B) as the dashed line and clearly shows the rapid increase in Π for $D < 80\ nm$.

5.6.2 *Resistance for 90% transmittance*

The data described above shows that lower values of D give better values of n and Π, with respect to opto-electrical applications. However, having two parameters describing the performance is not ideal. A single figure of merit which could directly be linked to performance would be much more desirable. We note that for industrial applications the transmittance generally needs to be above 90% while the sheet resistance must be as low as possible. With this in mind, a useful parameter is the sheet resistance of a film with $T = 90\%$, $R_S^{T=90\%}$. As networks with $T = 90\%$ generally reside in the percolative

regime, this new parameter can be found by setting $T = 90\%$ and rearranging equation 5.4:

$$0.054 = \frac{1}{\Pi}\left(\frac{Z_0}{R_S^{T=90\%}}\right)^{1/n+1} \tag{5.19}$$

where 0.054 arises from setting $T = 90\%$ and subbing into $\left(T^{-0.5} - 1\right)$, then:

$$R_S^{T=90\%} = Z_0\left(0.054\Pi\right)^{-(n+1)} \tag{5.20}$$

Alternatively, $R_S^{T=90\%}$ can be written in terms of more fundamental quantities by combining equations 5.4 and 5.5 and again setting $T = 90\%$

$$T = \left[1 + \frac{1}{2}\left[\frac{\left(Z_0\sigma_{Op}t_{min}\right)^n}{\sigma_{DC,B}/\sigma_{Op}}\right]^{1/n+1}\left(\frac{Z_0}{R_s}\right)^{1/n+1}\right]^{-2} \tag{5.21}$$

$$2\left(\frac{1}{\sqrt{T}} - 1\right)^{n+1} = \frac{Z_0}{R_s}\frac{\sigma_{Op}}{\sigma_{DC,B}}\left(Z_0\sigma_{Op}t_{min}\right)^n \tag{5.22}$$

$$2\left(0.054\right)^{n+1} \approx \frac{Z_0}{R_s^{T=90\%}}\frac{\sigma_{Op}}{\sigma_{DC,B}}\left(Z_0\sigma_{Op}t_{min}\right)^n \tag{5.23}$$

$$R_S^{T=90\%} = \frac{Z_0}{0.11^{\sigma_{DC,B}/\sigma_{Op}}}\left(\frac{Z_0\sigma_{Op}t_{min}}{0.54}\right)^n \tag{5.24}$$

This expression displays an exponential relationship between $R_S^{T=90\%}$ and n, underlining the importance of n i.e. network uniformity. Both these expressions were used to calculate $R_S^{T=90\%}$ using the data described above for each wire type (Figure 5.15). Although there is some scatter and considerable uncertainty, these data clearly show that lower diameter wires give better values of $R_S^{T=90\%}$. To make the diameter dependence clearer, a semi-empirical expression for $R_S^{T=90\%}$ as a function of D was generated using the empirical expressions for $\sigma_{DC,B}/\sigma_{Op}$, n and $\sigma_{Op}t_{\text{min}}$ described above, similarly to what was done with equation 5.18. This is shown as the solid line in Figure 5.15. These data clearly show that very low values of $R_S^{T=90\%}$ can be expected if wires with very low D can be produced. Although it must be noted that for lower diameters, electrons will start to feel the effects of confinement and increased scatter will start to play a part in the dc conductivity. In fact, measurements have shown the nanowire conductivity to fall by a factor of two as D is reduced from $50\ nm$ to $25\ nm$[162, 163]. Figure 5.15 also indicates that larger nanowires would improve the opto-electrical properties of the network, however it is believed that larger nanowires would lead to increased

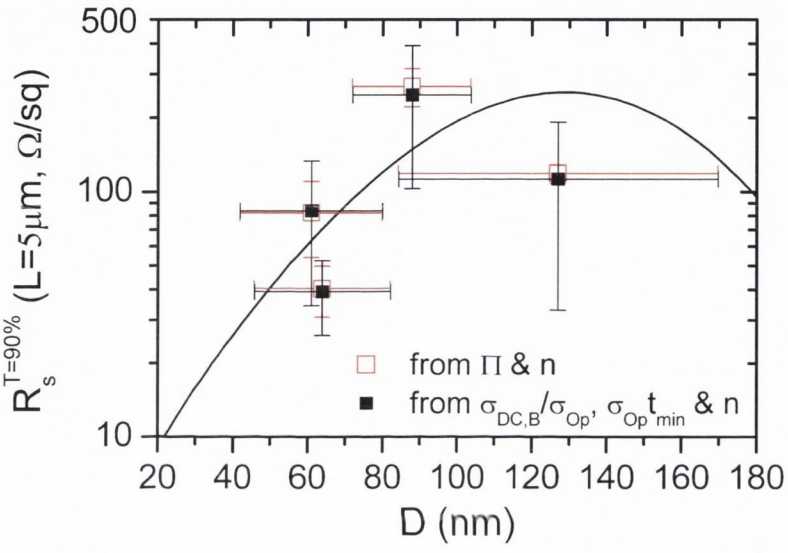

Figure 5.15: The estimated sheet resistance associated with a film of transmittance of 90%, $R_S^{T=90\%}$, plotted as a function of mean wire diameter. The data points represent $R_S^{T=90\%}$ calculated two ways: using values of Π and n found for each wire type using equation 5.20 and using values of $\frac{\sigma_{DC,B}}{\sigma_{Op}}$, $\sigma_{Op}t_{min}$ and n using equation 5.24 (in each case the values used were those rescaled to represent samples of $5\mu m$ long nanowires). The solid line represents a continuous function calculated using equation 5.24 incorporating the empirical fit curves shown in figures 5.11, 5.12 and 5.13, A).

haze[30, 33] due to an increase of the optical conductivity from increased scattering of light and would also diminish the uniformity of the network and hence lower n.

5.7 CONCLUSION

The aim of this work was to understand the reasons behind the broad variation in the opto-electrical properties of silver nanowire thin films. Preliminary work on silver nanowires showed that annealing thick networks for a short period of time enhances their opto-electrical properties which is believed to be due to the removal of leftover polymer from synthesis and welding of the nanowires at the junctions.

In order to investigate the role played by nanowire length on network properties, nanowires with initial length $L = 4.5\mu m$ were shortened to about $1\mu m$ using sonic energy. It was shown that the length of the wires followed a power law with respect to sonication time of the form $L \propto t^{-0.33}$. A similar time dependence was found by Hecht[114] for work on carbon nanotubes. This shows that sonication induced scission will be a powerful tool for tuning nanowires to industry specified requirements.

A range of networks of silver nanowires with different lengths (L) and diameters (D) were then produced and their transmittance and sheet resistance measured. It was found that while the bulk-like dc conductivity, $\sigma_{DC,B}$, of the networks scales linearly with L, the optical conductivity is invariant with respect to L. However, the ratio of dc to optical conductivities often used as a figure of merit for transparent conducting thin films was shown to scale linearly with wire diameter, allowing us to write $\frac{\sigma_{DC,B}}{\sigma_{Op}} \propto \frac{L}{D}$. It must be noted that more work should be undertaken in order to understanding the individual dependence of the dc and optical conductivities on D.

Within the technologically relevant regime of $T > 90\%$, thin films were best described by percolation theory. In this case the dependence of T on R_s is controlled by two parameters: the percolation exponent, n, and the percolative figure of merit, Π. n was found to decrease with decreasing D while Π increased with decreasing D. In both cases, this behavior points to better opto-electrical performance for networks of lower diameter wires. This could be checked by calculating the expected sheet

resistance for a network with T=90%, $R_S^{T=90\%}$, which was found to fall rapidly with decreasing D. It was estimated that by preparing networks of wires with $D = 25nm$, values as low as $R_S^{T=90\%} = 25\Omega/\square$ could be obtained (for nanowires with length $L = 5\mu m$). In fact, since this work has been conducted Leem et al. have published a paper showing thin films of silver nanowires with transmittance $T = 90\%$ and sheet resistance $R_S = 12\Omega/\square$ by using silver nanowires with diameter $D = 25nm$ and length $L \sim 12\mu m$. This corresponds rather perfectly to our predictions for $R_S^{T=90\%}$ and shows that networks of silver nanowires with opto-electrical properties matching that of ITO are indeed within reach.

6

FLEXIBLE TRANSPARENT DIELECTRIC CAPACITORS WITH NANOSTRUCTURED ELECTRODES

6.1 INTRODUCTION

Many devices are on their way to becoming perfectly flexible and transparent with the help of a range of novel nanomaterials such as graphene, carbon nanotubes and metallic nanowires. With this in mind, devices have already been produced using those nanomaterials such as solar cells, touch screen panels or supercapacitors. However, little attention has been paid to one of the most basic electronic components: the dielectric capacitor. The previous chapter dealt with understanding the influence of the geometry of silver nanowires on the properties of the network. In this chapter, transparent flexible capacitors were built and their properties linked to the geometry of the device, namely the thickness of the dielectric layer and the thickness of the porous nanostructured electrode. First the optical and electrical properties of the electrode layer will be investigated in the context of a capacitive device. Then the device will be modeled as a simple equivalent circuit in order to extract the resistance and capacitance value from impedance spectroscopy data. It will be demonstrated that the transparency, capacitance and, in particular, series resistance depend on the nature of the electrode. Finally, the capacitors will be tested mechanically to check their integrity under tension and compression.

6.2 SAMPLE PREPARATION

Flexible, transparent capacitors require both dielectric and electrodes to be flexible and transparent. Polymer dielectrics are well known and can fulfill the criteria for flexibility

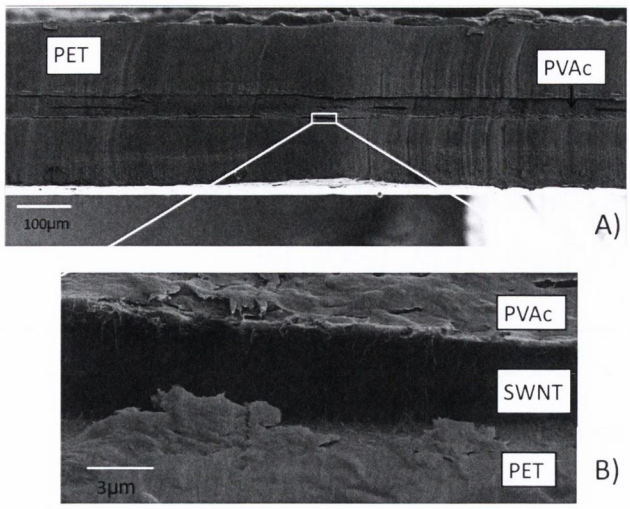

Figure 6.1: The "sandwich" method: electrodes were sprayed onto a PET substrate and subsequently encased in spin coated polymer then pressed together. This method of building the capacitor creates various weaknesses and fractures throughout the device. A) Cross section of the device shows the weakness of the design B) A close-up at the interface shows the carbon-nanotube network clearly suffering from the design.

and maximum transparency. In order to obtain an electrode that is transparent and flexible, it was necessary to choose from a pool of novel materials such as graphene, carbon nanotubes and silver nanowires. It was likely that electrode resistance would be relatively high because ultra-thin electrodes would be required to achieve high transparency. Therefore, the electrode would have to present high conductivity but also low surface roughness to obtain homogeneous capacitive properties. Carbon nanotubes were therefore an ideal candidate for this study.

Many methods were investigated for preparing transparent flexible capacitors. One method consisted in spraying a thin film of carbon nanotubes onto a PET substrate followed by the spin coating of a polymer layer on top of the electrode and finally spraying a second electrode on top. This configuration was ideal since spin coating can achieve very low polymer thicknesses and hence increase the range of capacitance that could be obtained. However, this configuration encouraged the formation of pinholes creating shorts in the device. Another method consisted in spraying two electrodes onto independent pieces of PET. Both were then encased in a layer of spin coated polymer

then heated up in order to render the polymer soft. The samples were then pressed together in order to bind the polymer layers. This configuration, which would have avoided shorts, was not structurally sound as the polymer presented a weakness at the interface between the two parts of the sample (see Figure 6.1). These methods were disregarded in profit of the method described below. To fabricate transparent, parallel electrode capacitors (Figure 6.2), free-standing polymer dielectric films were produced by drop casting a solution of polyvinyl acetate (PVAc in tetrahydrofuran (THF) at $C = 60\ mg/ml$) into a Teflon tray. This was then left to dry overnight, followed by further drying in an oven at 50^oC for $8\ h$ resulting in, relatively uniform, free-standing polymer films. The film thickness was controlled by the volume and concentration of solution deposited and was varied between $35\ \mu m$ and $90\ \mu m$. To deposit the electrodes, single walled nanotubes (SWNTs) produced by Iljin group[157] were dispersed in water with the aid of the surfactant sodium dodecyl sulphate, SDS ($C_{SWNT}= 0.15\ mg/ml$, $C_{SDS}=10\ mg/ml$). This dispersion was deposited onto both sides of the polymer film by spray casting using a Harder & Steenbeck infinity airbrush secured to a JANOME JR2300N robot. Spraying was performed using a $30\ psi$ back-pressure ($2.07 \times 10^5 Pa$) and a flow-rate of $2.5\ mm^3/s$, with the polymer film on a hotplate at 50^oC. As explained earlier (Chapter 2, section 2.2.3) the homogeneity of the network and hence better opto-electrical properties depend on the rate of evaporation of the droplets. Since it was necessary to stay below the glass transition temperature of the polymer, the CNT in SDS had to be sprayed at low temperature which meant the flow rate had to be kept very low to accelerate the evaporation rate and avoid agglomeration. The resulting capacitor was stored under ambient conditions for $24h$ before measurements were made. Note that the device could not be cleared of SDS since the usual methods, water baths and annealing of the sample, would have affected the polymer dielectric layer. Although PVAc is not soluble in water, some water could diffuse into the polymer which affected reproducibility greatly. Also, in order to rid the sample of SDS annealing temperatures would have had to be much higher than the glass transition temperature of PVAc. However, the increase in sheet resistance and transmittance due to the presence of SDS were low enough that carbon nanotubes still remained a good candidate for this

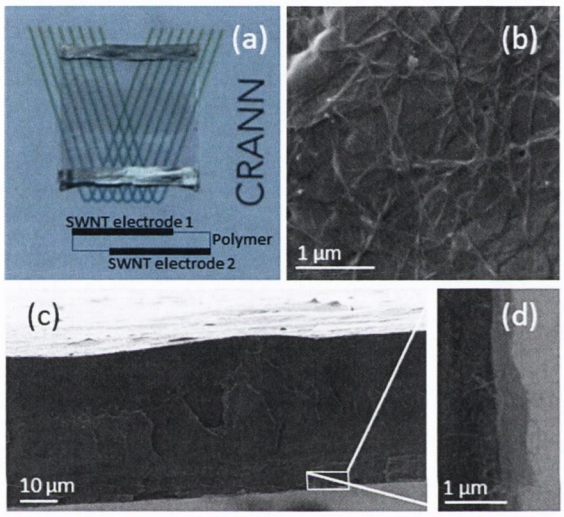

Figure 6.2: A typical flexible transparent capacitor: a) Photograph of a free standing capacitor (T = 74%)SEM of caps.The metallic bands at top and bottom are silver paint to facilitate connection to external circuitry. Inset: Schematic of the capacitor structure. b) SEM image of a spray-coated SWNT electrode at the surface of the polymer dielectric. (c) SEM image of a fracture surface of a typical capacitor. (d) Zoomed image of the capacitor edge showing protruding nanotubes. Note, (d) had been rotated by 90° relative to (c).

study. Furthermore, note that the devices were very robust and could be handled, manipulated, and flexed without apparent damage.

Scanning electron microscopy (SEM, Figures 6.2 (b)–(d)) measurements (Zeiss Ultra, samples coated with a *5 nm* thick layer of a Ti-Au alloy) show the deposited electrodes to consist of a very thin network of nanotube bundles similar to those prepared for other transparent electrode applications. By comparison with previous work, these networks were expected to be *5–20 nm* thick. As the capacitor electrodes were being deposited, a piece of PET was simultaneously sprayed (one side only) with SWNTs under identical conditions to facilitate the characterization of the electrodes individually. The transmittance of these individual networks (with PET film as reference) as well as that of the capacitors themselves (no reference) was measured using a Cary Varian 6000i spectrophotometer. Broad spectra similar to those reported previously were found in all cases. The sheet resistance, R_S, of the individual electrodes was measured using a Keithley source meter.

6.3 MEASURING THE PHYSICAL PROPERTIES OF THE DEVICE

6.3.1 *From electrodes to capacitor: Transmittance*

It is important in a complex device to study every element independently in order to separate the influence of each component on the measurements undertaken on the whole device. With this in mind, the transmittances of the individual electrodes (T_1, T_2, *550 nm*) are plotted against electrode sheet resistance (R_{S_1}, R_{S_2}) in Figure 6.3. Here, the subscripts 1 and 2 represent individual electrodes that were sprayed concurrently with the capacitor electrodes but on PET. These parameters will help to understand the data that will be obtained later using impedance spectroscopy. They are well described by

$$T = \left(1 + \frac{Z_0}{2R_S}\frac{\sigma_{Op}}{\sigma_{DC,B}}\right)^{-2} \tag{6.1}$$

The figures of merit were extracted from the data for both electrodes as shown in Figure 6.4 following the method covered in Chapter 5. Table 6.1 shows the values for the figures of merit for the electrodes. For both electrodes, $\frac{\sigma_{DC,B}}{\sigma_{Op}} \sim 3$ which is significantly

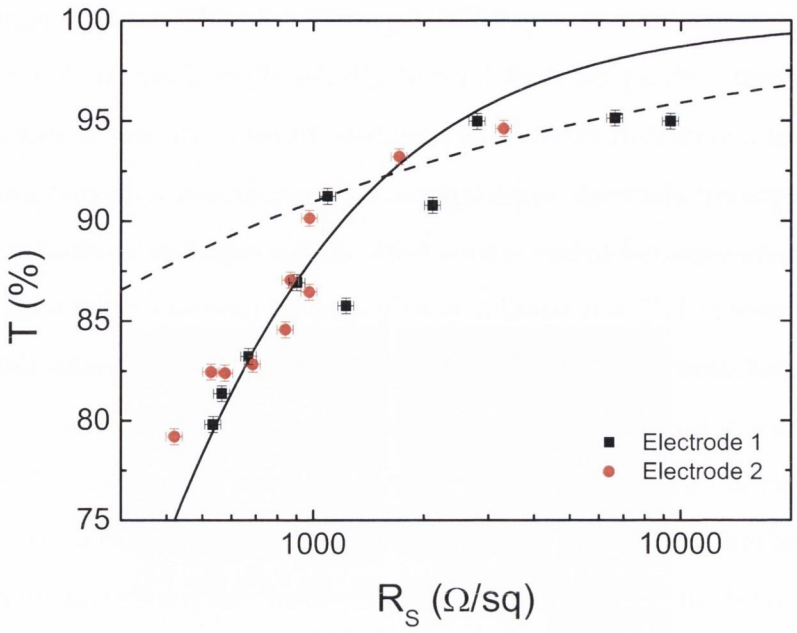

Figure 6.3: Transmittance versus sheet resistance, R_S, for individual nanotube networks, sprayed onto PET substrates at the same times as the capacitor electrodes were deposited.

	$\sigma_{DC,B}/\sigma_{Op}$	Π	n
Electrode 1	2.94	12.753	1.859
Electrode 2	2.89	15.927	1.7

Table 6.1: Figures of merit for the capacitor's electrodes for both the bulk and percolative regimes. The figures of merit for both electrodes are practically identical allowing us to assume identical electrodes on both sides of the capacitors. This will be used to relate the resistance measured by impedance spectroscopy and the sheet resistance of the electrodes.

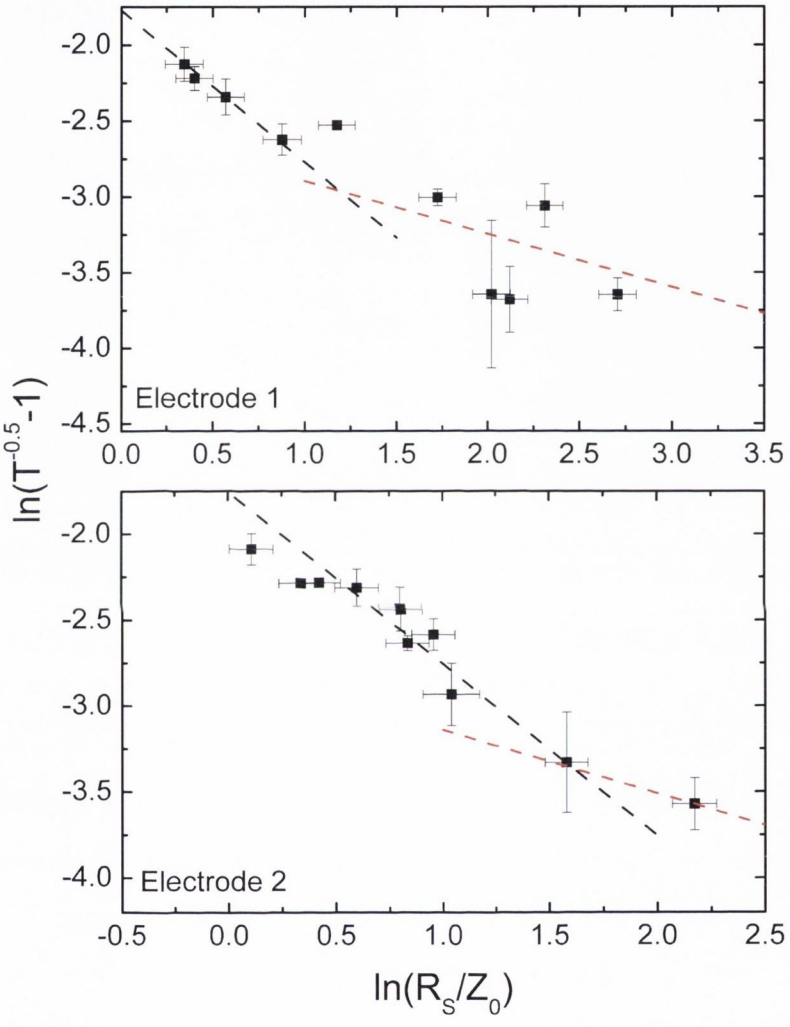

Figure 6.4: Fitting the bulk and percolative parts of the curve to find the figures of merit , $\sigma_{DC,B}/\sigma_{Op}$, for bulk networks and , Π and n, for percolative networks.

lower than the state of the art for transparent conductors. This can be explained by the presence of SDS among the nanotubes in the network which would increase dramatically the junction resistance in the network, the main source of resistance in nanotube networks[70, 87]. Moreover, the SDS was responsible for a visible haze on the surface of the film which must have an effect on the optical conductivity. State of the art figures of merit are however not necessary for showing the dependence of the properties of the device on its geometry, therefore carbon nanotubes will be sufficient for this study. In order to make sure the data for the capacitors and the individual electrodes can be compared, the product of transmittance for the electrodes was plotted against the transmittance for the whole device (Figure6.5). It is expected from the Beer-Lambert law that those would scale linearly with the slope equal to the transmittance for the polymer film:

$$T_{Cap} = e^{-\alpha_{CNT}(t_1+t_2)} e^{-\alpha_{Poly} t_{Poly}} \tag{6.2}$$

$$T_{Cap} = T_1 \times T_2 \times T_{Poly} \tag{6.3}$$

Indeed, the value of 88% for T_{Poly} found from fitting data in Figure 6.5 is in good agreement with measurements of the transmittance of PVAc films over a range of thicknesses ($45\ \mu m$-$75\ \mu m$) for which it was found that $85\% \leq T_{Poly} \leq 88\%$. T_{Poly} was not found to vary with varying thickness, this can be explained by the fact that the polymer was dropcast onto a surface with irregularities such as scratches and bumps. The resulting film was therefore not smooth and these scratches were probably the main source of scatter as the light went through the polymer films. This can be easily solved, in fact industry already has tools capable of fabricating highly transparent thin polymer films (e.g. thermal spraying or extrusing and rolling lamination[164]) which could be used in place of PVAc.

6.3.2 *Extracting information from Impedance data*

Impedance (Z) spectra (Gamry 600, V_{AC}= 25–$100\ mV$) were measured for a range of capacitors with various polymer and electrode thicknesses (for simplicity, the thicknesses of both electrodes were equal). It is possible to match the shape of the

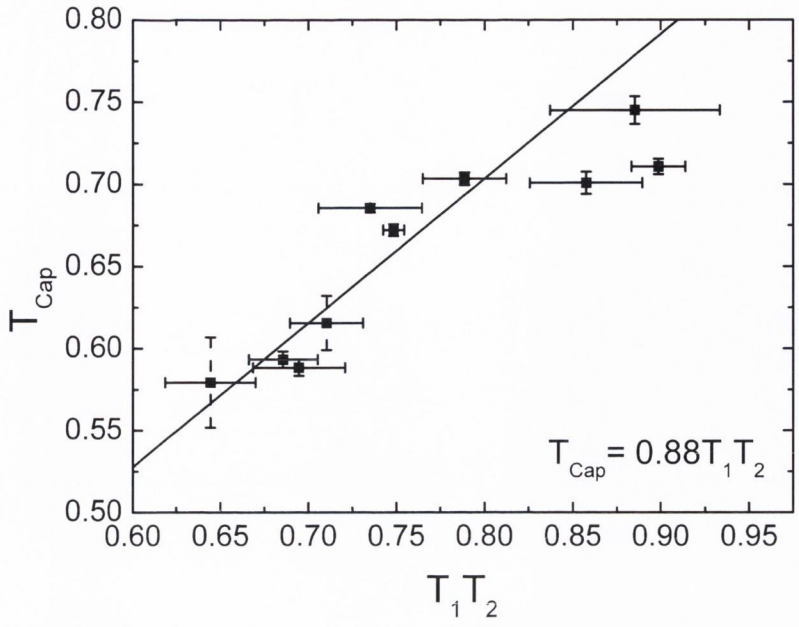

Figure 6.5: Capacitor transmittance versus the product of the transmittance of the individual films. The linear relationship shows a discrepancy in the transmittance of 88% which is attributed to the polymer's participation in the overall transmittance.

impedance spectra to equivalent circuits which, though not always representative of the actual circuit, describes the behaviour of the device. Figure 6.6 shows that the typical Nyquist plot of one of our transparent, flexible capacitor is a delta function which is representative of a series RC equivalent circuit. Shown in Figure 6.7 is the corresponding data for the the modulus of the impedance, $|Z|$, plotted as a function of angular frequency, ω, and the phase, φ, versus ω (NB: $Z = Z_{Re} + iZ_{Im} = |Z|e^{i\varphi}$). From this data it is possible to extract the values for the time constant $\tau = R_{Ser}C$, the series resistance R_{Ser} and the capacitance C of the device by using the definitions of impedance as shown below. As was covered in Chapter 3, the impedance of an RC circuit is defined as

$$Z = R_{Ser} - i\frac{1}{X_c} \tag{6.4}$$

where $X_c = \frac{1}{\omega C}$ is the capacitive reactance and it follows that the modulus is

$$|Z|^2 = R^2 + \left(\frac{1}{\omega C}\right)^2 \tag{6.5}$$

This can be used to find C and R_{Ser} by considering the fact that as $\omega \to \infty$ then $\frac{1}{\omega C} \to 0$ which leads to $|Z| = R$. This means if the lower part of the curve in Figure 6.7B) is

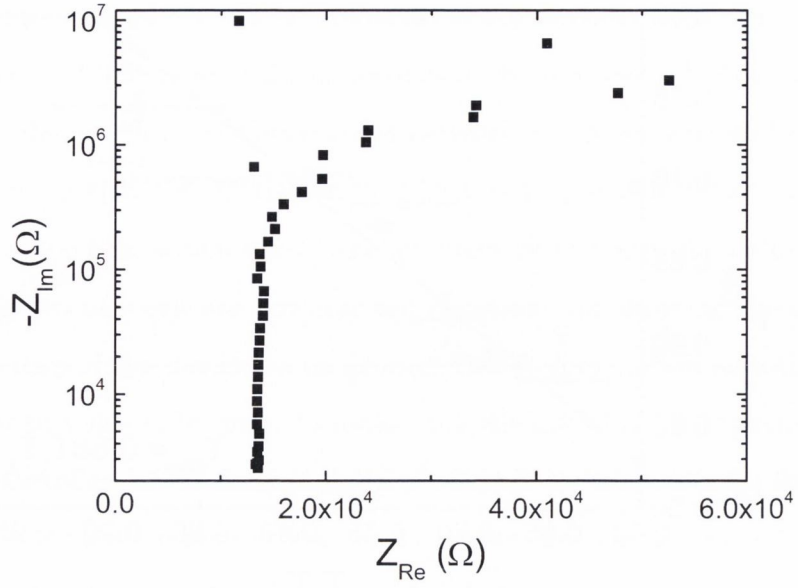

Figure 6.6: Typical Nyquist plot for the fabricated capacitors. The distinct delta function shape is typical of a series RC circuit. The scatter at very low frequency is due to the fact that the magnitude of the current response is lower than the magnitude of the error on the measurement. However, Nyquist plots are mainly used for understanding the equivalent circuit behaviour of the device so that such scatter is acceptable.

fitted and the slope is fixed to *zero* then R_{Ser} will be equal to the intercept. Identically as $\omega \to 0$ then $\frac{1}{\omega C} \to \infty$ (i.e. becomes very large) and the series resistance is negligible. In this case,

$$|Z|^2 = \left(\frac{1}{\omega C}\right)^2 \tag{6.6}$$

taking the natural logarithm

$$ln(|Z|) = -ln(\omega) - lnC \tag{6.7}$$

This means that fitting the higher part of the curve in Figure 6.7 A) and forcing the slope to be *-1* leads to $C = 10^{-intercept}$. This method can be used to find C and R_{Ser} for most samples. However, as the thickness of the electrodes increases the whole curve is shifted down due to the decrease in electrode resistance; in this case, a different method must be found. It can be noted that the impedance is made of two parts, the series resistance (Z_{Real}) which is invariant for a given sample and the reactance ($Z_{Imaginary}$) which varies with the frequency. Therefore, in Figure 6.6, the imaginary part of the impedance decreases with increasing frequency and eventually meets the real axis at

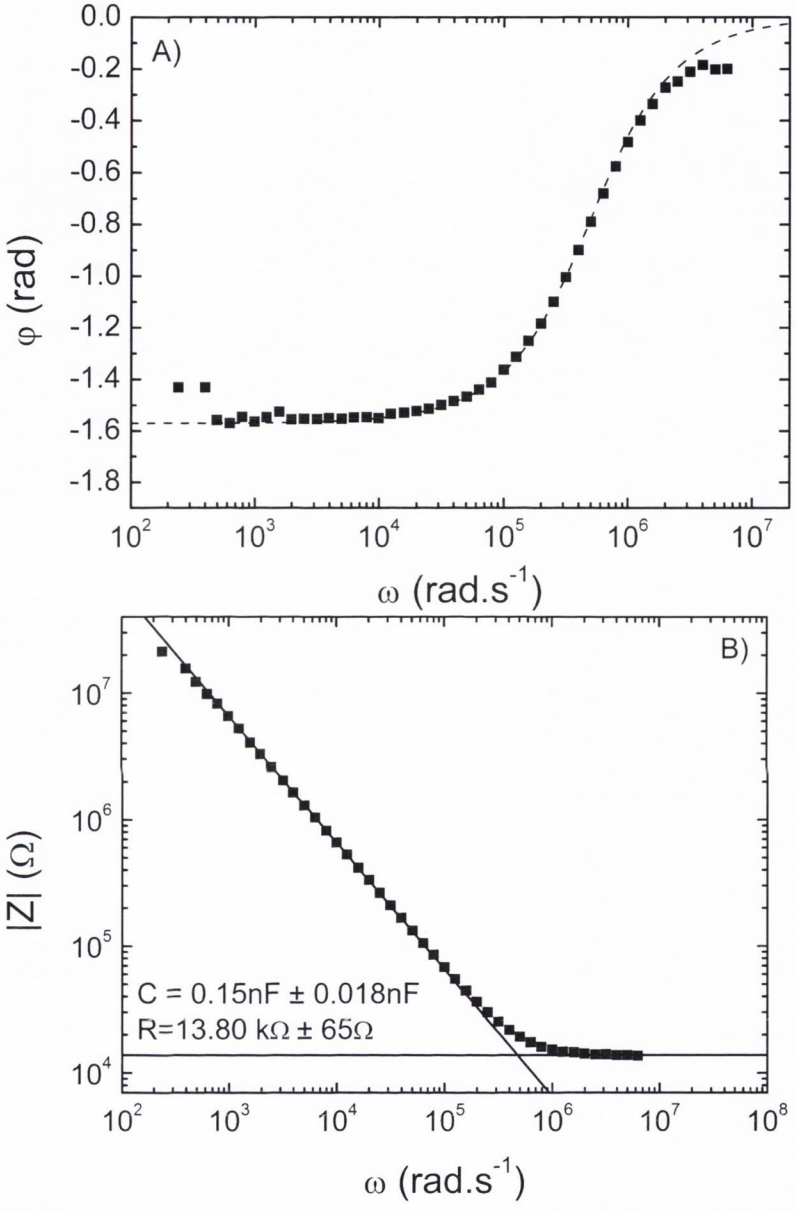

Figure 6.7: Bode plots: A) The phase as a function of frequency shows that for lower frequency, the phase shift between current and voltage is $-\pi/2$ which is representative of a series RC circuit. B) The modulus as a function of frequency shows two separate behaviours; completely resistive at very high frequency before the capacitive component becomes apparent for medium and low frequencies.

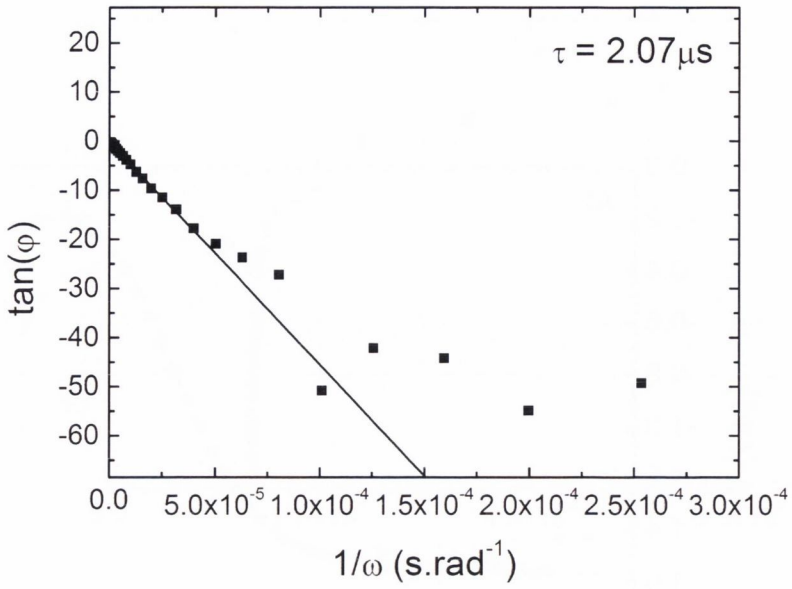

Figure 6.8: The time constant can be found by fitting the linear part of the data of $tan\varphi$ as a function of $1/\omega$. The data starts converging towards $-\pi/2$ for low frequencies as the time constant term becomes negligible.

R_{Ser} as $\omega \to \infty$. This can be used to find R_{Ser} for samples with thick electrodes and the Gamry Analyst software was used in this study. Finally, the time constant τ can be found from the phase data. For an RC series circuit, the phase is

$$\varphi = tan^{-1}\left(\frac{1}{\omega R_{Ser} C}\right) \tag{6.8}$$

where the time constant for the system is $\tau = R_{Ser}C$. Therefore by plotting $tan\varphi$ against $\frac{1}{\omega}$, $\frac{1}{\tau} = \frac{1}{RC}$ can be obtained as the slope of the linear part of the curve as seen in Figure 6.8. It can be noted that the curve stops being linear for lower frequencies, this can be explained by the fact that as $\omega \to 0$ then $\frac{1}{\omega} \to \infty$ which means that the $\frac{1}{RC}$ term becomes negligible and the phase converges towards $tan(\infty) = -\frac{\pi}{2}$. The value for the time constant extracted from the data in Figure 6.8 was then subbed into equation 6.8 in order to model the behavior of the phase. The model matched the data very well as shown in Figure 6.7 A) (dashed line). Furthermore, the time constant $\tau = 2.07\mu s$ matches the product of the series resistance, R_{Ser}, and capacitance, C, extracted from the data ($R_{Ser}C = 2.2\mu s$) in Figure 6.7 A) meaning that fitting the phase data is a second way to obtain R_{Ser} for thick electrodes.

It is important to study the electrodes independently from the capacitor in order to state whether the equivalent circuit is representative of the device. The transmittance was studied in the previous section, however it has not yet been demonstrated whether the series resistance in the equivalent circuit is due to the electrodes' resistances. Comparing the series resistance obtained from impedance studies and the sheet resistance of the electrodes measured independently using four point probing (see Figure 6.3) is not possible. Instead, it will be assumed that the device's electrodes behave as two resistances in series

$$R_{Ser} = R_{cap,1} + R_{cap,2} \tag{6.9}$$

noting that

$$R = R_S \frac{l}{w} \tag{6.10}$$

and assuming both top and bottom electrodes in the device have the same network properties i.e. same sheet resistance

$$R_{S,cap,1} = R_{S,cap,2} = R_{Ser,RE} \tag{6.11}$$

then

$$R_{Ser} = R_{Ser,RE} \frac{l_1}{w_1} + R_{Ser,RE} \frac{l_2}{w_2} \tag{6.12}$$

where $l_{1,2}$ and $w_{1,2}$ are the length and width of the device's two electrodes respectively. This leads to

$$R_{Ser} = R_{Ser,RE} \left[\frac{l_1}{w_1} + \frac{l_2}{w_2} \right] \tag{6.13}$$

or

$$R_{Ser,RE} = R_{Ser} \left[\frac{w_1 w_2}{l_1 w_2 + l_2 w_1} \right] \tag{6.14}$$

$R_{Ser,\,RE}$ now presents the right unit, namely $\Omega/\square$for comparison with the independent electrodes' sheet resistance. One last step to take is to average the values for sheet resistance obtained from four point probing. Assuming the two electrodes are in series

$$R_{AVG} = R_1 + R_2 \tag{6.15}$$

again using

$$R = R_S \frac{l}{w} \tag{6.16}$$

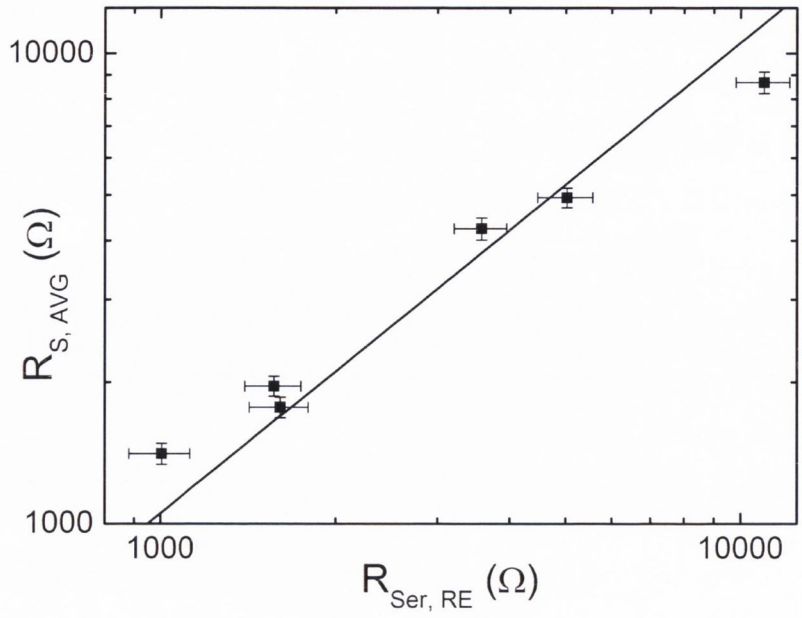

Figure 6.9: The average of the sheet resistance for the electrodes versus a series resistance to the same units. The data presents a linear relationship between the two, showing that the series resistance measured via impedance spectroscopy is in fact due to the resistance of the electrodes. The fitted line has equation $R_{S,AVG} = 1.053 R_{Ser,RE}$

we write

$$R_{S,AVG}\frac{l_{total}}{w_{total}} = R_{S,1}\frac{l_1}{w_1} + R_{S,2}\frac{l_2}{w_2} \tag{6.17}$$

$$R_{S,AVG} = \frac{w_1 + w_2}{l_1 + l_2}R_{S,1}\frac{l_1}{w_1} + R_{S,2}\frac{l_2}{w_2} \tag{6.18}$$

$R_{Ser,\,RE}$ and $R_{S,AVG}$ were plotted against each other as shown in Figure 6.9 which leads to the conclusion that within error, $R_{Ser,RE} = R_{S,AVG}$. It can be concluded that the series resistance measured by impedance spectroscopy is composed of the resistances in series of the two electrodes.

6.4 VARYING THE DIELECTRIC AND ELECTRODE THICKNESS

Now that the information relating to the properties of the capacitor has been extracted from the individual data, the geometry of the devices can be varied to investigate what consequences this has on the properties. Data sets for a number of capacitors with separately varying electrode and dielectric thicknesses were analyzed to give the

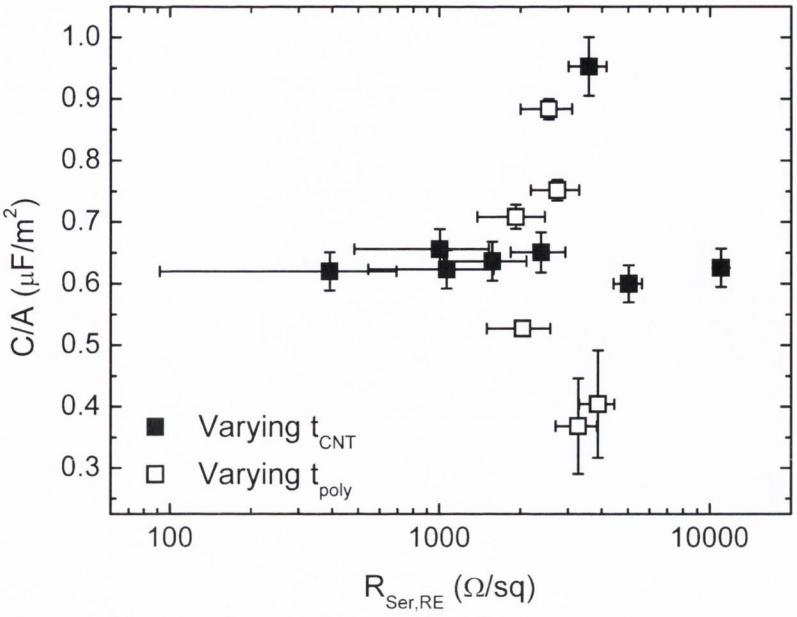

Figure 6.10: C/A plotted against $R_{Ser,RE}$ as the polymer and electrode thicknesses are varied. Changes in C/A are linked to changes in the polymer thickness while changes in $R_{Ser,RE}$ are linked to changes in electrode thickness

capacitance per overlapping electrode area, C/A, and series resistance R_{Ser}. As shown previously, to facilitate comparison between different capacitors, the measured series resistances are rescaled to represent square capacitors (units: $\Omega/\square$). The measured data is plotted in Figure 6.10. It is clear from this data that R_{Ser} depends solely on the electrode geometry while C/A depends solely on the polymer thickness. The scatter in the data for varying polymer thickness could be due to the difficulty to deposit the exact same amount of carbon nanotubes on both sides of each capacitor. The outlying data point for varying CNT network thickness could be due to scratches on the surface of the polymer from the teflon tray which would vary the capacitive area from one sample to the next or a mistake could have been made when measuring the volume of polymeric solution. The dependence of C/A on the thickness, t_{poly}, of the dielectric material is expected to follow

$$\frac{C}{A} = \frac{\varepsilon_0 \varepsilon_r}{t_{poly}} \tag{6.19}$$

It is shown in Figure 6.11 that this is indeed the case. This data is consistent with a dielectric constant of $\varepsilon_r = 3.64$, close to the expected value for PVAc of ~ 3 at room temperature [165]. The capacitances obtained here are not particularly high. This is

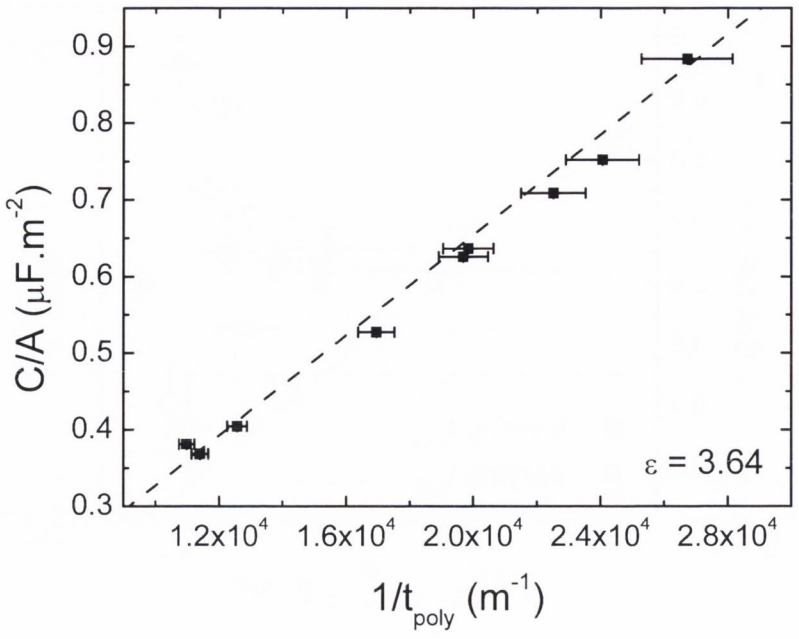

Figure 6.11: The capacitance per unit area scales linearly with the inverse of the polymer thickness following equation 6.19. The equation for the fit is $\frac{C}{A} = 3.22 \times 10^{-11} \frac{1}{t}$ leading to the permittivity of PVAc to be 3.64. This is in agreement with the literature.

largely due to the relatively low dielectric constant of PVAc and the relatively high thickness of the polymer dielectric. Both of these factors should be relatively easy to improve using existing materials.

It was shown in the previous chapter that it is very difficult to measure the thickness of networks of nanomaterials. Because of this, it is not possible to plot C/A and R_{Ser} as a function of electrode thickness. An excellent proxy for electrode thickness is the transmittance of the device, indeed the two are linked by

$$T = \left(1 + \frac{Z_0}{2}\sigma_{Op} t_{electrode}\right)^{-2} \tag{6.20}$$

where $\sigma_{Op}$is a property of the network and $Z_o$is a constant. Figure 6.12 show the transmittance of the capacitors plotted against C/A . Varying the thickness of the polymer (open symbols) changes C/A but hardly affects T or R_{Ser}. However, changing the thickness of the SWNT network (solid symbols) does not affect C/A but has a large effect on T and R_{Ser}.

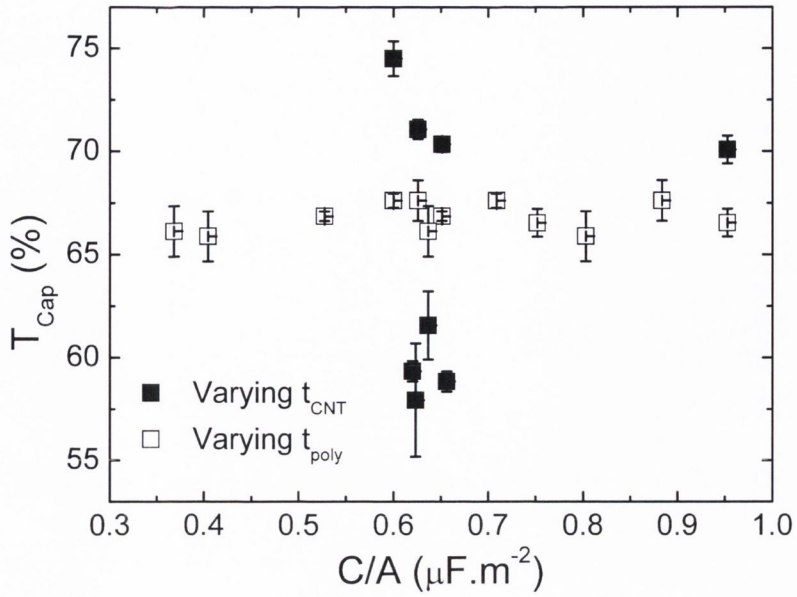

Figure 6.12: Capacitor transmittance as a function of areal capacitance . Data is shown for capacitors with either constant electrode thickness but variable polymer thickness or vice versa.

Finally, making the approximation that front and back electrodes are identical (i.e. $T_1 = T_2$, $R_{S,1} = R_{S,2}$, and $\frac{\sigma_{DC,B,1}}{\sigma_{Op,1}} = \frac{\sigma_{DC,B,2}}{\sigma_{Op,2}}$), and assuming that the rescaled series resistance is equal to the average of the electrode sheet resistances ($R_{Ser,RE} = R_{S,AVG}$), the transmittance of the capacitor can be related to the series resistance by the square of equation 6.1

$$T = \left(1 + \frac{Z_0}{2R_{Ser,RE}} \frac{\sigma_{Op}}{\sigma_{DC,B}}\right)^{-4} \tag{6.21}$$

Indeed the equation must be squared since $T_{cap} = T_{poly} \times T_1 \times T_2$ as it was shown previously. This curve is plotted on Figure 6.13 by the dashed line using $T_{poly} = 0.88$ and $\frac{\sigma_{DC,B}}{\sigma_{Op}} = 3$ and matches the data quite well.

6.5 MECHANICAL TESTING

Previous work has shown the electrical properties of nanotube networks to be robust under flexing, therefore the properties of our capacitive devices are expected to remain stable against bending. To test this, the impedance spectrum of a typical capacitor was measured in a planar arrangement (Figure 6.14, A)). R_{Ser} and C for this capacitor

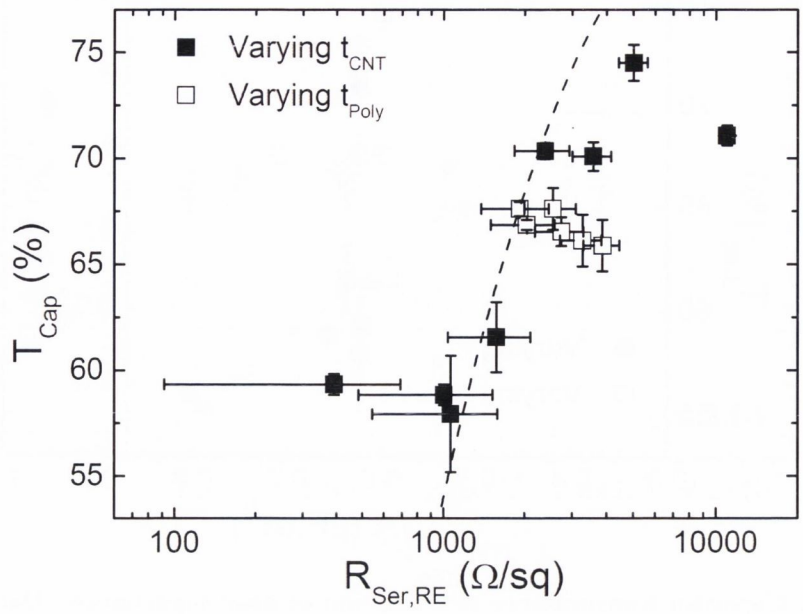

Figure 6.13: Capacitor transmittance as a function of series resistance. Data is shown for capacitors with either constant electrode thickness but variable polymer thickness or vice versa. The dashed line illustrates the behaviour expected for two identical electrodes, each described by the fit line in Figure 6.3, assuming a polymer transmittance $T_{poly} = 0.88$, $R_{Ser} = 2R_S$ and $\frac{\sigma_{DC,B}}{\sigma_{Op}} = 3$. Note that the series resistance here has been rescaled to make it represent a square electrode and so is presented in $\Omega/\square$

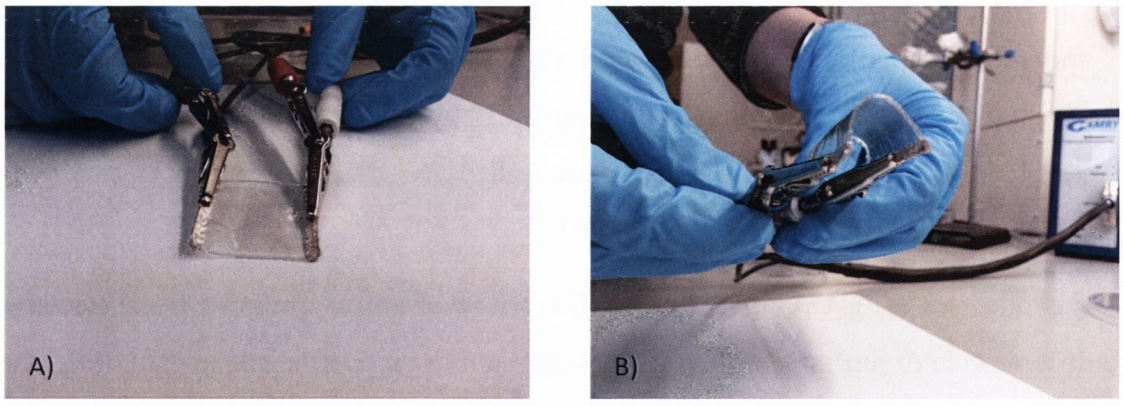

Figure 6.14: Measuring impedance on a capacitor A) Impedance is measured while the capacitor lays flat B) Capacitor is bent with a radius of curvature of *8 mm* and impedance measured to check mechanical stability of the device.

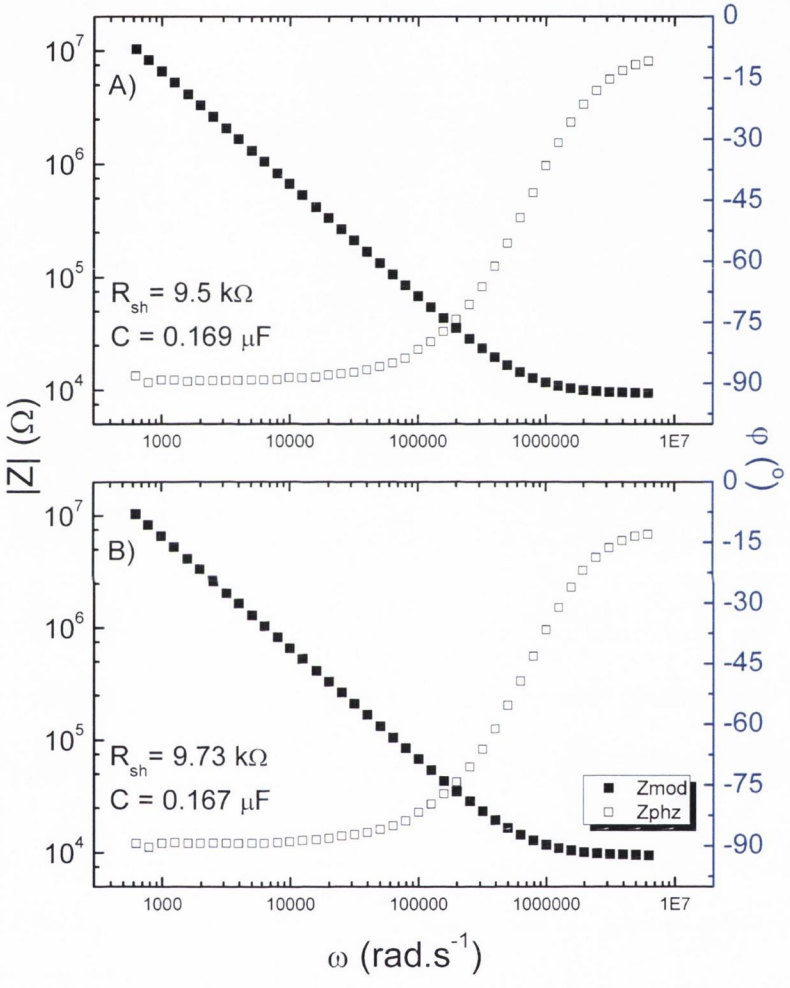

Figure 6.15: Impedance modulus and phase measured for a sample in a planar arrangement A) before and B) after bending as shown in Figure 6.14, B).

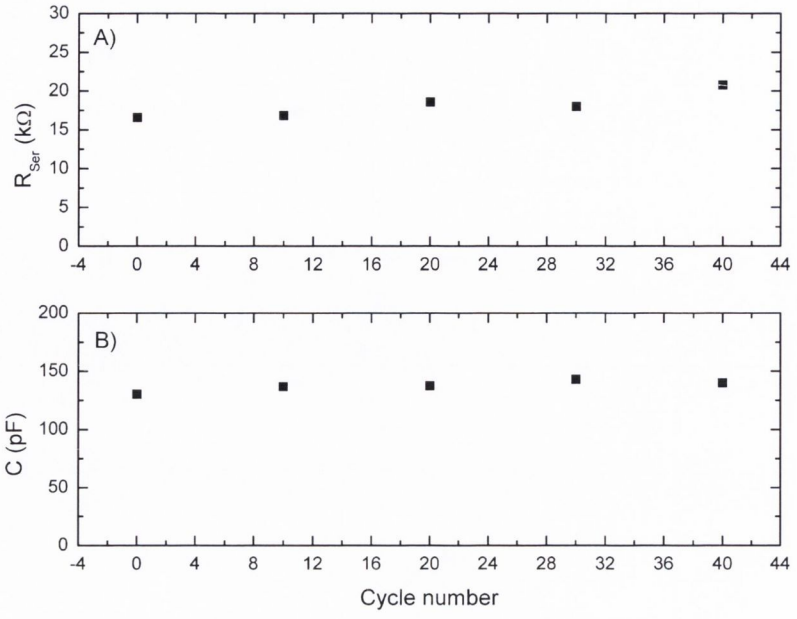

Figure 6.16: Flexibility test: A) Change in the series resistance over a large cycle number; the resistance increases slightly although this is believed to be due to a failure from the polymer substrate rather that the carbon nanotube electrodes. B) Change in the device capacitance over a large cycle number, the capacitance varies very little showing the sturdiness of the device.

were extracted from fitting the data as previously explained (Figures 6.15, A)). The capacitor was then bent to a radius of curvature of $\sim 8mm$ (Figure 6.14, B)), before measuring again the impedance spectrum (Figure 6.15, B)) and extracting C and R_{Ser}. The properties of the capacitor were found to be virtually indistinguishable before and after bending, demonstrating the robustness of the structure. To confirm this robustness, a (different) capacitor was subjected to repeated bend cycles ($\sim 8mm$ radius), measuring the impedance periodically. As shown in Figures 6.16, both R_{Ser} and C are stable under these conditions. The small increase in series resistance is believed to be due to a failure on the part of the polymer dielectric, indeed the polymer has brittle edges which formed during drying. The edges are believed to be responsible for the increased series resistance over the course of the cycles.

6.6 OTHER MATERIALS

In order for the devices to be industrially relevant, they have to be of use in circuits which are fully transparent and flexible. Therefore, the required conductivity of the device must be able to compete with the state of the art transparent conductors used nowadays. In order to ameliorate the properties of the capacitors, two more materials with different properties and advantages were investigated as a replacement for the carbon nanotube porous electrodes: silver nanowires for their very high conductivity and graphene for its very low surface roughness.

6.6.1 *Silver nanowires*

The capacitance per unit area for the carbon nanotubes device is quite low, ranging from *0.4* to *1.1* $\mu F.m^{-2}$, while the series resistance is extremely high, with values in the range of *2–10* $k\Omega$ for *70%* transmittance. As indicated above, it should be possible to increase the capacitance by using thinner polymer films and/or different dielectric materials. However, to reduce the series resistance, the conductivity of the electrode material must be increased. One material that would be ideal for such applications silver nanowires (from Kechuang Advanced Materials, $D = 35nm$, $L = 30\mu m$ Ltd.) which are considerably more conductive than SWNTs. To test this, a range of capacitors was prepared using a sheet of polyethylene terephthalate (PET) 37μm thick as the dielectric for simplicity and with both electrodes made up of sprayed networks of AgNWs. Those capacitors were prepared using the method described earlier for carbon nanotubes. Spraying was done at *40 psi* instead of *30 psi* and the nozzle was changed from a diameter of *200* μm to *600* μm to account for the size of the nanowires. Individually, these electrodes had transmittances in the range of *71* to *96%* and sheet resistances from *9* $\Omega/\square$ to *126.7* $k\Omega/\square$ (Figure 6.17), competitive with the state of the art for nanostructured transparent conductors. The capacitors fabricated from this method achieved transmittances much higher than that for SWNT capacitors paired with rescaled series resistances several orders of magnitude smaller. As for the SWNT capacitor study, Figure 6.18 shows the

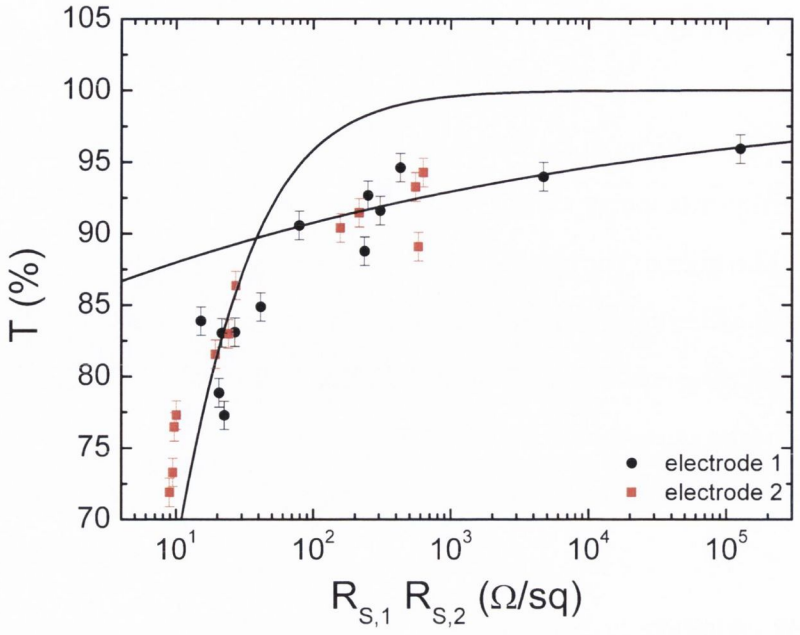

Figure 6.17: Transmittance versus sheet resistance, R_S, for individual silver nanowire networks, sprayed onto PET substrates at the same times as the capacitor electrodes were deposited. Here $\frac{\sigma_{DC,B}}{\sigma_{Op}} = 22.2$, $\Pi = 19.98$ and $n = 6.8$

transmittance of the device plotted against the product of the transmittance of the two electrodes. In the case of the silver nanowires, the relationship obtained is of the form $T_{Cap} = T_1 \times T_2$, in accordance with measurements for the transmittance of PET, $98\% \leq T_{PET} \leq 100\%$. Furthermore, the transmittance of the capacitors can be modeled as a function of series resistance using equation 6.21 for the bulk part of the curve and the following equation

$$T = \left[1 + \frac{1}{\Pi}\left(\frac{Z_0}{R_S}\right)^{1/n+1}\right]^{-4}$$

for the percolative part of the curve. This shows that even through the device superimposes two electrodes, it is possible to obtain transparent flexible capacitors with a transmittance of 85% for a series resistance of $400\Omega/\square$ (Figure 6.18).

6.6.2 *Graphene*

Graphene is another promising material for transparent flexible applications and although the conductivities achieved for a network of graphene has been quite low,

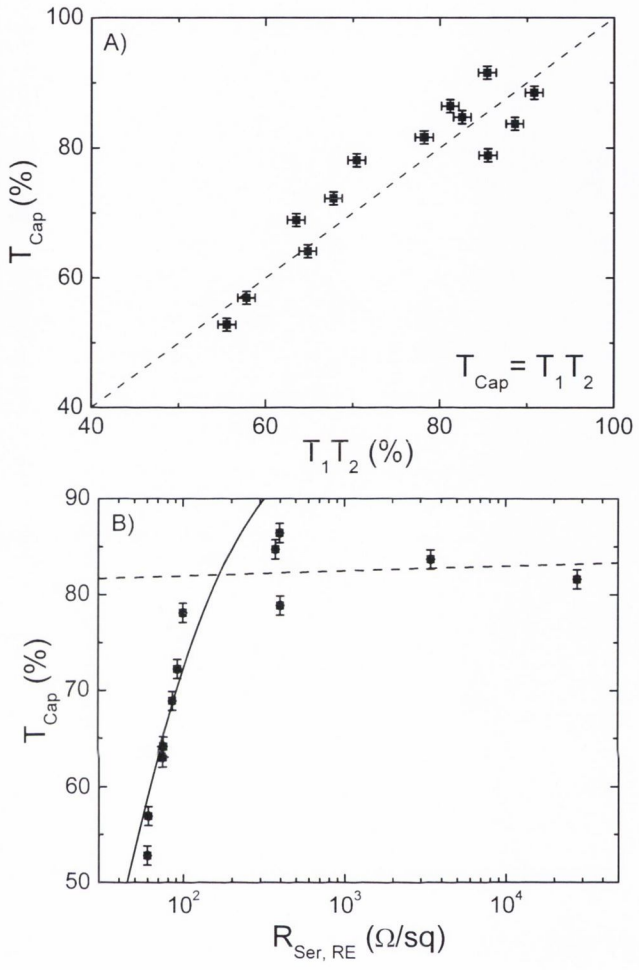

Figure 6.18: A) Capacitor transmittance versus the product of the transmittance of the individual films for silver nanowires. The linear relationship follows the fact that the transmittance of PET is close to 1. B) Capacitor transmittance as a function of series resistance. The lines illustrate the behaviour expected for two identical electrodes in the bulk (continuous line) and percolation (dashed line) regimes by subbing the FoMs obtained from the fits in Figure 6.17 into equation 6.21, assuming a polymer transmittance $T_{PET} = 1$, $R_{Ser} = 2R_S$ and $\frac{\sigma_{DC,B}}{\sigma_{Op}} = 22$. Note that the series resistance here has been rescaled to make it represent a square electrode and so is presented in $\Omega/\square$

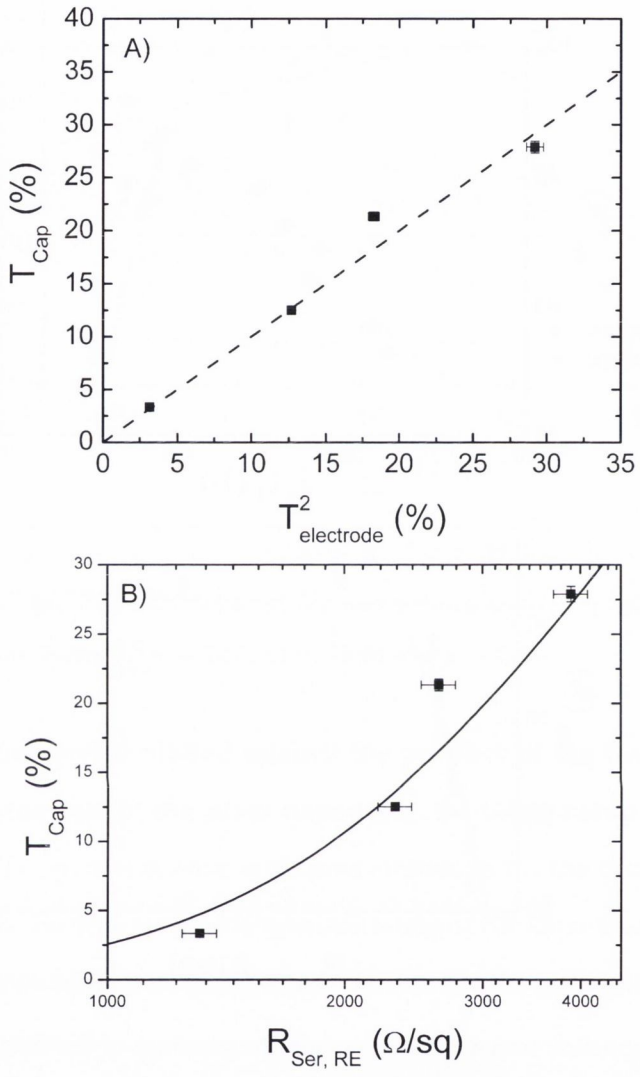

Figure 6.19: A) Capacitor transmittance versus the product of the transmittance of the individual films for graphene. The linear relationship follows the fact that the transmittance of PET is close to 1. B) Capacitor transmittance as a function of series resistance. The line illustrates the behaviour expected for two identical electrodes in the bulk regimes by subbing the FoMs obtained from T-R_{Ser} data into equation 6.21, assuming a polymer transmittance $T_{PET} = 1$, $R_{Ser} = 2R_S$ and $\frac{\sigma_{DC,B}}{\sigma_{Op}} = 0.1258$. Note that the series resistance here has been rescaled to make it represent a square electrode and so is presented in Ω/□

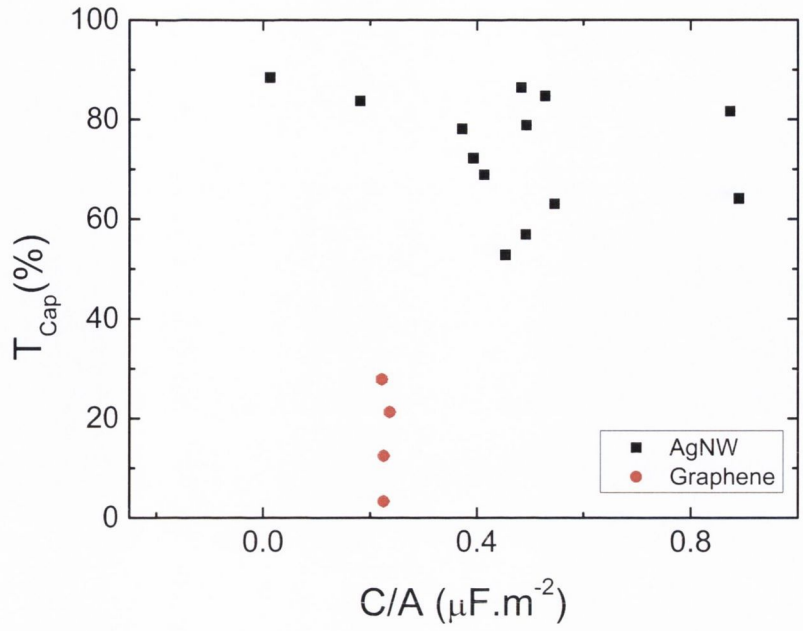

Figure 6.20: Capacitor transmittance as a function of areal capacitance for silver nanowires and graphene electrodes. The scatter supported in the silver nanowire data is believed to be due to the high surface roughness of the material. This theory is supported by the very low scatter in the graphene data which has very low surface roughness and by the uniform packing from vacuum filtration.

the nature of the material could be an advantage for this specific application. Indeed, graphene is a two dimensional nanomaterial yielding networks with very low surface roughness ($\geq$ *10 nm*) which would be a huge advantage to control the properties of the transparent flexible capacitors. The graphene capacitors could not be made using the spraying technology and so were fabricated using the transfer method outlined in Chapter *4.2*.Figure 6.19 shows the transmittance and sheet resistance achieved in the case of graphene. With a maximum transmittance of less than *30%* for a series resistance of nearly *4*k$\Omega/\square$ graphene is far from achieving the same performances as silver nanowires. However, nearly as much as high transparency and high conductivity, industry requires consistency. Figure 6.20 shows the data for T_{Cap} as a function of *C/A* for both silver nanowire electrodes and graphene electrodes (these can be compared since the polymer dielectric held the exact same thickness for every sample). The scatter in the case of the silver nanowire electrodes in massive ($\Delta\,(C/A) = C/A$ for some samples). This can be explained by the fact that the geometric surface area of the device

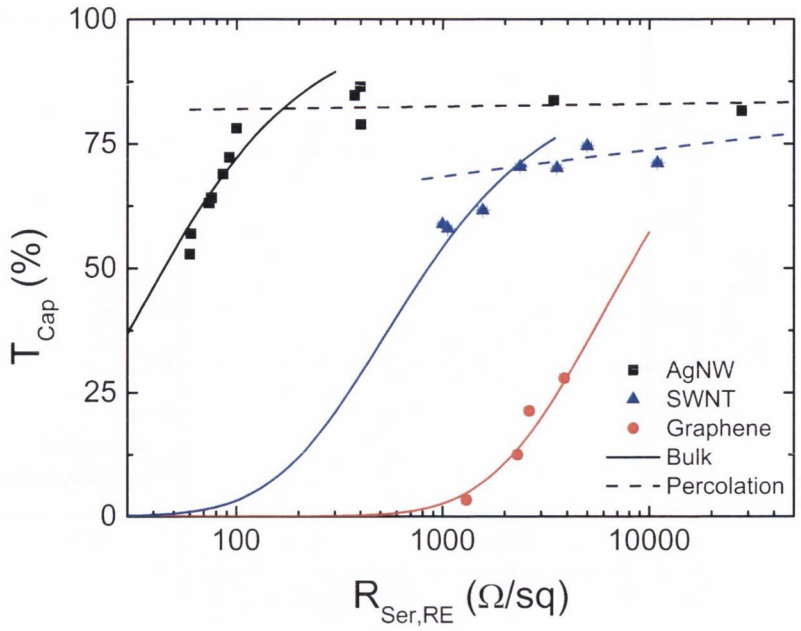

Figure 6.21: Transmittance as a function of rescaled sheet resistance of the devices for the three electrode materials: Silver nanowires, carbon nanotubes and graphene. Silver nanowires are the obvious choice to increase electrode conductivity and reduce the time constant $\tau = RC$.

is not the true surface area for the silver nanowires. Indeed, the surface roughness is so high ($\sim 40nm$) that the active area is most probably much larger than its geometric surface area (which is the area used in the study). This theory is supported by the fact that scatter is virtually non-existent in the case of graphene. Indeed, graphene has very low surface roughness ($\sim 1nm$) and hence active area is identical to geometric area in this case. The scatter in the silver data may have been emphasized by a lower than ideal homogeneity of the networks as shown by the high percolation exponent n obtained, as opposed to the graphene which was vacuum filtered. Increasing the homogeneity of the network may be a way of improving the use of silver nanowires as the electrode material for applications.

6.7 CONCLUSION

In conclusion, transparent capacitors were produced by spraying SWNT networks onto both sides of PVAc thin films and spraying AgNW or transferring vacuum

filtered graphene films onto both sides of a PET film. The properties of the SWNT capacitors were shown to be to be invariant with flexing over 40 bending cycles and the whole range of capacitors displayed transmittances between 5% and *86%*, capacitances ranging from *0.2* to *1.1* $F.cm^{-2}$ and series resistances ranging from $9\Omega/\square$ to $4k\Omega/\square$.

The properties of the capacitors were linked to the geometric structure of the device and to the nature of the transparent electrode material through impedance spectroscopy by analogy of the device to an simple equivalent RC circuit. It was shown that the measured series resistance for the equivalent circuit corresponds to the resistance of the two electrodes in series and that the equivalent resistance and transmittance of the device only vary with varying electrode thickness. Similarly, the areal capacitance of the device was shown to only be a function of the polymer thickness through $C/A = \varepsilon_r\varepsilon_0/d$ where d is the polymer thickness.

Silver nanowire capacitors displayed enhanced electrode conductivity (see Figure 6.18) while graphene, although displaying very low T for very large R_S, showed increased sample reproducibility due to its layered two-dimensional nature.

This simple study shows what can be done by harnessing the incredible properties of novel nanomaterials. Indeed, it was shown that simple devices such as dielectric capacitors can be controllably tuned to any specifications such as low sheet resistance, high transmittance, high capacitance, small time constant or large reproducibility. This in turn could be very useful for straightforward applications such as transparent and flexible gas, humidity or biosensors. Furthermore, it would be worth investigating associating the advantages presented by the various materials and create hybrid electrodes made from a blend of AgNWs, SWNTs or graphene. Spraying would be a powerful tool in this case as a range of different nanomaterials could be controllably layered on top of the substrate. In fact, insulating layered nanomaterials could be useful to this application, for example boron-nitride could be used as the dielectric layer between two layers of conducting nanomaterials dramatically increasing the capacitance and flexibility of the device while decreasing the thickness. This means it would be possible to build a string of capacitors in series by simply spraying down successive layers of conducting and insulating materials.

7

THE DEPENDENCE OF TEMPERATURE IN TRANSPARENT THIN FILM HEATERS ON FILM TRANSMITTANCE AND APPLIED CURRENT

7.1 INTRODUCTION

Transparent conductors acting as transparent flexible heaters (TFHs) have attracted the attention of the scientific community in recent years. Indeed, those devices pairing transparency, flexibility and heating power would be incredibly useful for any application where water condensation is problematic, from window defrosters in aviation to temperature-controlled liquid crystal display (LCD) displays, medical equipment or food packaging. Their very high transparency paired with excellent flexibility make silver nanowires an excellent candidate for such applications. Such silver nanowire heaters have already been fabricated and their properties studied as shown in Chapter 2. However, the dependence of the surface temperature on variables such as applied current or network thickness was not explained satisfactorily. The aim of this work will be to state what influences the saturation temperatures for thin flexible networks of silver nanowires and what dictates the time taken to achieve such temperatures. Finally, using all the information gathered, a 3D surface map of the saturation temperature as a function of current applied and film transparency will be generated.

7.2 SAMPLE PREPARATION

For this study, silver nanowires (AgNWs) were synthesized by Kechuang [166] and supplied as a suspension in isopropyl alcohol (IPA) ($C_{AgNW} = 16\ mg.ml^{-1}$). A small volume of the dispersion was diluted to $1.5\ mg.ml^{-1}$ in IPA then was subjected to 30

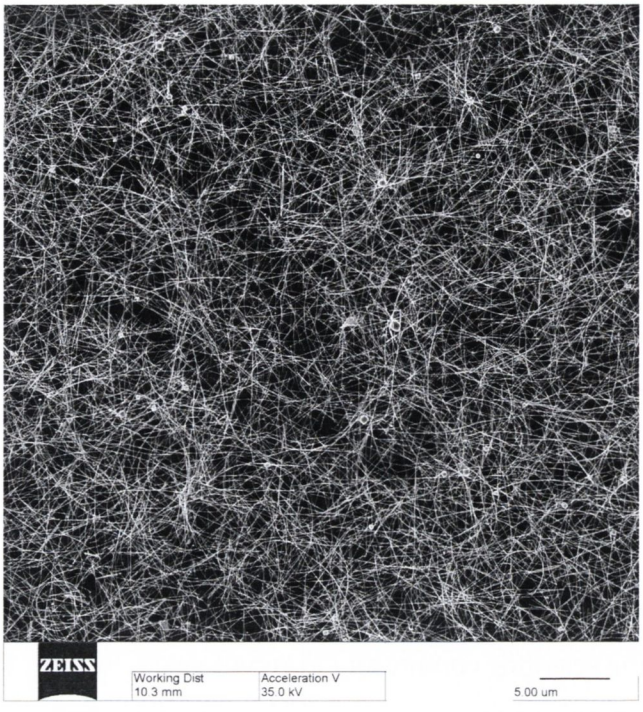

Figure 7.1: Helium Ion Microscope picture of a network of silver nanowires with transmittance $T = 61\%$, courtesy of Dr. Alan Bell (AML, CRANN, TCD).

sec low power sonication in a sonic bath (Model Ney Ultrasonic) to eliminate eventual bundles of nanowires. This solution was then further diluted to $0.15\ mg.ml^{-1}$ and sonicated another *30 sec* right before being sprayed onto polyethylene terephthalate (PET) squares of *2 x 2 cm* on a hotplate at $120^{o}C$. The temperature of the hotplate during spraying was ideal to both evaporate the IPA swiftly and to remove polymer residue left over from synthesis. Figure 7.1 shows a sample imaged via Helium Ion spectroscopy exhibiting the quality of the networks. A range of networks with different thicknesses were made and their transmittance and sheet resistance measured. The figures of merit for both the bulk and percolation regimes were extracted from the data as shown in Figure 7.2 and equations 3.9 and 3.29 were fitted to the data (Figure 7.3). The figures of merit obtained from the fits are $\frac{\sigma_{DC,B}}{\sigma_{Op}} = 70.44$, $\Pi = 25.83$ and $n = 5.6$ and it can be noted that the percolation exponent, n, is quite large meaning that the network is not very homogeneous. The samples were then taped onto a glass slide, placed on a piece of insulating foam and connected to a Keithley 2400 digital sourcemeter via silver wires which had been painted on with silver paint. A thermistor

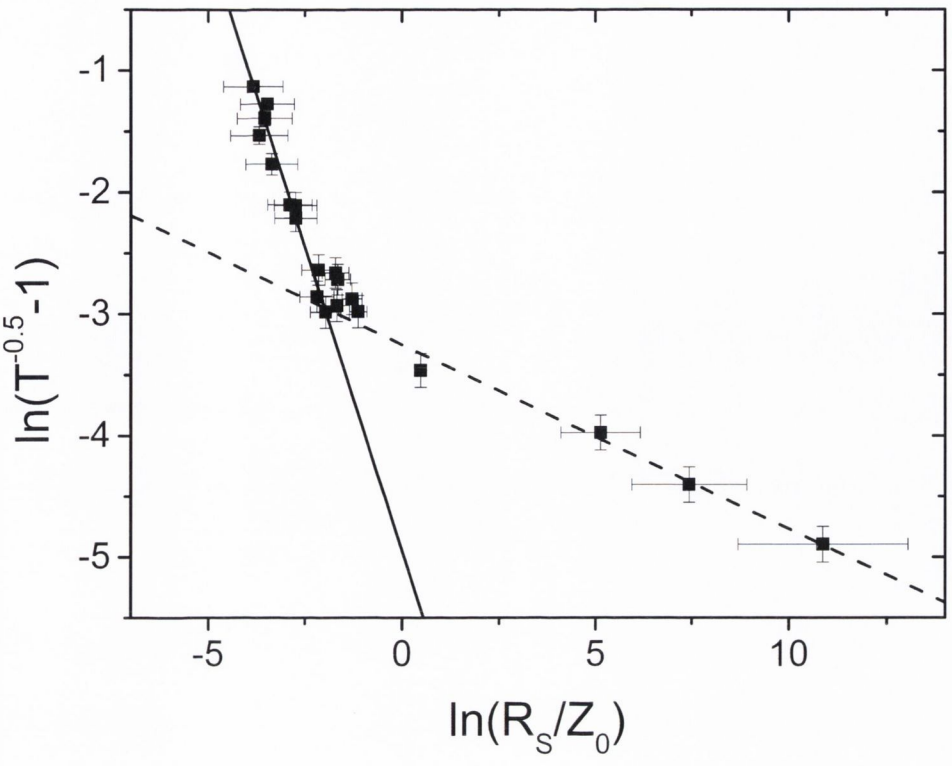

Figure 7.2: Finding the bulk and percolation figures of merit for the silver nanowire networks.

which was housed inside a hole in the side of a U-shaped copper clamp (secured using nail polish) was held in place with a small screw placed onto the sample at the midpoint between the silver electrodes (at the edge of the sample) as shown in Figure 7.4 and the temperature was recorded as a function of time using MATLAB.

7.3 TEMPERATURE DEPENDENCE ON TIME

The aim of the study of silver nanowires used as TFHs is to understand the complex relationship between the input power and the achieved surface temperature of the sample. As part of this thesis, expressions for the temperature at the surface of the heater as a function of time, sample transmittance and applied current were derived as follows.

The input power for an ohmic Joule heater is equal to

$$P = VI = I^2R = \frac{V^2}{R} \tag{7.1}$$

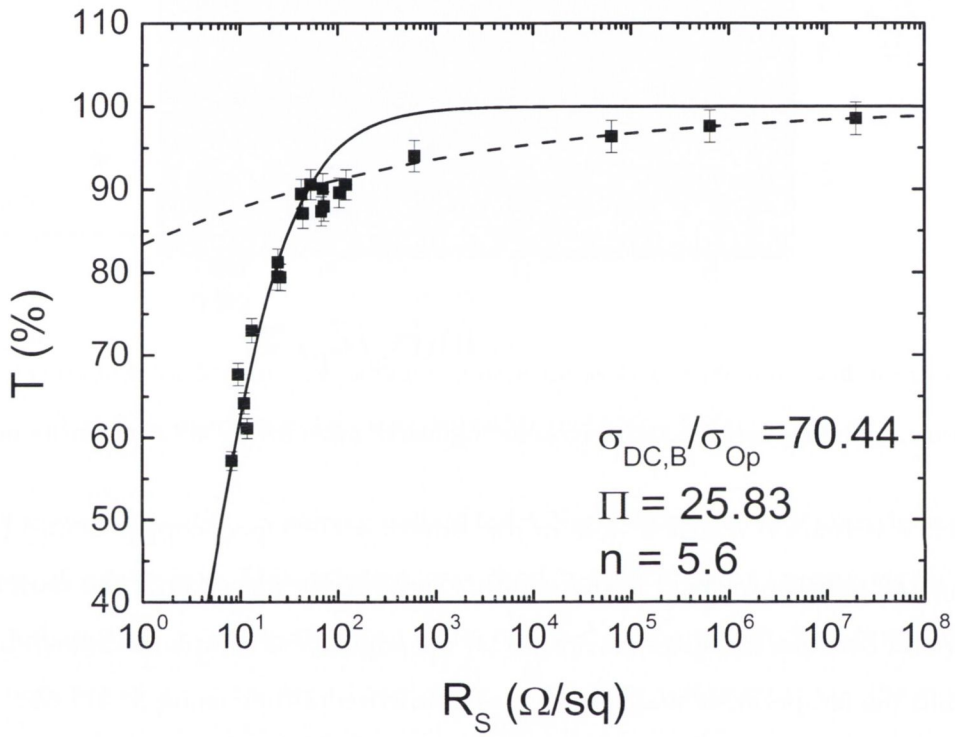

Figure 7.3: Data for the transmittance as a function of sheet resistance for the nanowires with diameter *25 nm* and length *30 μm* used in this study. The data can be divided into two regimes, the bulk-like regime and the percolative regime. These regimes have been fitted using equation 5.3 (solid line) and equation 5.4 (dashed line) respectively. The figures of merit obtained from the fits are $\frac{\sigma_{DC,B}}{\sigma_{Op}} = 70.44$, $\Pi = 25.83$ and $n = 5.6$.

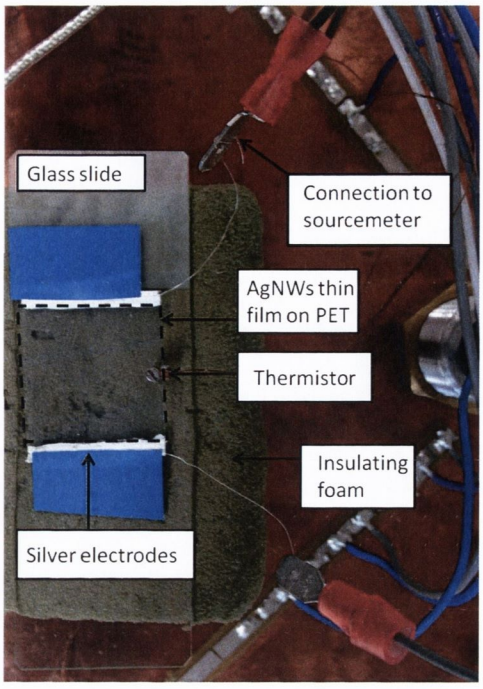

Figure 7.4: Setup for the temperature measurements. The thin nanowire film was taped down onto a glass slide and a thermistor secured onto the side of the sample with a screw. The whole setup was then covered inside an insulating chamber (not shown).

The electric power supplied is changed into heat and the temperature achieved is dictated by the specific heat capacity of silver as

$$P = \frac{dQ}{dt} = mc\frac{dT}{dt} \tag{7.2}$$

However, some heat is lost through radiation and convection as shown in Figure 7.5. Therefore the input power can be equated to the power used to heat the network to a temperature T, plus the power lost through convection, conduction and radiation (Figure 7.5)

$$P_{in} = m_1 c_1 \frac{dT}{dt} + P_{C1} + P_{R1} + P_{12} \tag{7.3}$$

Where the *conductive power loss* is

$$P_{C1} = h_1 A \left(T(t) - T_0\right) \tag{7.4}$$

the *radiative power loss* is

$$P_{R1} = \varepsilon_1 \sigma A \left(T(t)^4 - T_0^4\right) \tag{7.5}$$

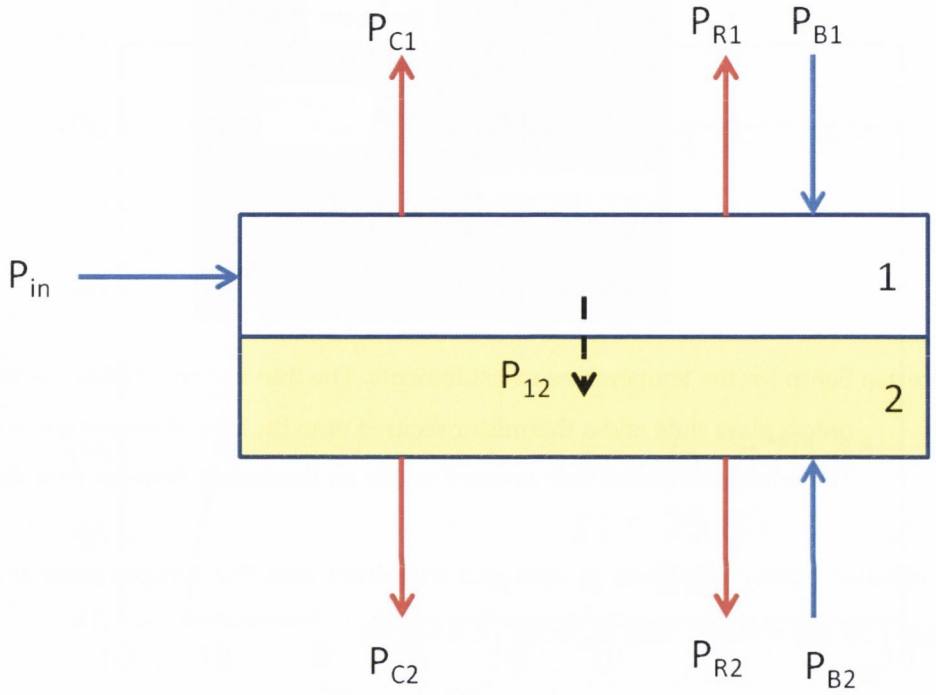

Figure 7.5: Power balance across the system. Current is driven across a silver nanowire network (1) causing it to heat up from Joule heating. P_{12}: Heat is lost to the substrate as it migrates to the PET substrate (2) through conduction. $P_{C1,C2}$: Power lost through convection for the network and substrate respectively; $P_{R1,R2}$: Power lost through radiation for the network and substrate respectively; P_{in}: Heat gained through radiation for the network and substrate respectively. $P_{B1,B2}$: Power gained through radiation of the background into the sample.

and the power lost to the substrate is

$$P_{12} = m_2 c_2 \frac{dT(t)}{dt} + P_{C2} + P_{R2} \tag{7.6}$$

The convective and radiative losses from the substrate are then

$$P_{C2} = h_2 A \left(T(t) - T_0\right) \tag{7.7}$$

and

$$P_{R2} = \varepsilon_2 \sigma A \left(T(t)^4 - T_0^4\right) \tag{7.8}$$

The T_o term in equation 7.5 arises from heat radiating from the surroundings back into the sample ($P_{B1,B2}$ in Figure 7.5) while A is the surface area of the film, σ is the Stefan-Boltzmann constant ($5.67 \times 10^{-8} W.m^{-2}.K^{-4}$), $h_{1,2}$ are the convection heat transfer coefficient of the air around the silver nanowire film and the substrate, $\varepsilon_{1,2}$ are the surface emissivities of the thin film and the substrate, $m_{1,2}$ are the masses of the network and the substrate, $c_{1,2}$ are the specific heat capacities of the nanowires and the substrate and T_o the initial surface temperature. This leads to an equation for the surface temperature as a function of time

$$\frac{dT(t)}{dt} = \frac{I^2 R}{(m_1 c_1 + m_2 c_2)} - \frac{(h_1 + h_2) A}{(m_1 c_1 + m_2 c_2)} \left(T(t) - T_0\right) - \frac{(\varepsilon_1 + \varepsilon_2) \sigma A}{(m_1 c_1 + m_2 c_2)} \left(T(t)^4 - T_0^4\right) \tag{7.9}$$

It is possible to expand the expression for the radiative power loss

$$T^4 - T_0^4 = (T_0 - \Delta T)^4 - T_0^4 \tag{7.10}$$

where $\Delta T = T - T_0$. Rearranging this and using a first order Taylor expansion leads to

$$\left(T^4 - T_0^4\right) = T_0^4 \left[1 + \frac{\Delta T}{T_0}\right]^4 - T_0^4 \tag{7.11}$$

$$\approx T_0^4 \left(1 + 4\frac{\Delta T}{T_0}\right) - T_0^4 \tag{7.12}$$

$$= 4 \Delta T T_0^3 \tag{7.13}$$

$$= 4 T_0^3 \left(T - T_0\right) \tag{7.14}$$

and in this case equation 7.9 becomes

$$\frac{dT(t)}{dt} = \frac{I^2 R}{(m_1 c_1 + m_2 c_2)} - \frac{1}{(m_1 c_1 + m_2 c_2)} \left[(h_1 + h_2) A + 4 (\varepsilon_1 + \varepsilon_2) \sigma A T_0^3\right] \left(T(t) - T_0\right) \tag{7.15}$$

From now on, β will be set as the *dissipation constant:*

$$\beta = \left[(h_1 + h_2)\, A + 4\,(\varepsilon_1 + \varepsilon_2)\,\sigma A T_0^3\right] \tag{7.16}$$

then

$$\frac{dT(t)}{dt} = \frac{I^2R}{(m_1c_1 + m_2c_2)} - \frac{\beta}{(m_1c_1 + m_2c_2)}\,(T(t) - T_0) \tag{7.17}$$

$$\frac{dT(t)}{dt} = -\frac{\beta}{(m_1c_1 + m_2c_2)}\left(T(t) - T_0 - \frac{I^2R}{\beta}\right) \tag{7.18}$$

$$\frac{dT(t)}{T(t) - T_0 - \frac{I^2R}{\beta}} = -\frac{\beta}{(m_1c_1 + m_2c_2)}dt \tag{7.19}$$

$$\int_{T_0}^{T} \frac{dT(t)}{T(t) - T_0 - \frac{I^2R}{\beta}} = -\frac{\beta}{(m_1c_1 + m_2c_2)}\int_0^t dt \tag{7.20}$$

$$ln\left(T(t) - T_0 - \frac{I^2R}{\beta}\right) - ln\left(-\frac{I^2R}{\beta}\right) = -\frac{\beta}{(m_1c_1 + m_2c_2)}t \tag{7.21}$$

$$T(t) - T_0 - \frac{I^2R}{\beta} = -\frac{I^2R}{\beta}exp\left(-\frac{\beta}{(m_1c_1 + m_2c_2)}t\right) \tag{7.22}$$

$$T(t) - T_0 = \frac{I^2R}{\beta}\left[1 - exp\left(-\frac{\beta}{(m_1c_1 + m_2c_2)}t\right)\right] \tag{7.23}$$

$$T(t) = T_0 + \frac{I^2R}{\beta}\left[1 - exp\left(-\frac{\beta}{(m_1c_1 + m_2c_2)}t\right)\right] \tag{7.24}$$

This expression predicts the temperature rise of the sample as a function of time, with a time constant $\tau = \frac{(m_1c_1 + m_2c_2)}{\beta}$. Once the input and output powers stabilize, the temperature of the sample reaches a *saturation temperature.* An example of this behaviour is shown in Figure 7.6 while equation 7.24 is fitted to the data and obviously matches the shape of the curve very well for the different currents. The temperature as a function of time was recorded for a range of samples with different transmittance and sheet resistance and for each sample, the dissipation constant, β, and the system's overall heat capacity, $m_1c_1 + m_2c_2$ were recorded as shown in Figure 7.7.

A few remarks must be made about β and $m_1c_1 + m_2c_2$. First, $m_1c_1 + m_2c_2$ is a function of fundamental properties of the system and should be constant; however, the very large error associated with measurements could explain the variation in $m_1c_1 + m_2c_2$ as it seems to be due to scatter from the data with 61% transmittance rather than follow a trend. Furthermore, assuming a mass of $1g$ and a specific heat of $1200 J.kg^{-1}K^{-1}$ [167]for the PET, we obtain $m_2c_2 = 1.2$ which is very close to the values

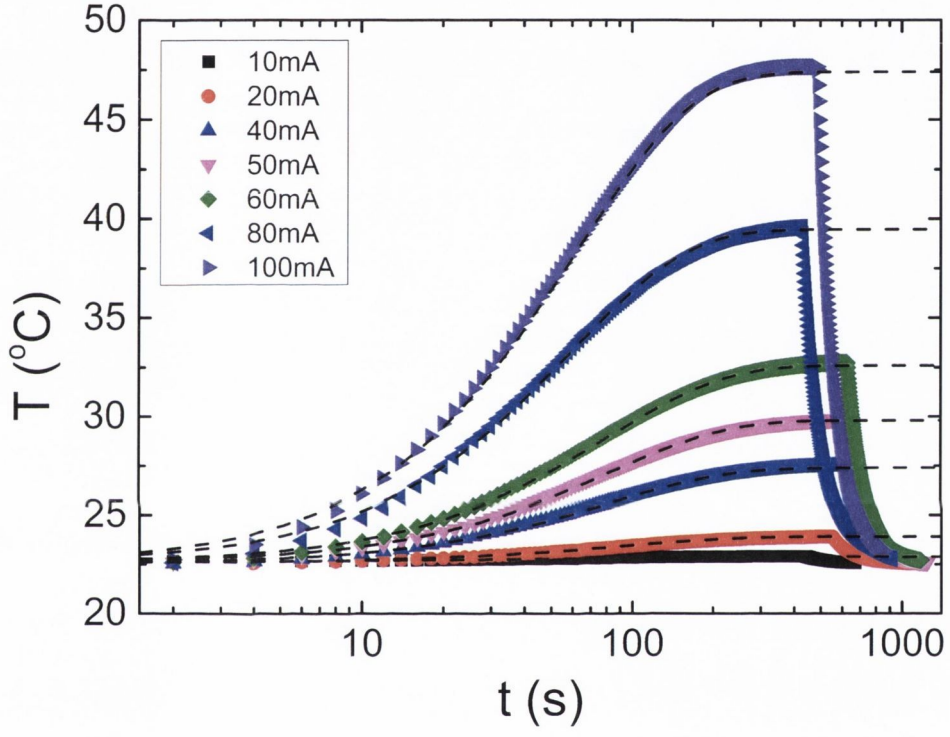

Figure 7.6: The temperature rise as a function of time. A current is driven through a sample with sheet resistance $R_S = 42\Omega/\square$ and the temperature is measured by a thermistor on the surface of the film as a function of time. Once the current is switched off, the temperature falls very quickly.

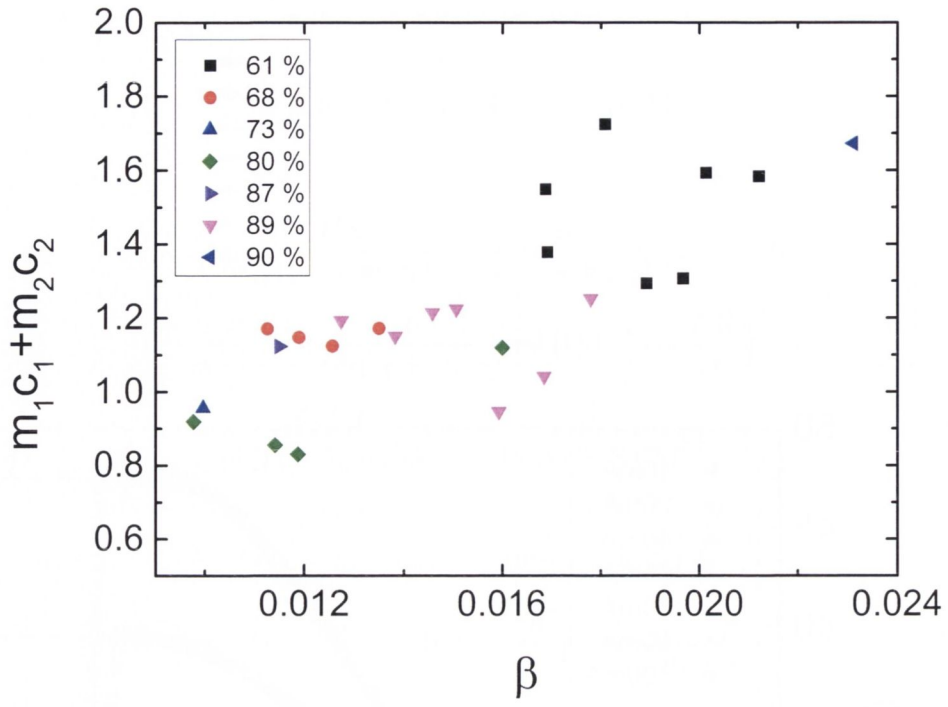

Figure 7.7: Dissipation constant and system heat capacity as a function of network transmittance. The scatter is most probably due to error associated with flaws in the setup.

shown in Figure 7.7, suggesting that the $m_1c_1 + m_2c_2$ term is dominated by the mass and specific heat of the PET.

Second, there seems to be a correlation between the two terms, however there is no pattern to this correlation as it is independent on film transparency (i.e. thickness). This seems to be brought on by a variation in β which can be explained by the fact that it is a function of both fundamental properties of the system and properties of the surroundings (see equation 7.16). Indeed, equation 7.16 suggests that β is dominated by the radiative term (T_0^3) which is several orders of magnitude larger than an estimated value for the convective term (h). This means the variation in β may have been brought on by the experimental chamber not being perfectly sealed or the initial temperature not being perfectly identical due to chiller variations, however we believe the error associated with β and $m_1c_1 + m_2c_2$ will be small enough in order to be able to draw conclusions about the saturation temperatures. Therefore, the rest of this work will

focus on understanding the dependence of the saturation temperature on the current applied and the network thickness.

7.4 TEMPERATURE AS A FUNCTION OF CURRENT

As $t \to \infty$, temperature loses its time-dependence and equation 7.24 becomes

$$T(t) = T_0 + \frac{I^2 R}{\beta} \tag{7.25}$$

or

$$T(t) - T_0 = \frac{I^2 R}{\beta} \tag{7.26}$$

The resistance can be replaced by the sheet resistance through its definition

$$R = R_S \frac{l}{w} \tag{7.27}$$

so that

$$(T - T_0) = \frac{R_S I^2}{\beta} \frac{l}{w} \tag{7.28}$$

Therefore plotting the temperature difference against the square of the current should lead to a slope of $\frac{R_S}{\beta} \frac{l}{w}$. Figure 7.8 shows equation 7.28 fitted to the data for samples with different thicknesses and subjected to a range of currents. It is obvious that this equation describes the data very well and equation 7.28 predicts that the slope for the different samples should scale linearly with R_S. The data in Figure 7.9 represents the slopes obtained above as a function of sheet resistance and it is obvious that they display a linear relationship, allowing us to write and assume $\beta = 0.0131$ for the remainder of this work.

7.5 TEMPERATURE AS A FUNCTION OF TRANSMITTANCE

For transparent flexible applications, it is very important to be able to predict the temperature that can be achieved for a particular network thickness. A good proxy for network thickness (actual thickness measurements yield very large error - see Chapter

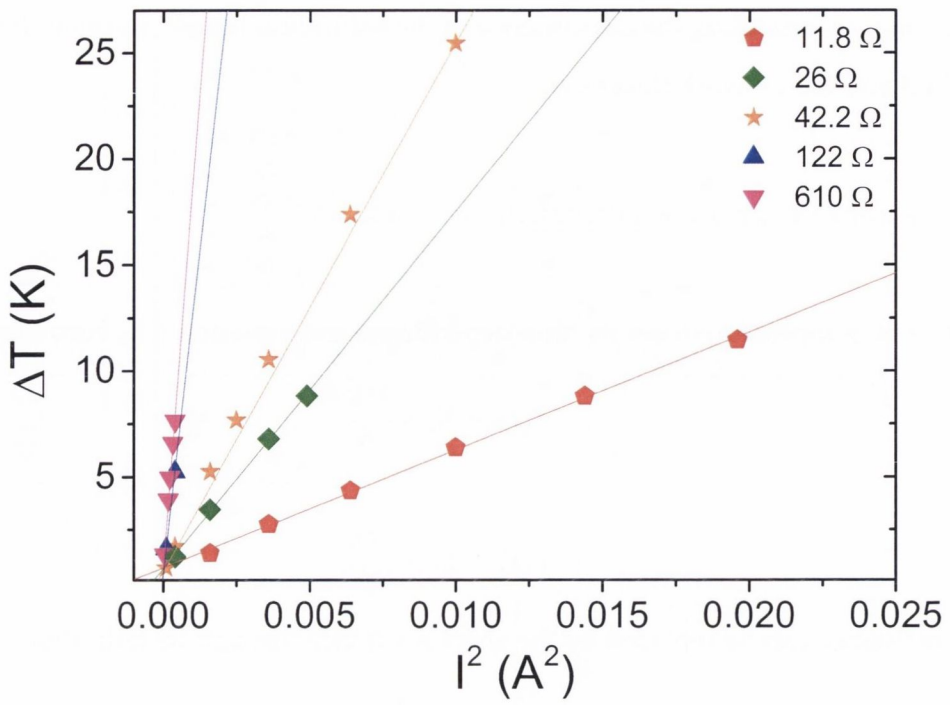

Figure 7.8: Temperature difference, $\Delta T = (T - T_0)$, as a function of current for a range of networks with different R_S. As the current is increased, the saturation temperature also increases. Decreasing the thickness of the film will have the same effect of increasing the saturation temperature.

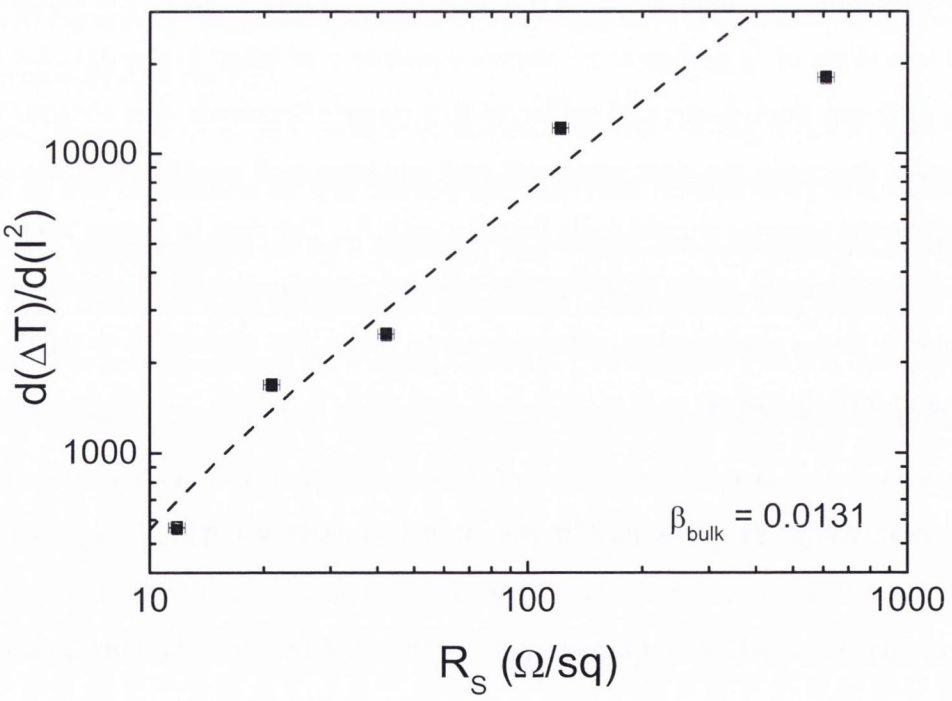

Figure 7.9: Plotting the slope of the fits in Figure 7.8 against the sheet resistance of each sample. The slopes increase linearly with sheet resistance, allowing us to write $\beta = 0.0131$.

5) is the transmittance of the sample. The definition of transmittance for thin metallic films in the bulk region (i.e. network conductivity is thickness-independent) is

$$T_{r,bulk} = \left[1 + \frac{Z_0}{2R_S}\left(\frac{\sigma_{Op}}{\sigma_{DC,B}}\right)\right]^{-2} \tag{7.29}$$

or

$$R_S = \left[\frac{1}{\sqrt{T_{r,bulk}}} - 1\right]^{-1}\left[\frac{Z_0}{2}\left(\frac{\sigma_{Op}}{\sigma_{DC,B}}\right)\right] \tag{7.30}$$

Subbing this into equation 7.28

$$(T - T_0) = \frac{R_S I^2}{\beta}\frac{l}{w}$$

allows us to write an expression for the steady-state temperature as a function of film thickness for a given current

$$I^2\left(\frac{1}{\sqrt{T_{r,bulk}}} - 1\right)^{-1}\left[\frac{Z_0}{2}\left(\frac{\sigma_{Op}}{\sigma_{DC,B}}\right)\right]\frac{l}{w} = \beta\left[T(T_{r,bulk}, I) - T_0\right] \tag{7.31}$$

$$\frac{T_{bulk}(T_{r,bulk}, I) - T_0}{I^2} = \frac{l}{w}\frac{1}{\beta}\left(\frac{1}{\sqrt{T_{r,bulk}}} - 1\right)^{-1}\left[\frac{Z_0}{2}\left(\frac{\sigma_{Op}}{\sigma_{DC,B}}\right)\right] \tag{7.32}$$

$$log_{10}\left[\frac{T_{bulk}(T_{r,bulk}, I) - T_0}{I^2}\right] = log_{10}\left[\frac{1}{\sqrt{T_{r,bulk}}} - 1\right]^{-1} + log_{10}\gamma \tag{7.33}$$

where

$$\gamma = \frac{1}{\beta}\frac{l}{w}\left[\frac{Z_0}{2}\left(\frac{\sigma_{Op}}{\sigma_{DC,B}}\right)\right] \tag{7.34}$$

In the same way, the definition for transmittance of a thin metallic film in the percolation regime can be subbed in to obtain the temperature of a percolative film as a function of film thickness and current applied

$$T_{r,perc} = \left[1 + \frac{1}{\Pi}\left(\frac{Z_0}{R_S}\right)^{1/n+1}\right]^{-2} \tag{7.35}$$

$$R_S = \left(\frac{1}{\sqrt{T_{r,perc}}} - 1\right)^{-(n+1)}\left(\frac{Z_0}{\Pi^{n+1}}\right) \tag{7.36}$$

$$\frac{T_{perc}(T_{r,perc}, I) - T_0}{I^2} = \frac{1}{\beta}\frac{l}{w}\left(\frac{1}{\sqrt{T_{r,perc}}} - 1\right)^{-(n+1)}\left(\frac{Z_0}{\Pi^{n+1}}\right) \tag{7.37}$$

$$log_{10}\left[\frac{T_{perc}(T_{r,perc}, I) - T_0}{I^2}\right] = (n+1)\,log_{10}\left[\frac{1}{\sqrt{T_{r,perc}}} - 1\right]^{-1} + log_{10}(\delta) \tag{7.38}$$

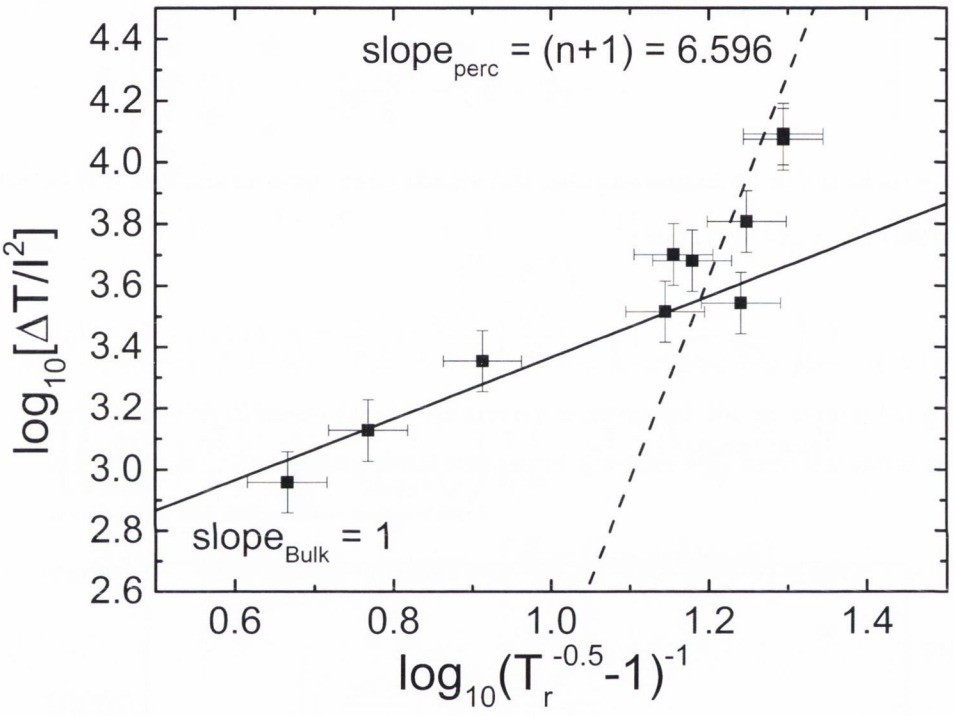

Figure 7.10: The logarithm of $\Delta T/I^2$ as a function of the logarithm of $\left(T^{-0.5}-1\right)^{-1}$ for a range of networks under an applied current of $20mA$. The data for bulk networks sits on a line with slope 1 while the data for percolative networks sits on a line with slope $(n+1) = 6.6$ meaning the expressions derived (equation 7.33 and 7.38) to describe network behaviour are accurate.

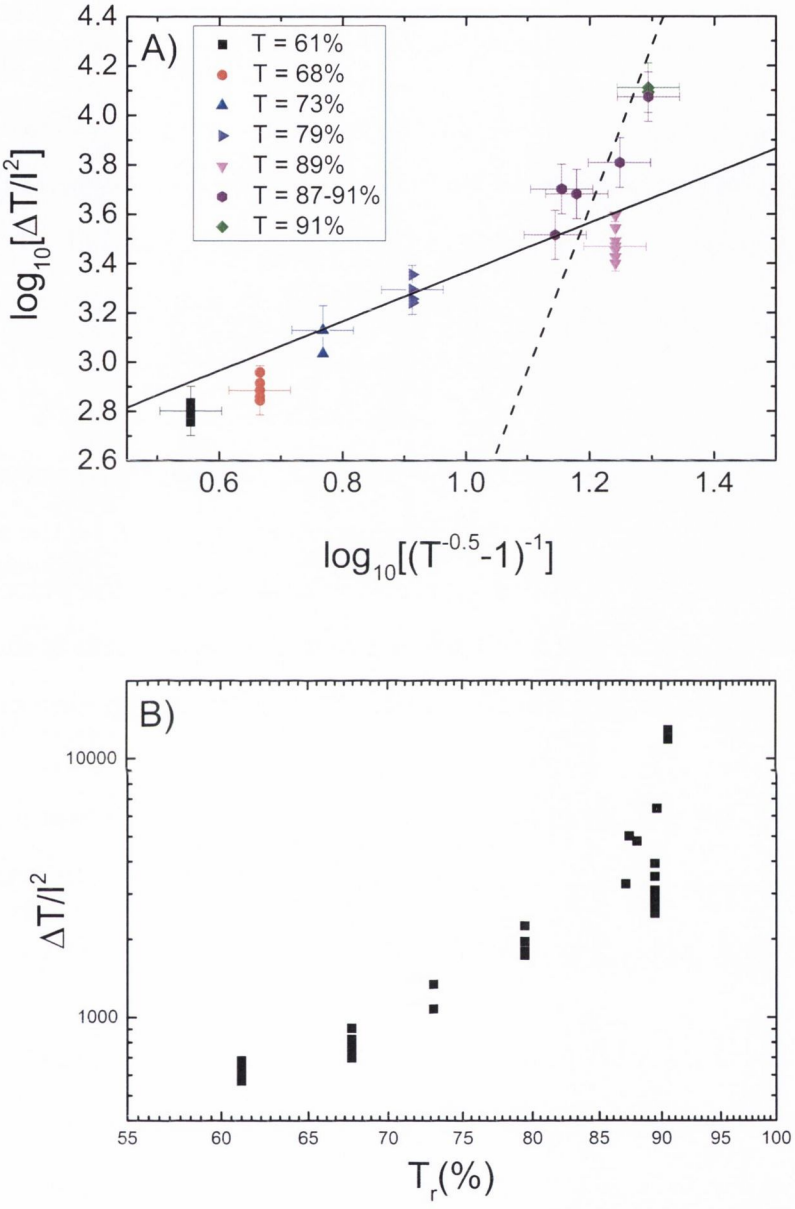

Figure 7.11: A) Representation of a range of networks with different transmittances under different currents. The temperature difference $\Delta T = (T - T_0)$ is normalised with respect to the square of the current so as to show all the data follow the same trend obtained from Figure 7.10 for both the bulk and percolative networks. B) The same data represented with more intuitive axes.

where

$$\delta = \frac{1}{\beta}\frac{l}{w}\left(\frac{Z_0}{\Pi^{n+1}}\right) \tag{7.39}$$

This means that plotting the natural log of the temperature difference against $\left(\frac{1}{\sqrt{T_{r,bulk}}} - 1\right)^{-1}$ should lead to a slope of 1 in the bulk regime and a slope of $(n+1)$ in the percolation regime. Data fitted to equations 7.33 and 7.38 is shown in Figure 7.10 (for an applied current of $20\ mA$). For both regimes, the data sits perfectly on the lines with slope 1 (bulk) and 6.6 (percolation) although there would ideally be more data points in the case of percolative networks. To formally link the saturation temperature to the film transmittance in the case of percolative networks, it would be necessary to produce more data points spanning transmittances from 92% to 99%.

Naturally, since the dependence on the current applied has been removed by dividing ΔT by I^2, the data for all currents and transmittance should fit on the same line with slope 1 for samples in the bulk regime and with slope 6.6 in the percolation regime, as shown in Figure 7.11 A). A more intuitive display of the data is shown in Figure 7.11 B). Scatter in the data can be explained by the small variation in β and by the fact that the large percolation exponent n (Figure 7.3) means that the network has low homogeneity which could cause spatial non-uniformity during heating and could be at the origin of the observed scatter. However, it would be easy to obtain equivalent data for networks with low n to verify this theory.

7.6 SURFACE PLOT OF TEMPERATURE AS A FUNCTION OF TRANSMITTANCE AND CURRENT

The temperature was shown to depend on the current applied and the thickness of the nanowire network. Therefore, using all the information that we have gathered, it is possible to theoretically predict the temperature achieved for a film with a certain transmittance under a chosen current. Indeed, the temperature can be defined as

$$T(T_r, I) = \frac{l}{w}\frac{I^2}{\beta}\left(\frac{1}{\sqrt{T_{r,bulk}}} - 1\right)^{-1}\left[\frac{Z_0}{2}\left(\frac{\sigma_{Op}}{\sigma_{DC,B}}\right)\right] + T_0$$

for a bulk film and

$$T\left(T_r, I\right) = \frac{l}{w}\frac{I^2}{\beta}\left(\frac{1}{\sqrt{T_{r,perc}}} - 1\right)^{-(n+1)}\left(\frac{Z_0}{\Pi^{n+1}}\right) + T_0$$

where the figures of merit $\frac{\sigma_{DC,B}}{\sigma_{Op}}$, n, Π have been extracted from Figure 7.2, β was extracted from the intercept in Figures 7.9 B) as 0.0131 and Z_0 is a known constant. Figure 7.12 shows a three dimensional surface plot of the temperature of the sample as a function of current applied and depending on the transmittance (i.e. thickness) of the network for bulk networks (A) and percolative networks (B). This shows that as the current increases, the temperature of the network increases which follows from the fact that the temperature depends on power input. More importantly, it shows that the temperature increase is maximised for thinner networks which is ideal for TFH applications. Indeed, this will minimise the amount of (expensive) nanowires needed for the devices, minimise the magnitude of the current applied and maximise the transparency of the heaters. The only drawback to such thin films is their weakness. As discussed in Chapter 2, silver nanowires will melt at much lower temperatures than bulk silver in a bid to minimise their surface energy. This means that as the temperature in the network reaches a threshold temperature, some nanowires or connective paths could break and render the network useless for sparse enough networks. Indeed, during this work, network breaking could be observed for some films with transmittance above 90% for currents between 5 and $20\ mA$. An example of such behaviour is shown in Figure 7.13.

7.7 CONCLUSION

A range of thin films of silver nanowires were made in order to be used as TFHs. The transmittance and sheet resistance for each film was measured using a spectrophotometer and 4-point probing in order to extract the figures of merit for the nanowires, obtaining $\frac{\sigma_{DC,B}}{\sigma_{Op}} = 70.44$, $\Pi = 25.83$ and $n = 5.6$. A range of currents was applied to each sample while the temperature as a function of time was measured and an expression derived and fitted to the data. The derived equation fit the transient data very well, however, the constants obtained from the fits seemed to vary between samples

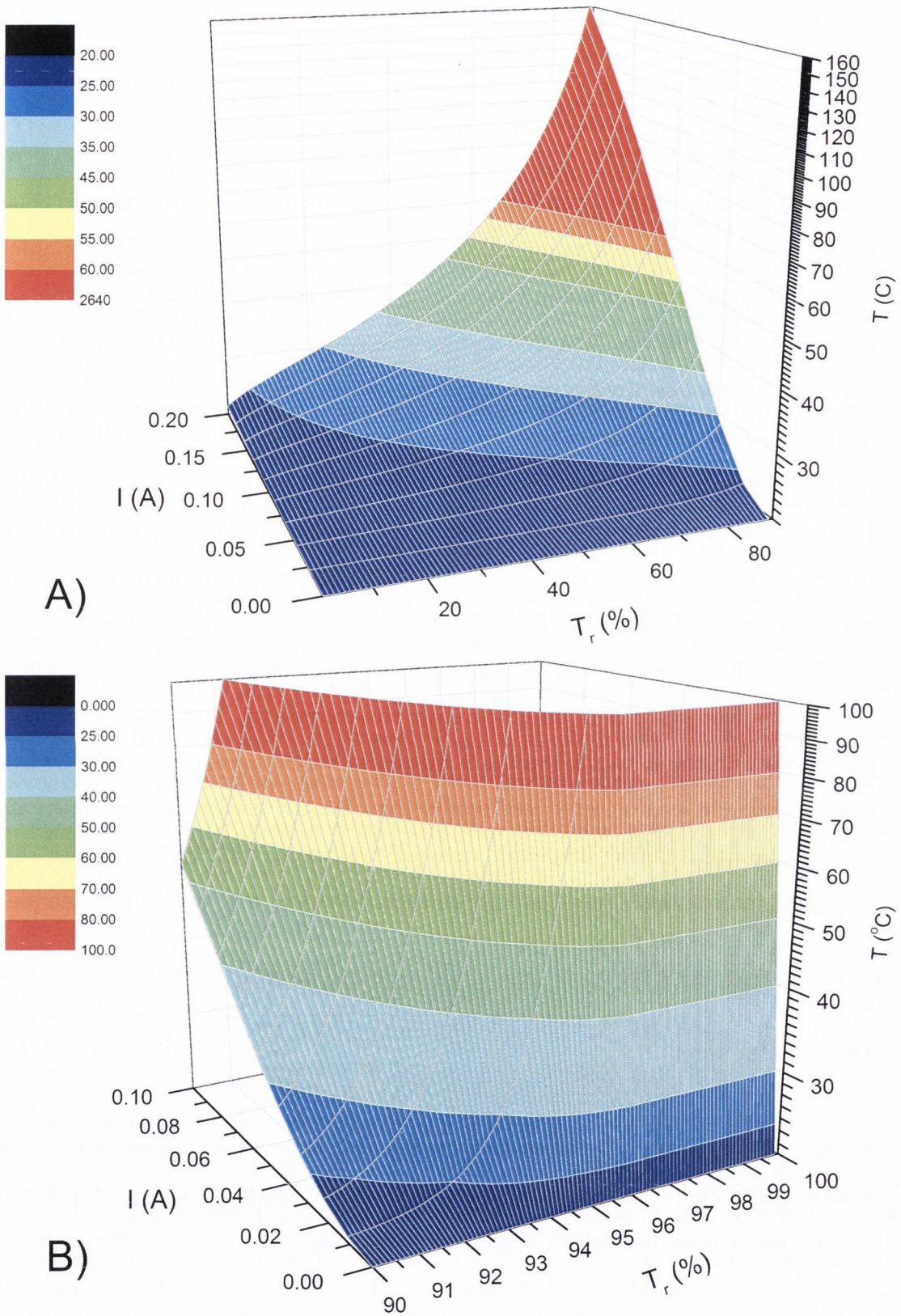

Figure 7.12: 3D surface plot of temperature as a function of current applied and network transmittance in the case of A) bulk networks and B) percolative networks. It is obvious from this graph that thinner films will be ideal for transparent flexible heater applications.

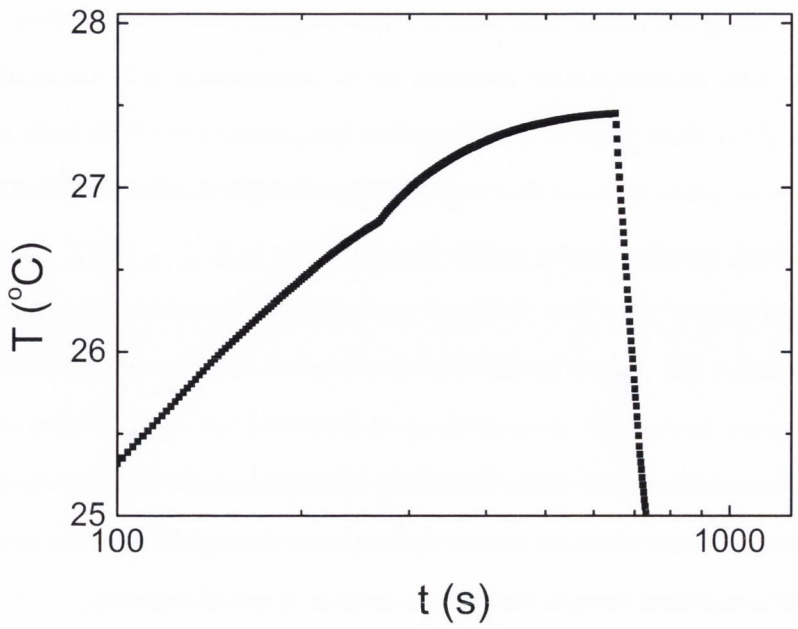

Figure 7.13: Failure of the network of silver nanowires as a current in applied: a current $I = 20mA$ was applied to a network with transmittance $T = 91\%$. The shoulder observed at $t \sim 270s$ is typical of conducting paths breaking, increasing the overall network resistance and hence increasing the temperature of the sample.

and for different applied currents. This variation in the constants can be explained by the large error associated with the measurements which are largely due to the setup. This scatter should be tackled in future work by improving the setup however for the sake of this study we allowed ourselves to assume constant β using the average value extracted from Figure 7.9. This is because standard deviation of 10% was deemed reasonable considering the scatter in the data as well as the shape of the dependence of the temperature on network transmittance (Figure 7.11) being independent of β.

At $t \to \infty$, the saturation temperature was attained and T_{sat} was characterised as a function of current applied for a range of samples and found to follow the derived expression for temperature as a function of current and sheet resistance, $(T - T_0) = \frac{R_S I^2}{\beta} \frac{l}{w}$, allowing us to obtain the average dissipation constant $\beta = 0.0131$ which arises from the heat loss mechanisms (convection and radiation).

Finally, the definition of transmittance for thin metallic films as a function of sheet resistance was used in order to relate the saturation temperature to film transmittance. The measured data behaved as expected for both bulk and percolative networks.

Understanding the mechanisms behind the dependence of the network temperature on current and transmittance allowed us to summarise this dependence through generating 3D surface plots of the saturation temperature for both bulk and percolative regimes. Those plots showed that higher temperatures can be obtained by using films with very high transmittance under low currents (e.g. $T = 100^{o}C$ for $T_r = 94\%$ and $I = 20mA$), however very thin films are more prone to breaking due to the temperature increase because the network only carries a limited number of conductive paths. This is inconvenient since high transparency is essential for applications such as heaters imbedded into motorcycle helmets or car windscreens. In the future, those 3D plots will permit us to tune silver nanowire networks to the right thickness in order to obtain the desired saturation temperature for a certain applied current.

8

CONCLUSION AND FUTURE WORK

8.1 CONCLUSION

The use of networks of nanomaterials, primarily silver nanowires, as transparent flexible electrodes for devices has been studied. Silver nanowires are a very promising material for TC applications as previous work has shown but the effects of their geometry (or aspect ratio) on network properties have never been investigated. The first objective of this work was to understand the reason behind the broad variation in the opto-electrical properties of silver nanowire thin films. In order to investigate the role played by nanowire length on network properties, nanowires were shortened using sonic energy. It was shown that the length of the wires followed a power law with respect to sonication time of the form $L \propto t^{-0.33}$ in line with theoretical and experimental work done with carbon nanotubes. Sonication induced scission is a powerful tool for tuning nanowires to industry specified requirements and was used in this work to study the effect of nanowire length on network properties, independently of diameter. It was found that while the bulk-like dc conductivity, $\sigma_{DC,B}$, of the networks scales linearly with L, the optical conductivity is invariant with respect to L. The increase in $\sigma_{DC,B}$ with increasing nanowire length can be explained by an increase in network connectivity which would result in more conducting paths across the sample.

A range of networks of silver nanowires with different lengths (L) and diameters (D) were then produced and their transmittance and sheet resistance measured. The networks displayed different behaviours above and below a certain thickness t_{min} and the transmittance as a function of sheet resistance was described through bulk (thick films) and percolation (thin films) theory. The ratio of dc to optical conductivity, $\frac{\sigma_{DC,B}}{\sigma_{Op}}$, is a figure of merit used in the area of TCs to describe the behaviour of thick networks -

where conductivity is independent of thickness - and was shown to scale linearly with wire diameter, allowing us to write $\frac{\sigma_{DC,B}}{\sigma_{Op}} \propto \frac{L}{D}$, though more work should be undertaken for understanding the individual dependence of the dc and optical conductivities on D. Furthermore, the conductivity ratio was shown to decrease with increasing nanowire diameter allowing us to write $\frac{\sigma_{DC,B}}{\sigma_{Op}} \propto \frac{L}{D}$ but because of the inaccuracy of network thickness measurements, it was not possible to conclude on whether the dc or the optical conductivity (or both) were responsible for this diameter dependence.

In the percolative regime, the new figures of merit Π and n were used to describe the behaviour of the properties of thin networks. Values found for nanowires of different diameters spanned $20 \leq \Pi \leq 56$ and $0.59 \leq n \leq 2.44$ and it was found that larger Π and smaller n lead to better opto-electrical properties, which coincides with nanowires with small diameters. In particular, previous work has shown that smaller n leads to more homogeneous networks, which explains the decrease in n for nanowires with small diameter. Π is quite an unintuitive figure of merit since it is a function of n, σ_{Op} and t_{min} (the transition thickness from percolative to bulk) and it is hard to relate it to the physical properties of the network. For this reason the sheet resistance at an industrially relevant transmittance of $T = 90\%$, $R_S^{T=90\%}$, was introduced. It was shown that $R_S^{T=90\%}$ decreases for decreasing nanowire diameter. It was estimated that by preparing networks of wires with $D = 25nm$, values as low as $R_S^{T=90\%} = 25\Omega/\square$ could be obtained (for nanowires with length $L = 5\mu m$). This prediction has since then been fulfilled through the work of Leem et al. who have recently published a paper showing thin films of silver nanowires with transmittance $T = 90\%$ and sheet resistance $R_S = 12\Omega/\square$ were produced by spin coating silver nanowires with diameter $D = 25nm$ and length $L \sim 12\mu m$. This shows that, before any post-deposition treatment, networks of silver nanowires with opto-electrical properties matching that of ITO are already within reach.

The aim of the second part of this thesis was to design and characterise simple transparent flexible devices based on our study of the properties of one-dimensional nanomaterials. The first system studied was the dielectric capacitor made transparent through the use of porous nanostructured electrodes. Transparent flexible dielectric capacitors were made using carbon nanotubes, silver nanowires or graphene networks

as the transparent flexible electrodes' material and PVAc or PET as the dielectric layer. Those devices displayed transmittance between 5% and 86%, capacitances ranging from *0.2* to *1.1* $F.cm^{-2}$and series resistances ranging from $9\Omega/\square$ to $4k\Omega/\square$ depending on electrode material. Impedance spectroscopy described the device through the use of an equivalent series RC circuit and it was shown that the series resistance of the equivalent circuit, R_{Ser}, was equal to the combined resistances of the electrodes in series.

Capacitors with CNT electrodes were characterised by varying the geometry of the device, namely the thickness of the electrodes and of the dielectric. It was shown that areal capacitance can be adjusted by varying the polymer thickness following equation $C/A = \varepsilon_r\varepsilon_0/d$, while the series resistance could only be controlled through the thickness of the electrodes. The transmittance of the device followed the definition for transmittance as a function of sheet resistance for thin metallic films, although the expression had to be squared to account for the two layers of carbon nanotubes that light must penetrate. Carbon nanotubes were found to be a good compromise between obtaining low enough surface roughness and high conductivity. However, silver nanowires would be an option worth examining for applications requiring very large conductivities. However, it was shown that the surface roughness of the nanowires paired with inhomogeneity from spraying may involve too much inconsistency for applications. Conversely, graphene was shown to display poor opto-electrical properties but showed incredible reproducibility.

This study showed what can be done by harnessing the incredible properties of novel nanomaterials. Indeed, simple devices such as dielectric capacitors can be controllably tuned to any specifications such as low sheet resistance, high transmittance, high capacitance, small time constant or large reproducibility. Many applications could follow from this work such as transparent and flexible gas, humidity or biosensors. Furthermore, materials could be paired in order to create electrodes pairing, for example, the high conductivity of silver nanowires with the consistency of graphene. Spraying would be a powerful tool in this case as a range of different nanomaterials could be controllably layered on top of the substrate. It would perhaps even be possible

to build a string of capacitors in series by simply spraying down successive layers of conducting materials and insulating materials such as boron nitride (BN).

The second type of devices characterised were transparent flexible heaters (TFH) made by using silver nanowire networks as Joule heaters. Those types of devices have been made in the past although the mechanism for heat transfer and heat loss has not been thoroughly investigated. A range of TFHs were made from networks of different thicknesses and their opto-electrical properties were characterised, obtaining $\frac{\sigma_{DC,B}}{\sigma_{Op}} = 70.44$, $\Pi = 25.83$ and $n = 5.6$. A range of currents was applied to each sample while the temperature as a function of time was measured and an expression derived to describe the data:

$$T(t) = T_0 + \frac{I^2 R}{\beta}\left[1 - exp\left(-\frac{\beta}{(m_1 c_1 + m_2 c_2)}t\right)\right] \tag{8.1}$$

The dissipation constant, β, was introduced and extracted from the transient data for different samples and different currents applied. It was found that the $m_1c_1 + m_2c_2$ and β terms are constant as expected with scatter due to flaws in the setup design. However, the study went ahead as a standard deviation on the data of 10% was deemed reasonable. Expressions for the saturation temperature (temperature at $t \to \infty$) as a function of current

$$(T - T_0) = \frac{R_S I^2}{\beta}\frac{l}{w}$$

and transmittance

$$\frac{T_{bulk}(T_{r,bulk}, I) - T_0}{I^2} = \frac{l}{w}\frac{1}{\beta}\left(\frac{1}{\sqrt{T_{r,bulk}}} - 1\right)^{-1}\left[\frac{Z_0}{2}\left(\frac{\sigma_{Op}}{\sigma_{DC,B}}\right)\right]$$

and

$$\frac{T_{perc}(T_{r,perc}, I) - T_0}{I^2} = \frac{1}{\beta}\frac{l}{w}\left(\frac{1}{\sqrt{T_{r,perc}}} - 1\right)^{-(n+1)}\left(\frac{Z_0}{\Pi^{n+1}}\right)$$

(for bulk and percolative networks respectively) were derived and were shown to describe the data very well. The dissipation constant was extracted from the data with an average value $\beta = 0.0131$. Understanding the mechanisms behind the dependence of the network temperature on current and transmittance allowed us to summarise this dependence through generating a 3D surface plot of the saturation temperature. This plot showed that higher temperatures will be obtained by using films with higher

transmittance under high currents (e.g.. $T = 100^{o}C$ for $T_r = 94\%$ and $I = 20mA$) although very thin films are more prone to breaking at high temperatures increase due to the fact that the network only carries a limited number of conductive paths. In the future, this plot will permit us to tune silver nanowire networks to the right thickness in order to obtain the desired saturation temperature for a certain applied current. This study shows that the heat dissipation mechanism for TFHs made from one dimensional nanomaterials can be easily explained from first principles. More importantly, this study shows that TFHs made from nanowires can be produced only using a minimal amount of materials which would lower their cost dramatically, since very transparent network yield the highest temperatures (with temperature increasing most rapidly in the percolation regime).

8.2 FUTURE WORK: IMPEDANCE STUDY OF NETWORKS OF 1D NANOMATERIALS

The study of the properties of silver nanowire networks in Chapter 5 showed that in order to obtain state of the art networks, polymer leftover from nanowire synthesis had to be removed from the networks to increase its opto-electrical properties. Indeed, in some cases, the presence of the polymer (usually PVP) caused the networks to be infinitely resistive. Although this in a huge inconvenience in the area of TCs, it has great advantages in the field of switches where the possibility of having a network, or part thereof, in an "on" or "off" state would be very useful. Some work has already been done on characterising this phenomenon. Nirmalraj et al.[168] have shown that by spray-depositing silver nanowires onto gold electrodes with a separation of about 1mm, "on" switching those devices could be imaged via conductive AFM as shown in Figure 8.1. In order to understand the switching mechanism of the networks, they applied a voltage to a range of networks with different nanowire densities and electrode separations. They were able to show that the relationship between the threshold voltage (at which the network switches on) and the network density follows a power law

$$V_{Th} = \left(\frac{N}{A}\right)^{n} \tag{8.2}$$

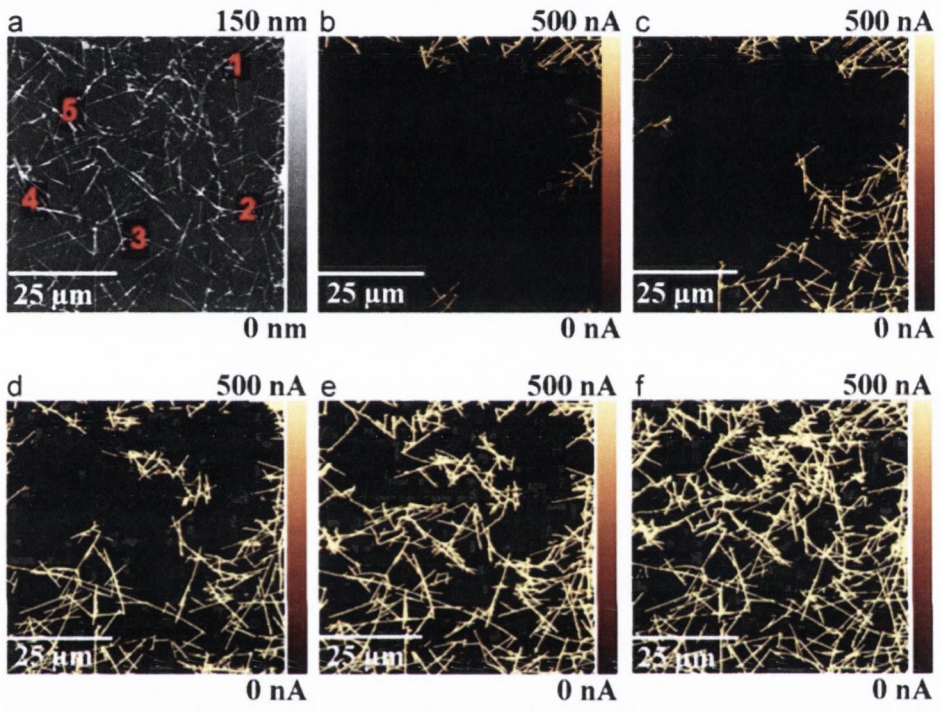

Figure 8.1: (a) Topography of a random network of Ag nanowires. The metal coated AFM tip was used to locally activate sites in the network by applying a voltage pulse of 6 V for $\sim$ 2*s* and then imaging the same network region under a lower bias of *200 mV*. The current maps shown in b–f are a result of applying the voltage pulses at selected regions marked *1-5* on the topographic map. The network can be seen to turn on locally as the wires become connected to each other and to the electrode following local probe excitation. Note: the electrode is located at the top of the image.

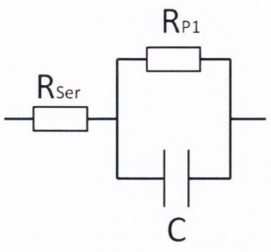

Figure 8.2: Equivalent circuit for a silver nanowire network as seen through impedance spectroscopy.

where n is a function of electrode separation and increases sharply from -1 for small electrode separation to -0.5 for larger tip-electrode separations. However, a major part of the mechanism eluded them as they were unable to see the effect of the creation of the conducting paths other than optically. Indeed, until full paths are formed between the electrodes it is impossible to measure a current carrying information about the network. However, this problem can be avoided by applying an AC voltage to the network in addition to the base DC voltage and measuring the current response using impedance spectroscopy. In this case, even in the presence of an "open-network", the effects of the changes in the network morphology can be recorder. We have done some preliminary work using this technique which was found to be very promising. Figure 8.3 shows the change in series resistance, parallel resistance and capacitance (extracted from the impedance spectroscopy data) as a function of the DC voltage applied. This data shows that until $3V$ is applied, the network shows no parallel resistance and exhibits the behaviour of a series RC circuit in agreement with a circuit which is switched off. Once a channel is created between the electrodes, a parallel resistance appears as shown in Figure 8.2. However, it must be noted that the values for the resistances and capacitance do not correspond to properties of the physical system. Indeed, impedance spectroscopy can only measure the values for the impedance of the "effective" equivalent circuit components. This is where lies this project's main challenge: understanding the mechanism of network switching via information about an imaginary equivalent circuit which morphs as voltage is varied and as time goes by...

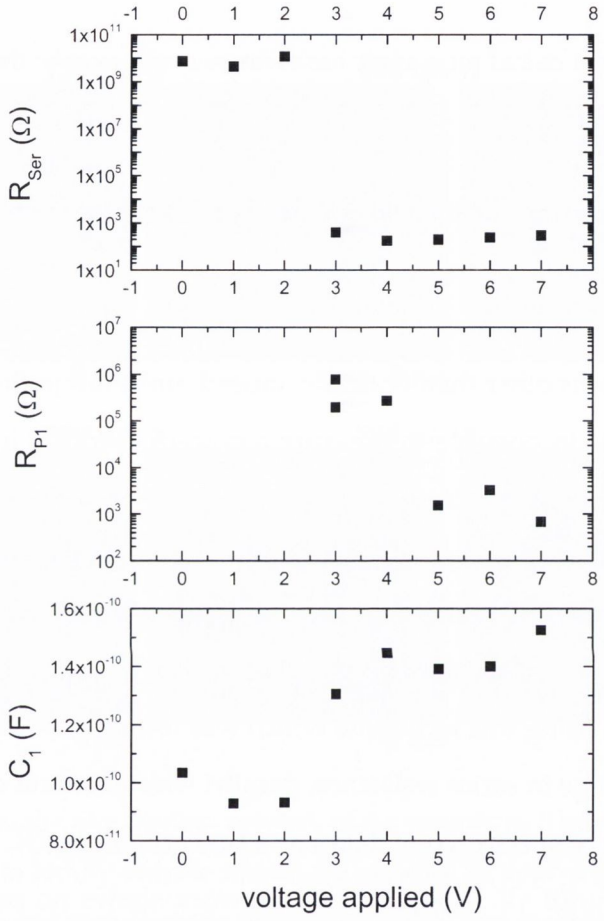

Figure 8.3: DC voltage is applied to the sample for a set time and impedance measured after each voltage change. The series and parallel resistance and the capacitance are represented in Figure 8.2. This data shows that at $3V$, a parallel resistance appears and the values for both series resistance and capacitance changes. The challenge will be to match the impedance description of the system to the actual physical system.

BIBLIOGRAPHY

[1] Chen, Z., Cotterell, B., and Wang, W. (2002) The fracture of brittle thin films on compliant substrates in flexible displays. *Engineering Fracture Mechanics 69*, 597 – 603.

[2] Wu, J., Zang, J., Rathmell, A. R., Zhao, X., and Wiley, B. J. (2013) Reversible Sliding in Networks of Nanowires. *Nano Letters 0*, null.

[3] Lipomi, D. J., Vosgueritchian, M., Tee, B. C.-K., Hellstrom, S. L., Lee, J. A., Fox, C. H., and Bao, Z. (2011) Skin-like pressure and strain sensors based on transparent elastic films of carbon nanotubes. *Nat Nano 6*, 788–792.

[4] Kang, T. J., Kim, T., Seo, S. M., Park, Y. J., and Kim, Y. H. (2011) Thickness-dependent thermal resistance of a transparent glass heater with a single-walled carbon nanotube coating. *Carbon 49*, 1087 – 1093.

[5] Kang, T. J., Kim, T., Seo, S. M., Park, Y. J., and Kim, Y. H. (2011) Thickness-dependent thermal resistance of a transparent glass heater with a single-walled carbon nanotube coating. *Carbon 49*, 1087 – 1093.

[6] Yoon, Y.-H., Song, J.-W., Kim, D., Kim, J., Park, J.-K., Oh, S.-K., and Han, C.-S. (2007) Transparent Film Heater Using Single-Walled Carbon Nanotubes. *Advanced Materials 19*, 4284–4287.

[7] Celle, C., Mayousse, C., Moreau, E., Basti, H., Carella, A., and Simonato, J.-P. (2012) Highly flexible transparent film heaters based on random networks of silver nanowires. *Nano Research 5*, 427–433.

[8] Kang, J., Kim, H., Kim, K. S., Lee, S.-K., Bae, S., Ahn, J.-H., Kim, Y.-J., Choi, J.-B., and Hong, B. H. (2011) High-Performance Graphene-Based Transparent Flexible Heaters. *Nano Letters 11*, 5154–5158.

[9] Gordon, R. G. (2000) Criteria for Choosing Transparent Conductors. *MRS Bulletin 25*, 52–57.

[10] McMillan, J. A., and Peterson, E. M. (1979) Kinetics of decomposition of amorphous hydrogenated silicon films. *Journal of Applied Physics 50*, 5238–5241.

[11] Lewis, B. G., and Paine, D. C. (2000) Applications and Processing of Transparent Conducting Oxides. *MRS Bulletin 25*, 22–27.

[12] Hartnagel, H., Dawar, A., Jain, A., and Jagadish, C. In *Semiconducting Thin Films*; Jain, S., Ed.; Institute of Physics Publishing, 1195.

[13] Lampert, C. (2003) Large-area smart glass and integrated photovoltaics. *Solar Energy Materials and Solar Cells 76*, 489 – 499, <ce:title>Photovoltaics and photoactive materials - properties, technology and applications</ce:title>.

[14] Tak, Y.-H., Kim, K.-B., Park, H.-G., Lee, K.-H., and Lee, J.-R. (2002) Criteria for ITO (indium tin-oxide) thin film as the bottom electrode of an organic light emitting diode. *Thin Solid Films 411*, 12 – 16.

[15] Rowell, M. W., and McGehee, M. D. (2011) Transparent electrode requirements for thin film solar cell modules. *Energy Environ. Sci. 4*, 131–134.

[16] Leem, D.-S., Edwards, A., Faist, M., Nelson, J., Bradley, D. D. C., and de Mello, J. C. (2011) Efficient Organic Solar Cells with Solution-Processed Silver Nanowire Electrodes. *Advanced Materials 23*, 4371–4375.

[17] Granqvist, C., and Hultker, A. (2002) Transparent and conducting ITO films: new developments and applications. *Thin Solid Films 411*, 1 – 5.

[18] Christian, K., and Shatynski, S. (1983) Thin film passive solar windows produced by reactive evaporation of In-Sn. *Thin Solid Films 108*, 319 – 324.

[19] Yao, J., Hao, S., and Wilkinson, J. (1990) Indium tin oxide films by sequential evaporation. *Thin Solid Films 189*, 227 – 233.

[20] Ryabova, L., Salun, V., and Serbinov, I. (1982) Transparent conductive films of In2O3:Sn prepared by the pyrolysis method. *Thin Solid Films 92*, 327 – 332.

[21] Lin, H., Yu, J., Wang, N., Lou, S., and Jiang, Y. (2009) Fabrication and Properties of DC Magnetron Sputtered Indium Tin Oxide on Flexible Plastic Substrate. *Journal of Materials Sciences and Technology 25*, 119.

[22] Fujinaka, M., and Berezin, A. (1983) Tin-doped In2O3 films deposited by r.f. sputtering. *Thin Solid Films 101*, 7 – 10.

[23] Cairns, D. R., Witte, R. P., Sparacin, D. K., Sachsman, S. M., Paine, D. C., Crawford, G. P., and Newton, R. R. (2000) Strain-dependent electrical resistance of tin-doped indium oxide on polymer substrates. *Applied Physics Letters 76*, 1425–1427.

[24] Leterrier, Y., Madico, L., Demarco, F., Manson, J.-A., Betz, U., EscolaÊ, M., Olsson, M. K., and Atamny, F. (2004) Mechanical integrity of transparent conductive oxide films for flexible polymer-based displays. *Thin Solid Films 460*, 156 – 166.

[25] 2013; http://www.nitto.com/product/datasheet/optical/009/.

[26] Kim, H., Horwitz, J. S., Kushto, G. P., Kafafi, Z. H., and Chrisey, D. B. (2001) Indium tin oxide thin films grown on flexible plastic substrates by pulsed-laser deposition for organic light-emitting diodes. *Applied Physics Letters 79*, 284 – 286.

[27] Shirakawa, H., Louis, E. J., MacDiarmid, A. G., Chiang, C. K., and Heeger, A. J. (1977) Synthesis of electrically conducting organic polymers: halogen derivatives of polyacetylene, (CH). *J. Chem. Soc., Chem. Commun. 0*, 578–580.

[28] Groenendaal, L., Jonas, F., Freitag, D., Pielartzik, H., and Reynolds, J. R. (2000) Poly(3,4-ethylenedioxythiophene) and Its Derivatives: Past, Present, and Future. *Advanced Materials 12*, 481–494.

[29] Hu, L., Li, J., Liu, J., Gruner, G., and Marks, T. (2010) Flexible organic light-emitting diodes with transparent carbon nanotube electrodes: problems and solutions. *Nanotechnology 21*, 155202.

[30] Hu, L., Kim, H. S., Lee, J.-Y., Peumans, P., and Cui, Y. (2010) Scalable Coating and Properties of Transparent, Flexible, Silver Nanowire Electrodes. *ACS Nano 4*, 2955–2963, PMID: 20426409.

[31] Lee, J.-Y., Connor, S. T., Cui, Y., and Peumans, P. (2008) Solution-Processed Metal Nanowire Mesh Transparent Electrodes. *Nano Letters 8*, 689–692, PMID: 18189445.

[32] De, S., Higgins, T. M., Lyons, P. E., Doherty, E. M., Nirmalraj, P. N., Blau, W. J., Boland, J. J., and Coleman, J. N. (2009) Silver Nanowire Networks as Flexible, Transparent, Conducting Films: Extremely High DC to Optical Conductivity Ratios. *ACS Nano 3*, 1767–1774.

[33] Scardaci, V., Coull, R., Lyons, P. E., Rickard, D., and Coleman, J. N. (2011) Spray Deposition of Highly Transparent, Low-Resistance Networks of Silver Nanowires over Large Areas. *Small 7*, 2621–2628.

[34] Wu, H., Hu, L., Rowell, M. W., Kong, D., Cha, J. J., McDonough, J. R., Zhu, J., Yang, Y., McGehee, M. D., and Cui, Y. (2010) Electrospun Metal Nanofiber Webs as High-Performance Transparent Electrode. *Nano Letters 10*, 4242–4248.

[35] Lyons, P. E., De, S., Elias, J., Schamel, M., Philippe, L., Bellew, A. T., Boland, J. J., and Coleman, J. N. (2011) High-Performance Transparent Conductors from Networks of Gold Nanowires. *The Journal of Physical Chemistry Letters 2*, 3058–3062.

[36] Koleonik, M. M., Hansel, S., Lutz, T., Kinahan, N., Boese, M., and Krstic, V. (2011) Resolving In Situ Specific-Contact, Current-Crowding, and Channel Resistivity in Nanowire Devices: A Case Study with Silver Nanowires. *Small 7*, 2873–2877.

[37] Lagos, M. J., Autreto, P. A. S., Galvao, D. S., and Ugarte, D. (2012) Correlation between quantum conductance and atomic arrangement of atomic-size silver nanowires. *Journal of Applied Physics 111*, 124316.

[38] Zhao, J., Buia, C., Han, J., and Lu, J. P. (2003) Quantum transport properties of ultrathin silver nanowires. *Nanotechnology 14*, 501.

[39] Link, S., Mohamed, M. B., and El-Sayed, M. A. (1999) Simulation of the Optical Absorption Spectra of Gold Nanorods as a Function of Their Aspect Ratio and the Effect of the Medium Dielectric Constant. *The Journal of Physical Chemistry B 103*, 3073–3077.

[40] Kline, T. R., Tian, M., Wang, J., Sen, A., Chan, M. W. H., and Mallouk, T. E. (2006) Template-Grown Metal Nanowires. *Inorganic Chemistry 45*, 7555–7565.

[41] Xia, Y., Yang, P., Sun, Y., Wu, Y., Mayers, B., Gates, B., Yin, Y., Kim, F., and Yan, H. (2003) One-Dimensional Nanostructures: Synthesis, Characterization, and Applications. *Advanced Materials 15*, 353–389.

[42] Sun, Y., Gates, B., Mayers, B., and Xia, Y. (2002) Crystalline Silver Nanowires by Soft Solution Processing. *Nano Letters 2*, 165–168.

[43] Sun, Y., Yin, Y., Mayers, B. T., Herricks, T., and Xia, Y. (2002) Uniform Silver Nanowires Synthesis by Reducing $AgNO_3$ with Ethylene Glycol in the Presence of Seeds and PVP. *Chemistry of Materials 14*, 4736–4745.

[44] Allpress, J., and Sanders, J. (1967) The structure and orientation of crystals in deposits of metals on mica. *Surface Science 7*, 1 – 25.

[45] Wang, D., Dimonie, V. L., Sudol, E. D., and El-Aasser, M. S. (2002) Effect of PVP in dispersion and seeded dispersion polymerizations. *Journal of Applied Polymer Science 84*, 2721–2732.

[46] Huang, H. H., Ni, X. P., Loy, G. L., Chew, C. H., Tan, K. L., Loh, F. C., Deng, J. F., and Xu, G. Q. (1996) Photochemical Formation of Silver Nanoparticles in Poly-N-vinylpyrrolidone. *Langmuir 12*, 909–912.

[47] Johnson, C. J., Dujardin, E., Davis, S. A., Murphy, C. J., and Mann, S. (2002) Growth and form of gold nanorods prepared by seed-mediated, surfactant-directed synthesis. *J. Mater. Chem. 12*, 1765–1770.

[48] Sun, Y., Mayers, B., Herricks, T., and Xia, Y. (2003) Polyol Synthesis of Uniform Silver Nanowires:A Plausible Growth Mechanism and the Supporting Evidence. *Nano Letters 3*, 955–960.

[49] Giersig, M., Pastoriza-Santos, I., and Liz-Marzan, L. M. (2004) Evidence of an aggregative mechanism during the formation of silver nanowires in N,N-dimethylformamide. *J. Mater. Chem. 14*, 607–610.

[50] Hsieh, D.-Y., and Plesset, M. S. (1961) Theory of Rectified Diffusion of Mass into Gas Bubbles. *The Journal of the Acoustical Society of America 33*, 206–215.

[51] Fyrillas, M. M., and Szeri, A. J. (1994) Dissolution or growth of soluble spherical oscillating bubbles. *Journal of Fluid Mechanics 277*, 381–407.

[52] Lee, J., Kentish, S., and Ashokkumar, M. (2005) Effect of Surfactants on the Rate of Growth of an Air Bubble by Rectified Diffusion. *The Journal of Physical Chemistry B 109*, 14595–14598.

[53] Hennrich, F., Krupke, R., Arnold, K., Rojas Stutz, J. A., Lebedkin, S., Koch, T., Schimmel, T., and Kappes, M. M. (2007) The Mechanism of Cavitation-Induced Scission of Single-Walled Carbon Nanotubes. *The Journal of Physical Chemistry B 111*, 1932–1937.

[54] Lucas, A., Zakri, C., Maugey, M., Pasquali, M., Schoot, P. v. d., and Poulin, P. (2009) Kinetics of Nanotube and Microfiber Scission under Sonication. *The Journal of Physical Chemistry C 113*, 20599–20605.

[55] Kuijpers, M. W., Iedema, P. D., Kemmere, M. F., and Keurentjes, J. T. (2004) The mechanism of cavitation-induced polymer scission; experimental and computational verification. *Polymer 45*, 6461 – 6467.

[56] Jones, S., Evans, G., and Galvin, K. (1999) Bubble nucleation from gas cavities - a review. *Advances in Colloid and Interface Science 80*, 27 – 50.

[57] Sepulveda-Mora, S., and Cloutier, S. (2012) Figures of Merit for High-Performance Transparent Electrodes Using Dip-Coated Silver Nanowire Networks. *Journal of Nanomaterials 1*, 1–7.

[58] Madaria, A., Kumar, A., Ishikawa, F., and Zhou, C. (2010) Uniform, highly conductive, and patterned transparent films of a percolating silver nanowire network on rigid and flexible substrates using a dry transfer technique. *Nano Research 3*, 564–573.

[59] Hines, D. R., Mezhenny, S., Breban, M., Williams, E. D., Ballarotto, V. W., Esen, G., Southard, A., and Fuhrer, M. S. (2005) Nanotransfer printing of organic and

carbon nanotube thin-film transistors on plastic substrates. *Applied Physics Letters 86*, 163101.

[60] Wu, Z., Chen, Z., Du, X., Logan, J. M., Sippel, J., Nikolou, M., Kamaras, K., Reynolds, J. R., Tanner, D. B., Hebard, A. F., and Rinzler, A. G. (2004) Transparent, Conductive Carbon Nanotube Films. *Science 305*, 1273–1276.

[61] Hu, L., Hecht, D. S., and Gruner, G. (2004) Percolation in Transparent and Conducting Carbon Nanotube Networks. *Nano Letters 4*, 2513–2517.

[62] De, S., Lyons, P. E., Sorel, S., Doherty, E. M., King, P. J., Blau, W. J., Nirmalraj, P. N., Boland, J. J., Scardaci, V., Joimel, J., and Coleman, J. N. (2009) Transparent, Flexible, and Highly Conductive Thin Films Based on Polymer Nanotube Composites. *ACS Nano 3*, 714–720.

[63] Wang, Y., Feng, T., Wang, K., Chen, M. Q. Y., and Sun, Z. (2011) A Facile Method for Preparing Transparent, Conductive, and Paper-Like Silver Nanowire Films. *Journal of Nanomaterials 2011*, 1–5.

[64] Scardaci, V., Coull, R., and Coleman, J. N. (2010) Very thin transparent, conductive carbon nanotube films on flexible substrates. *Applied Physics Letters 97*, 023114.

[65] Shen, X., Ho, C.-M., and Wong, T.-S. (2010) Minimal Size of Coffee Ring Structure. *The Journal of Physical Chemistry B 114*, 5269–5274, PMID: 20353247.

[66] Deegan, R. D., Bakajin, O., Dupont, T. F., Huber, G., Nagel, S. R., and Witten, T. A. (2000) Contact line deposits in an evaporating drop. *Phys. Rev. E 62*, 756–765.

[67] Deegan, R. D., Bakajin, O., Dupont, T. F., Huber, G., Nagel, S. R., and Witten, T. A. (1997) Capillary flow as the cause of ring stains from dried liquid drops. *Nature 389*, 827– 829.

[68] Pereira, L. F. C., Rocha, C. G., Latge, A., and Ferreira, M. S. (2010) A computationally efficient method for calculating the maximum conductance of disordered networks: Application to one-dimensional conductors. *Journal of Applied Physics 108*, 103720.

[69] van de Groep, J., Spinelli, P., and Polman, A. (2012) Transparent Conducting Silver Nanowire Networks. *Nano Letters 12*, 3138–3144.

[70] Lyons, P. E., De, S., Blighe, F., Nicolosi, V., Pereira, L. F. C., Ferreira, M. S., and Coleman, J. N. (2008) The relationship between network morphology and conductivity in nanotube films. *Journal of Applied Physics 104*, 044302.

[71] Behnam, A., and Ural, A. (2007) Computational study of geometry-dependent resistivity scaling in single-walled carbon nanotube films. *Phys. Rev. B 75*, 125432.

[72] Pike, G. E., and Seager, C. H. (1974) Percolation and conductivity: A computer study. I. *Phys. Rev. B 10*, 1421–1434.

[73] Seager, C. H., and Pike, G. E. (1974) Percolation and conductivity: A computer study. II. *Phys. Rev. B 10*, 1435–1446.

[74] Balberg, I., Binenbaum, N., and Anderson, C. H. (1983) Critical Behavior of the Two-Dimensional Sticks System. *Phys. Rev. Lett. 51*, 1605–1608.

[75] Garnett, E., McGehee, M., and Brongersma, M. (2012) Self-limited plasmonic welding of silver nanowire junctions. *Nat Mater 11*, 1476–1122.

[76] Lu, Y., Huang, J. Y., Wang, C., Sun, S., and Lou, J. (2005) Cold welding of ultrathin gold nanowires. *Nat Nano 5*, 218–224.

[77] Zhu, R., Chung, C.-H., Cha, K. C., Yang, W., Zheng, Y. B., Zhou, H., Song, T.-B., Chen, C.-C., Weiss, P. S., Li, G., and Yang, Y. (2011) Fused Silver Nanowires with Metal Oxide Nanoparticles and Organic Polymers for Highly Transparent Conductors. *ACS Nano 5*, 9877–9882.

[78] Hecht, D. S., Hu, L., and Irvin, G. (2011) Emerging Transparent Electrodes Based on Thin Films of Carbon Nanotubes, Graphene, and Metallic Nanostructures. *Advanced Materials 23*, 1482–1513.

[79] De, S., King, P. J., Lyons, P. E., Khan, U., and Coleman, J. N. (2010) Size Effects and the Problem with Percolation in Nanostructured Transparent Conductors. *ACS Nano 4*, 7064–7072.

[80] Balberg, I. (1987) Tunneling and nonuniversal conductivity in composite materials. *Phys. Rev. Lett. 59*, 1305–1308.

[81] Grimaldi, C., and Balberg, I. (2006) Tunneling and Nonuniversality in Continuum Percolation Systems. *Phys. Rev. Lett. 96*, 066602.

[82] 2013; http://www.mit.edu/~levitov/8.334/notes/percol_notes.pdf.

[83] Stauffer, D., and Aharony, A. In *Introduction to percolation Theory*; Francis, T. ., Ed.; Taylor & Francis, 1982.

[84] Balberg, I. (1998) Limits on the continuum-percolation transport exponents. *Phys. Rev. B 57*, 13351–13354.

[85] Johner, N., Grimaldi, C., Balberg, I., and Ryser, P. (2008) Transport exponent in a three-dimensional continuum tunneling-percolation model. *Phys. Rev. B 77*, 174204.

[86] Iijima, S. (1991) Helical microtubules of graphitic carbon. *Nature 354*, 56–58.

[87] Nirmalraj, P. N., Lyons, P. E., De, S., Coleman, J. N., and Boland, J. J. (2009) Electrical Connectivity in Single-Walled Carbon Nanotube Networks. *Nano Letters 9*, 3890–3895, PMID: 19775126.

[88] Dai, H. (2002) Carbon Nanotubes:Synthesis, Integration and Properties. *Accounts of Chemical Research 35*, 1035-1044, PMID: 12484791.

[89] Durkop, T., Getty, S. A., Cobas, E., and Fuhrer, M. S. (2004) Extraordinary Mobility in Semiconducting Carbon Nanotubes. *Nano Letters 4*, 35–39.

[90] Odom, T. W., Huang, J.-L., Kim, P., and Lieber, C. M. (2000) Structure and Electronic Properties of Carbon Nanotubes. *The Journal of Physical Chemistry B 104*, 2794–2809.

[91] Treacy, M., W., E. T., and Gibson, J. M. (1996) Exceptionally high Young's modulus observed for individual carbon nanotubes. *Nature 381*, 678–680.

[92] Coleman, J., Khan, U., and Gunko, Y. (2006) Mechanical Reinforcement of Polymers Using Carbon Nanotubes. *Advanced Materials 18*, 689–706.

[93] Yu, M.-F., Lourie, O., Dyer, M. J., Moloni, K., Kelly, T. F., and Ruoff, R. S. (2000) Strength and Breaking Mechanism of Multiwalled Carbon Nanotubes Under Tensile Load. *Science 287*, 637–640.

[94] Rowell, M. W., Topinka, M. A., McGehee, M. D., Prall, H.-J., Dennler, G., Sariciftci, N. S., Hu, L., and Gruner, G. (2006) Organic solar cells with carbon nanotube network electrodes. *Applied Physics Letters 88*, 233506.

[95] King, P. J., Higgins, T. M., De, S., Nicoloso, N., and Coleman, J. N. (2012) Percolation Effects in Supercapacitors with Thin, Transparent Carbon Nanotube Electrodes. *ACS Nano 6*, 1732–1741.

[96] Merkossi, A., Pumera, M., Llopis, X., Perez, B., del Valle, M., and Alegret, S. (2005) New materials for electrochemical sensing VI: Carbon nanotubes. *TrAC Trends in Analytical Chemistry 24*, 826 – 838.

[97] Iijima, S. (1993) Single-shell carbon nanotubes of 1-nm diameter. *Nature 363*, 603–605.

[98] Odom, T. W., Huang, J.-L., Kim, P., and Lieber, C. M. (1998) Atomic structure and electronic properties of single-walled carbon nanotubes. *Nature 391*, 62–64.

[99] Ouyang, M., Huang, J.-L., Cheung, C. L., and Lieber, C. M. (2001) Energy Gaps in Metallic Single-Walled Carbon Nanotubes. *Science 292*, 702–705.

[100] Kane, C. L., and Mele, E. J. (1997) Size, Shape, and Low Energy Electronic Structure of Carbon Nanotubes. *Phys. Rev. Lett. 78*, 1932–1935.

[101] Mintmire, J. W., and White, C. T. (1998) Universal Density of States for Carbon Nanotubes. *Phys. Rev. Lett. 81*, 2506–2509.

[102] Ding, J. W., Yan, X. H., and Cao, J. X. (2002) Analytical relation of band gaps to both chirality and diameter of single-wall carbon nanotubes. *Phys. Rev. B 66*, 073401.

[103] Kumar, M., and Ando, Y. (2010) Chemical Vapor Deposition of Carbon Nanotubes: A Review on Growth Mechanism and Mass Production. *Journal of Nanoscience and Nanotechnology 10*, 3739–3758(20).

[104] Naha, S., and Puri, I. K. (2008) A model for catalytic growth of carbon nanotubes. *Journal of Physics D: Applied Physics 41*, 065304.

[105] Ebbesen, T. W., and Ajayan, P. M. (1992) Large-scale synthesis of carbon nanotubes. *Nature 358*, 220–222.

[106] Prasek, J., Drbohlavova, J., Chomoucka, J., Hubalek, J., Jasek, O., Adam, V., and Kizek, R. (2011) Methods for carbon nanotubes synthesis-review. *J. Mater. Chem. 21*, 15872–15884.

[107] Guo, T., Nikolaev, P., Thess, A., Colbert, D., and Smalley, R. (1995) Catalytic growth of single-walled manotubes by laser vaporization. *Chemical Physics Letters 243*, 49–54.

[108] Kruusenberg, I., Alexeyeva, N., Tammeveski, K., Kozlova, J., Matisen, L., Sammelselg, V., Solla-Gullon, J., and Feliu, J. (2011) Effect of purification of carbon nanotubes on their electrocatalytic properties for oxygen reduction in acid solution. *Carbon 49*, 4031 – 4039.

[109] Sun, Z., Nicolosi, V., Rickard, D., Bergin, S. D., Aherne, D., and Coleman, J. N. (2008) Quantitative Evaluation of Surfactant-stabilized Single-walled Carbon Nanotubes: Dispersion Quality and Its Correlation with Zeta Potential. *The Journal of Physical Chemistry C 112*, 10692–10699.

[110] Coleman, J. N. (2009) Liquid-Phase Exfoliation of Nanotubes and Graphene. *Advanced Functional Materials 19*, 3680–3695.

[111] Yurekli, K., Mitchell, C. A., and Krishnamoorti, R. (2004) Small-Angle Neutron Scattering from Surfactant-Assisted Aqueous Dispersions of Carbon Nanotubes. *Journal of the American Chemical Society 126*, 9902–9903.

[112] Vaisman, L. (2006) The role of surfactants in dispersions of carbon nanotubes. *Advances in colloid and interface science 128-130*, 37–46.

[113] Arnold, M., Green, A., Hulvat, J., Stupp, S., and Hersam, M. (2006) Sorting carbon nanotubes by electronic structure using density differentiation. *Nat Nano 1*, 60–65.

[114] Hecht, D., Hu, L., and Gruner, G. (2006) Conductivity scaling with bundle length and diameter in single walled carbon nanotube networks. *Applied Physics Letters 89*, 133112.

[115] Lyons, P. E., De, S., Blighe, F., Nicolosi, V., Pereira, L. F. C., Ferreira, M., and Coleman, J. (2008) The relationship between network morphology and conductivity in nanotube films. *Journal of Applied Physics 104*, 044302–044302–8.

[116] Stadermann, M., Grube, H., Boland, J. J., Papadakis, S. J., Falvo, M. R., Superfine, R., and Washburn, S. (2003) Simultaneous atomic force microscopy measurement of topography and contact resistance of metal films and carbon nanotubes. *Review of Scientific Instruments 74*, 3653–3655.

[117] Stadermann, M., Papadakis, S. J., Falvo, M. R., Fu, Q., Liu, J., Fridman, Y., Boland, J. J., Superfine, R., and Washburn, S. (2005) Exponential decay of local conductance in single-wall carbon nanotubes. *Phys. Rev. B 72*, 245406.

[118] Stadermann, M., Papadakis, S. J., Falvo, M. R., Novak, J., Snow, E., Fu, Q., Liu, J., Fridman, Y., Boland, J. J., Superfine, R., and Washburn, S. (2004) Nanoscale study of conduction through carbon nanotube networks. *Phys. Rev. B 69*, 201402.

[119] Prior, M., Makarovski, A., and Finkelstein, G. (2007) Low-temperature conductive tip atomic force microscope for carbon nanotube probing and manipulation. *Applied Physics Letters 91*, 053112.

[120] Lee, H., Chang, S., and Yoon, E. (2006) A Flexible Polymer Tactile Sensor: Fabrication and Modular Expandability for Large Area Deployment. *Microelectromechanical Systems, Journal of 15*, 1681–1686.

[121] Kim, H., Lee, S., Han, J., Kim, T., Hwang, S., Ahn, S., You, I., Cho, K., Song, T., and Yun, K. (2009) Transparent and flexible tactile sensor for multi touch screen

application with force sensing. *Solid-State Sensors, Actuators and Microsystems Conference, 2009. TRANSDUCERS 2009. International 1*, 1146–1149.

[122] Ishihara, T., and Matsubara, S. (1998) Capacitive Type Gas Sensors. *Journal of Electroceramics 2*, 215–228.

[123] Quartarone, E., Mustarelli, P., Magistris, A., Russo, M., Fratoddi, I., and Furlani, A. (2000) Investigations by impedance spectroscopy on the behaviour of poly(N,N-dimethylpropargylamine) as humidity sensor. *Solid State Ionics 136*, 667–670.

[124] Schubert, P., and Nevin, J. (1985) A polyimide-based capacitive humidity sensor. *Electron Devices, IEEE Transactions on 32*, 1220–1223.

[125] Yeow, J. T. W., and She, J. P. M. (2006) Carbon nanotube-enhanced capillary condensation for a capacitive humidity sensor. *Nanotechnology 17*, 5441.

[126] Kang, U., and Wise, K. (2000) A high-speed capacitive humidity sensor with on-chip thermal reset. *Electron Devices, IEEE Transactions on 47*, 702–710.

[127] 2013; http://northeastflex.com/transparent-heaters/.

[128] 2013; http://www.vartechsystems.com/products/Transparent-Heaters.asp.

[129] Khaligh, H., and Goldthorpe, I. (2013) Failure of silver nanowire transparent electrodes under current flow. *Nanoscale Research Letters 8*, 235.

[130] Pop, E., Mann, D., Wang, Q., Goodson, K., and Dai, H. (2006) Thermal Conductance of an Individual Single-Wall Carbon Nanotube above Room Temperature. *Nano Letters 6*, 96–100.

[131] Wu, Z. P., and Wang, J. N. (2009) Preparation of large-area double-walled carbon nanotube films and application as film heater. *Physica E: Low-dimensional Systems and Nanostructures 42*, 77 – 81.

[132] Begtrup, G. E., Ray, K. G., Kessler, B. M., Yuzvinsky, T. D., Garcia, H., and Zettl, A. (2007) Probing Nanoscale Solids at Thermal Extremes. *Phys. Rev. Lett. 99*, 155901.

[133] Yang, Z.-P., Ci, L., Bur, J. A., Lin, S.-Y., and Ajayan, P. M. (2008) Experimental Observation of an Extremely Dark Material Made By a Low-Density Nanotube Array. *Nano Letters 8*, 446–451, PMID: 18181658.

[134] Jang, H.-S., Jeon, S. K., and Nahm, S. H. (2011) The manufacture of a transparent film heater by spinning multi-walled carbon nanotubes. *Carbon 49*, 111 – 116.

[135] Balandin, A. A., Ghosh, S., Bao, W., Calizo, I., Teweldebrhan, D., Miao, F., and Lau, C. N. (2008) Superior Thermal Conductivity of Single-Layer Graphene. *Nano Letters 8*, 902–907, PMID: 18284217.

[136] Seol, J. H., Jo, I., Moore, A. L., Lindsay, L., Aitken, Z. H., Pettes, M. T., Li, X., Yao, Z., Huang, R., Broido, D., Mingo, N., Ruoff, R. S., and Shi, L. (2010) Two-Dimensional Phonon Transport in Supported Graphene. *Science 328*, 213–216.

[137] Balandin, A. A. (2011) Thermal properties of graphene and nanostructured carbon materials. *Nat Mater 10*, 569–581.

[138] Cai, W., Moore, A. L., Zhu, Y., Li, X., Chen, S., Shi, L., and Ruoff, R. S. (2010) Thermal Transport in Suspended and Supported Monolayer Graphene Grown by Chemical Vapor Deposition. *Nano Letters 10*, 1645–1651.

[139] Bae, J. J., Lim, S. C., Han, G. H., Jo, Y. W., Doung, D. L., Kim, E. S., Chae, S. J., Huy, T. Q., Van Luan, N., and Lee, Y. H. (2012) Heat Dissipation of Transparent Graphene Defoggers. *Advanced Functional Materials 22*, 4819–4826.

[140] Kim, T., Kim, Y. W., Lee, H. S., Kim, H., Yang, W. S., and Suh, K. S. (2013) Uniformly Interconnected Silver-Nanowire Networks for Transparent Film Heaters. *Advanced Functional Materials 23*, 1250–1255.

[141] Janas, D., and Koziol, K. K. (2013) Rapid electrothermal response of high-temperature carbon nanotube film heaters. *Carbon 59*, 457 – 463.

[142] Kittel, C. In *Introduction to solid state physics*; McFadden, P., Ed.; Wiley & sons, 2005.

[143] Dressel, M., and Gruner, G. In *Electrodynamics of solids-optical properties of electrons in matter*; press, C. U., Ed.; Cambridge University press, 2002.

[144] Solomon, S., Weisbuch, G., de Arcangelis, L., Jan, N., and Stauffer, D. (2000) Social percolation models. *Physica A: Statistical Mechanics and its Applications 277*, 239 – 247.

[145] Moore, C., and Newman, M. E. J. (2000) Exact solution of site and bond percolation on small-world networks. *Phys. Rev. E 62*, 7059–7064.

[146] Stanley, H. E. (1977) Cluster shapes at the percolation threshold: and effective cluster dimensionality and its connection with critical-point exponents. *Journal of Physics A: Mathematical and General 10*, L211.

[147] Fletcher, T. H., Kerstein, A. R., Pugmire, R. J., Solum, M. S., and Grant, D. M. (1992) Chemical percolation model for devolatilization. Direct use of carbon-13 NMR data to predict effects of coal type. *Energy & Fuels 6*, 414–431.

[148] Moore, C., and Newman, M. E. J. (2000) Epidemics and percolation in small-world networks. *Phys. Rev. E 61*, 5678–5682.

[149] Newman, M. E. J., Jensen, I., and Ziff, R. M. (2002) Percolation and epidemics in a two-dimensional small world. *Phys. Rev. E 65*, 021904.

[150] Sander, L., Warren, C., Sokolov, I., Simon, C., and Koopman, J. (2002) Percolation on heterogeneous networks as a model for epidemics. *Mathematical Biosciences 180*, 293 – 305.

[151] Sorel, S., Lyons, P. E., De, S., Dickerson, J. C., and Coleman, J. N. (2012) The dependence of the optoelectrical properties of silver nanowire networks on nanowire length and diameter. *Nanotechnology 23*, 185201.

[152] Hecht, D. S., Hu, L., and Irvin, G. (2011) Emerging Transparent Electrodes Based on Thin Films of Carbon Nanotubes, Graphene, and Metallic Nanostructures. *Advanced Materials 23*, 1482–1513.

[153] Robert J. Young, P. P. A. L. *Introduction to polymers*; Nelson Thornes Limited, 1991.

[154] Hansen, C. M. In *Hansen Solubility Parameters: A UserÕs Handbook*; Raton, B., Ed.; CRC Press, 2007.

[155] 2013; www.seashelltech.com.

[156] Doherty, E. M., De, S., Lyons, P. E., Shmeliov, A., Nirmalraj, P. N., Scardaci, V., Joimel, J., Blau, W. J., Boland, J. J., and Coleman, J. N. (2009) The spatial uniformity and electromechanical stability of transparent, conductive films of single walled nanotubes. *Carbon* 47, 2466 – 2473.

[157] 2013; http://www.iljin.co.kr/eng/BusinessArea/material.asp.

[158] 2013; http://physicsworld.com/cws/article/news/2010/feb/26/both-answers-correct-in-century-old-optics-dilemma.

[159] Valdes, L. B. (1954) Resistivity Measurements on Germanium for Transistors. *Proceedings of the IRE* 42, 420–427.

[160] Cao, G. In *Nanostructures and nanomaterials:Synthesis, properties and applications*; Press, I. C., Ed.; Imperial College Press, 2004.

[161] Song, Y. M., and Lee, Y. T. (2010) Antireflective nanostructures for high-efficiency optical devices. *SPIE n/a*, 1–2.

[162] Wiley, B. J., Wang, Z., Wei, J., Yin, Y., Cobden, D. H., and Xia, Y. (2006) Synthesis and Electrical Characterization of Silver Nanobeams. *Nano Letters* 6, 2273–2278.

[163] Bid, A., Bora, A., and Raychaudhuri, A. K. (2006) Temperature dependence of the resistance of metallic nanowires of diameter below 15nm: Applicability of Bloch-Gruneisen theorem. *Phys. Rev. B* 74, 035426.

[164] 2013; http://www.tekra.com/content/products.

[165] Kummali, M. M., Schwartz, G. A., Alegria, A., Arinero, R., and Colmenero, J. (2011) Compatibility studies of polystyrene and poly(vinyl acetate) blends using

electrostatic force microscopy. *Journal of Polymer Science Part B: Polymer Physics 49*, 1332–1338.

[166] 2013; http://www.ke-chuang.com/productshow.asp?id=89.

[167] 2013; http://www.goodfellow.com/E/Polyethylene-terephthalate.html.

[168] Nirmalraj, P. N., Bellew, A. T., Bell, A. P., Fairfield, J. A., McCarthy, E. K., OKelly, C., Pereira, L. F. C., Sorel, S., Morosan, D., Coleman, J. N., Ferreira, M. S., and Boland, J. J. (2012) Manipulating Connectivity and Electrical Conductivity in Metallic Nanowire Networks. *Nano Letters 12*, 5966–5971.